DIPARTIMENTO DI SCIENZE ECOLOGICHE E BIOLOGICHE (DEB)

XXXI CICLO DI DOTTORATO DI RICERCA IN ECOLOGIA E GESTIONE SOSTENIBILE DELLE RISORSE AMBIENTALI

Green Chemistry and Bionanotechnology: Design of Poly(phenols) in Biocatalysis, Functionalized Nanomaterials and Bio-based Product

A thesis presented

by

Davide Piccinino

to

The Department of Biology and Ecology Science

in partial fulfillment of the requirements

for the degree of

Doctor of Philosophy

in the subject of

Organic chemistry of natural compounds (CHIM/06)

Tuscia University
Viterbo, Italy
January 2019

Thesis advisor
Raffaele Saladino

Thesis advisor
Raffaele Saladino

Author
Davide Piccinino

Green Chemistry and Bio-nanotechnology: Design of Poly(phenols) in Biocatalysis, Functionalized Nanomaterials and Bio-based Product

Abstract

Each project that was carried out during the doctoral period is in the field of green chemistry and circular economy. The projects were divided into two strands: nanotechnology and bio-nanomimetic systems.

In the projects included in nanotechnologies, polyphenols have been designed and applied in various fields. In a first project the polyphenols were successfully used as an eco-sustainable protection coating with galvanic gold coatings.

Microcapsules and nanocapsules based on the contemporary presence of sulfonate lignin and tannic acid have been prepared by the layer-by-layer procedure, using $MnCO_3$ or organosolv lignin as core templates, and polydiallyldimethylammonium chloride or chitosan as positive charged supporting layers. Nanocapsules and microcapsules of mixed polyphenols showed antioxidant activity, UV-shielding properties, and electrochemical responsiveness, higher than that in homo-polymer nanocapsules counterparts and of the native polyphenols, suggesting the presence of synergistic effects between the two components. The presence of UV-visible bathochromic shift suggested the formation of J-aggregates characterized by an orientation of the adjacent phenolic rings parallel to the longitudinal direction of the layer, with a head-to-tail like arrangement. Moreover, nanocapsules of mixed polyphenols showed an aggregation state higher than that observed in references, the specific morphology of their surface being dependent on the structural arrangement of the different components.

Sustainable catalysts for the oxidation of phenol derivatives under environmentally friendly conditions were prepared by the functionalization of lignin nanoparticles with tyrosinase. Lignin, the most abundant polyphenol in nature, is the main byproduct in the pulp and paper manufacturing industry and biorefinery. Tyrosinase has been immobilized

by direct adsorption, encapsulation, and layer-by-layer deposition, with or without glutaraldehyde reticulation. Lignin nanoparticles were found to be stable to the tyrosinase activity. After the enzyme immobilization, they showed a moderate to high catalytic effect in the synthesis of catechol derivatives, with the efficacy of the catalyst being dependent on the specific immobilization procedures.

Laccase from *Trametes versicolor* has been immobilized on lignin nanoparticles following different approaches: i) encapsulation; ii) direct physical absorption; iii) layer by layer coating; and iv) layer by layer coating followed by chemical cross-linking. Different activity and kinetic properties emerged depending on the immobilization procedure, laccase showing a direct electron transfer mechanism toward lignin when adsorbed or coated on the surface of the nanoparticles. The novel catalysts were active in the oxidation of alcohol derivatives to corresponding aldehydes.

The preparation of novel wrapped carbon nanotubes poly(4-vinylpyridine)/methyl trioxorhenium (MTO) based heterogeneous catalysts has been reported by two different procedures: a) the wrapping by grinding of multiwalled carbon nanotubes (CNTs) with pre-formed adducts (PVP/MTO and PVPN/MTO) and, b) the loading of MTO on previously wrapped CNTs with PVP and PVPN resins. The novel catalysts were characterized by SEM, TEM, ICP-MS and XPS analyses. Both types of catalysts were efficient systems in the oxidation of recalcitrant aromatic sulfur derivatives with H_2O_2, as representative models of ODS processes. The performance of novel catalysts was found to be dependent on the specific procedure applied for the immobilization of the active species.

DOPA peptidomimetics are an attractive therapeutic tool for the treatment of Parkinson’s disease. Compounds with unusual O-C and N-C covalent bonds between amino acids have been prepared by selective oxidative functionalization of tyrosine residues with tyrosinase from Agaricus bisporus. The reaction proceeded through Michael-like nucleophilic addition of amino acids on the DOPA quinone intermediate initially produced by tyrosinase oxidation. The reaction was effective under heterogeneous conditions by immobilization of tyrosinase on multi walled carbon nanotubes (MWCNTs). The anti-Parkinson activity of novel DOPA peptidomimetics was evaluated by electrophysiological techniques on individual dopaminergic neurons in rat ex vivo midbrain slices. Gly-N-C-Dopa and Val-N-C-Dopa peptidomimetics inhibited neuronal firing and evoked outward currents via activation of the D2 receptors in most

dopamine-sensitive neurons. In a subset of neurons which displayed low dopamine sensitivity, Gly-N-C-Dopa also caused significative effects.

Contents

2 BIO-NANO TECHNOLOGIES

3 BIONANOMIMETIC SYSTEM

List of figures

List of papers

- Piccinino D., Capecchi E., Botta L., Bizzarri B.M., Bollella P., Antiochia R. and Saladino R., Layer-by-Layer Preparation of Microcapsules and Nanocapsules of Mixed Polyphenols with High Antioxidant and UV-Shielding Properties. *Biomacromolecules,* **2018**, *19*(9) 3883-3893

- Capecchi E., Piccinino D., Delfino I., Bollella P., Antiochia R., Saladino R., Functionalized Tyrosinase-Lignin Nanoparticles as Sustainable Catalysts for the Oxidation of Phenols. *Nanomaterials,* **2018**, *8*(6)

- Botta, L., Bizzarri, B.M., Piccinino, D. et al. Prebiotic synthesis of carboxylic acids, amino acids and nucleic acid bases from formamide under photochemical conditions. *Eur. Phys. J. Plus,* **2017**

- Botta L., Brunori F., Tulimieri A., Piccinino D., Meschini R., and Saladino R., Laccase-Mediated Enhancement of the Antioxidant Activity of Propolis and Poplar Bud Exudates *ACS Omega,* **2017**, *2*(6), 2515–2523

- Bizzarri B.M., Martini A., Serafini F., Aversa D., Piccinino D., Botta L., Berretta N., Guatteo E. and Saladino R. Tyrosinase mediated oxidative functionalization in the synthesis of DOPA-derived peptidomimetics with anti-Parkinson activity *RSC Adv.*, **2017**, *7*, 20502-20509

- Piccinino D., Abdalghani I., Botta G., Crucianelli M., Passacantando M., Di Vacri M.L. and Saladino R. Preparation of wrapped carbon nanotubes poly(4-vinylpyridine)/MTO based heterogeneous catalysts for the oxidative desulfurization (ODS) of model and synthetic diesel fuel. *App. Cat. B Env.*, **2017**, *200,* 392-401

- Piccinino D., Delfino M., Botta G., Crucianelli M., Grossi V., Passacantando M., Antiochia R., Favero G. and Saladino R., Highly efficient synthesis of aldehydes by layer by layer multi-walled carbon nanotubes (MWCNTs) laccase mediator systems. *App. Cat. A: General 499,* **2015**, 77-88.

Acknowledgments

Qualcuno di passaggio, qualcuno fino alla fine, molte sono state le persone con cui ho condiviso questa esperienza durante questo percorso di dottorato. Sicuramente il primo ringraziamento più sentito va al prof. Saladino Raffaele, che non solo mi ha dato la possibilità e la fiducia per progredire nella ricerca, ma che non ha mai mancato di seguirmi con professionalità. Un ringraziamento speciale ai miei colleghi di lavoro, Bruno, Lorenzo e Silvia con cui ho condiviso la mia crescita ed esperienza con rispetto, comprensione ed amicizia. Un ringraziamento speciale lo dedico alla mia compagna, Eliana, che con me ha condiviso parallelamente gioie e dolori dandomi un fondamentale sostegno per il raggiungimento di questo traguardo.

Dedico questo lavoro tuttavia alla mia famiglia, che è sempre stato il vero e unico supporto per andare avanti alimentando con amore la mia forza per non mollare mai.

In ultimo, ma non certo per importanza a tutti i miei amici che hanno sempre creduto in me più di quanto potessi fare io.

Chapter 1
Introduction

1.1 Green chemistry and Circular economy

The growth of a new consciousness and sensitivity towards the environment and waste has led to the emergence of new eco-sustainable philosophies; Green Chemistry and Circular Economy. These philosophies enclose the application of their general principles to the chemical processing industry, opening the way to a steep change of paradigm: chemistry, often associated with dirty and polluting production practices, now provides all the tools for the solution of environmental pollution. Green Chemistry is based on the application of twelve principles set out in 1998 by Anastas and Warner[1]: (a) prevention, (b) atom economy, (c) less hazardous chemical syntheses, (d) design for safer chemicals, (e) safer solvents and auxiliaries, (f) design for energy efficiency, (g) use of renewable feedstocks, (h) reduction of derivatives, (i) catalysis, (j) design for degradation, (k) real-time analysis for pollution prevention, and (l) inherently safer chemistry for accident prevention. Now it provides a guide to pollution, climate change and the exhaustion of non-renewable sources. The core topic is the design, development, and implementation of chemical products and processes that reduce or eliminate the use and generation of substances hazardous to human health and the environment.

On the other hand, the circular economy has become a widespread paradigm for controlling production processes, so that their design should avoid waste production. The new paradigm of a circular economy suggests an innovative way of exploiting resources that is only viable through closed industrial loops. The recovery and recycling of building blocks and semi-finished products makes possible exploring new businesses way by reducing the environmental responsibility due to extraction and refining of virgin materials. This approach can be realized through a new way of thinking, which is based on the waste-to-resource opportunities. As a matter of fact, the core principles of the circular economy involve the recycling and the re-use of materials accompanied by a comprehensive and sustainable use of resources[2]. In this context, the recirculation concept has been introduced by Clark et al.[3] In general, a recirculated product is able to reach the usable state again without waste, making possible the optimization of the use of materials, and reducing waste and pollution. The chemical industry should represent an excellent example of symbiotic production with the earth. According with a well-known quote of August Wilhelm von Hoffman (1848) “in an ideal chemical factory there is, strictly speaking, no waste but only products. The better a real factory makes use of its waste, the

closer it gets to its ideal, the bigger is the profit". Therefore, the introduction of innovative recycling visions and activity provides opportunities to reduce the global chemical industry environmental footprint by contributing to the development of a lower carbon society. It is therefore clear that this point must be underlined when fulfilling the Green Chemistry & Green Engineering principles[1,4] and pursuing a benign by design[5]. Although recycling usually refers to the treatment of end-of-life materials, new scenarios that include by-product recycling and solvent recovery are new goals to be achieved. Nowadays, with the growth of circular economy, waste should become the new raw material for industrial processes[6] (Figure 1.1).

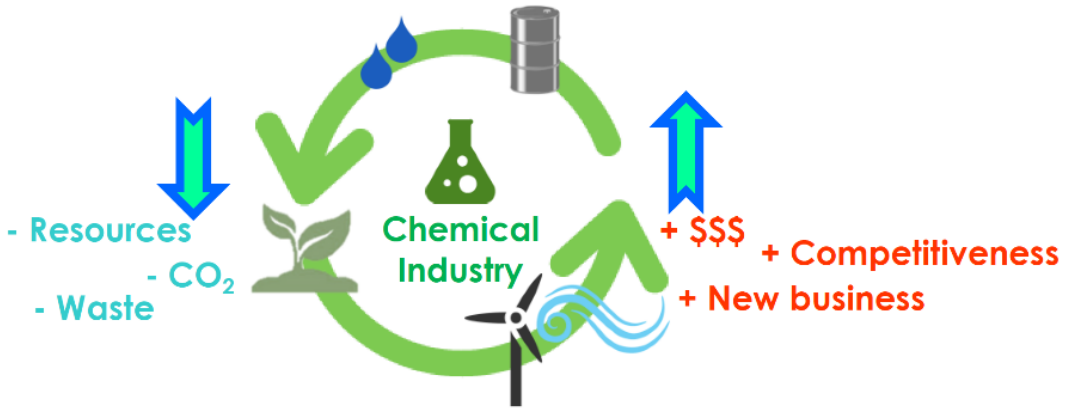

Figure 1.1. Chemical industry in circular economy view

Green chemistry anticipated the concept of circular economy: "1. Prevention: It is better to prevent waste than to treat or clean up waste after it has been created. 2. Atom Economy: Synthetic methods should be designed to maximize the incorporation of all materials used in the process into the final product." In fact, these two principles also belong to the circular economy approach, which aims precisely to achieve a zero-waste objective through a complete exploitation of all waste and by-products, for all production processes. Although starting from a common context, circular economy and green chemistry seem to proceed in some way on parallel routes, rarely crossing. For instance, the production of biofuels from residual biomasses, as we will see in the next chapter, (a paramount circular economy application) often passes through the use of non-renewable, hazardous chemicals to ensure the economic feasibility of the production process.

How to get the change? The fundamental challenge that is proposed in this era is the achievement of a new awareness where the current society is actually still based on consumption and controlled only by the demand and market forces, without having the foresight of its deleterious effects. While we are facing an unprecedented rate of growth

in the demand for resources, we should re-evaluate our relationship with the planet, as the new emerging economies in Asia and Latin America are still moving towards the standards and demands established in the last century in the West. The chemical industry that has been so effective for much of the twentieth century is now under enormous pressure to change in almost all aspects of how it operates[7]. The legislation concerning chemical production processes has grown exponentially in the last years of the twentieth century[8]. The industry is also suffering rising costs for energy and for the disposal of hazardous waste; these costs are increasing at a rate greater than the price of their associated products. Life expectancy and environmental safety of products have also increased in the early years of the twenty-first century. This is mainly due to general environmental concerns and reports, mostly from non-governmental organizations, on the detection of synthetic chemicals in animals and humans (as much a result of improvements in analytical science as of any increase in exposure to chemicals)[9]. Oil alternatives for long-term sustainable chemical production are essential because of the rapid rise in the price we have seen of oil, the main raw material of the organic chemical industry[10]. Therefore, chemical production must overcome a degree of pressure never seen in every phase of the life cycle or chemical production chain, as shown in Figure 1.2.

So, for the first time, the entire industrial supply chain is consciously influenced and interested in the long-term availability of chemicals. Many currently used chemicals will be replaced thanks to new legislation [e.g., REACH (Registration, Evaluation, Authorisation and Restriction of Chemicals) and RoHS (Restriction of Hazardous Substances)][8]. REACH has made it clear that research will inevitably have to discover, develop and apply greener substitutes for many important chemicals. These will also include current solvents, adhesives, flame retardants and stabilizers.

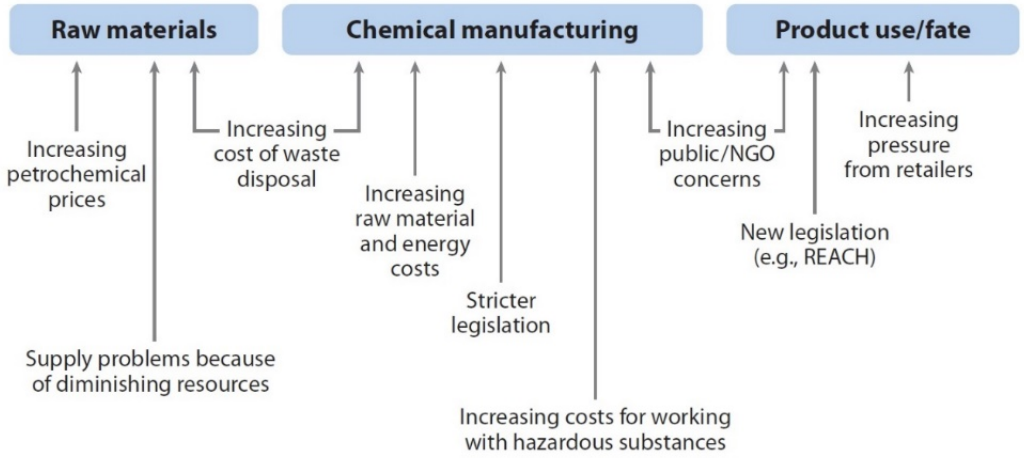

Figure 1.2. Pressures on the chemical industry across the life cycle. Abbreviations: NGO, nongovernmental organization; REACH, Registration, Evaluation, Authorisation and Restriction of Chemicals.

For example, the chlorofluorocarbons were replaced by hydrochlorofluorocarbons, which were then replaced by hydrofluorocarbons, which are now considered incompatible with the new legislation due to their high environmental impact historically started with their action in the formation of the ozone hole. Volatile chlorinated solvents in dry cleaning, polybrominated compounds in flame retardants and aluminium chloride in many organic processes have been considered unacceptable for many years, but we continue to use them in large quantities due to the lack of suitable legal and ecological substitutes. We must therefore concentrate our efforts in this area and, in particular, implement economically favourable substitutions based on chemicals derived from alternative and renewable resources, which nature has always provided us with.

1.2 Polyphenols: sustainable building block for new bio-based materials

The primary role of the chemical industry is the conversion of raw materials into value-added products that include fuels, polymers, materials, pharmaceutical products, etc. Fossil resources have been the primary raw material for most chemical processes and transformations. However, as was mentioned in the previous chapter, sustainability is becoming a global requirement. Due to the considerable depletion of fossil resources, the concept of "biorefinery" become a real solution for sustainable development. In this paradigm, renewable raw materials (intended as biomass or food wastes) are refined/enhanced to produce fuels and basic chemicals through novel chemical and biological technologies.

In recent years, research in the field of biorefinery, driven also by the availability of specific financing schemes, has focused on the production of energy in the form of fuels. The result is a conspicuous increase in scientific literature work on the development of new methods for converting biopolymers from lignocellulosic biomass into hydrocarbon fuels, pyrolytic bio-oils and fuel additives[11]. However, after a first phase of enthusiasm, the role of biofuels in a future energy supply scenario has been the subject of intense criticism, especially for the so-called "food vs. fuel" competition, in addition to a generic unfavourable energy balance. It is important to consider that economically classic fuels and energy carriers are produced with low speculation such as methane ("biogas"), ethanol ("biofuel") or "biodiesel". The researcher attention has been slowly re-directed to the development of routes for the conversion of lignocellulose and waste streams into platforms of specialty chemicals. These highly valued and marketable products are usually required in smaller volumes than fuels. At these levels, secondary/waste products (e.g. agroindustry, food industry, paper production and recycling) can indeed effectively serve as a renewable raw material for the production of chemicals and special materials. Therefore, a new model, that is substantially respectful of the environment, can be carried out, avoiding that the agriculture may be damaged in the primary production of food, avoiding changes in land use, and the loss of biodiversity, that are two among the most sensitive problems related to the production of biofuels[12].

Generally, the production of chemicals starting from waste streams has the potential to increase the added value of the product without altering or redirecting the current production.

There are different strategies to convert the three main biopolymers found in biomass into conventional chemicals. Their goal is to compete with the classic fossil-based production chains. In addition, due to the controversial shale gas revolution, which seems able to provide some of the traditional energy carriers and platform chemicals at a very competitive price, competition should increase, despite the extremely negative environmental effects[13].

However, the new biorefinery approaches focused on a number of elements that are potentially able to change the current building blocks of the chemical industry for the preparation of pharmaceutical materials and products. These natural compounds do not immediately compete with petrochemicals derivatives and could be used for innovative products. Among these polyphenols, such as tannins and lignin, have received the attention of the scientific community because they represent a new pool of natural and widely diffused chemicals, useful for the preparation of new polymers and pharmaceutical products. The real innovation of introducing biobased polyphenols in the economy is their ability to offer new and more effective properties compared to the corresponding products derived from oil, which often go beyond the intrinsic benefits of sustainability and biocompatibility. In this thesis work several projects are described in which polyphenols have been exploited for different eco-sustainable applications.

1.2.1 Woody biomass as new biorefinery

There are many differences between the biorefinery and the classical refinery plant, which converts fossil raw oil into higher value products through processes that have been optimized over time and which are able to enhance each fraction of the starting stock. An important difference, for example, is that oil occurs naturally in the form of a liquid and is characterized by an almost zero oxygen content, while biomass is often solid and composed of a high quantity of oxygenated molecules. In general, raw materials, including organic waste from crops, wood and straw are very heterogeneous as they are mainly composed of polysaccharides (which generally represent 60-80% of the weight) and the rich aromatic lignin (15-30% by weight). These molecules are closely related to form of a stable nanocomposite (Figure 1.3).

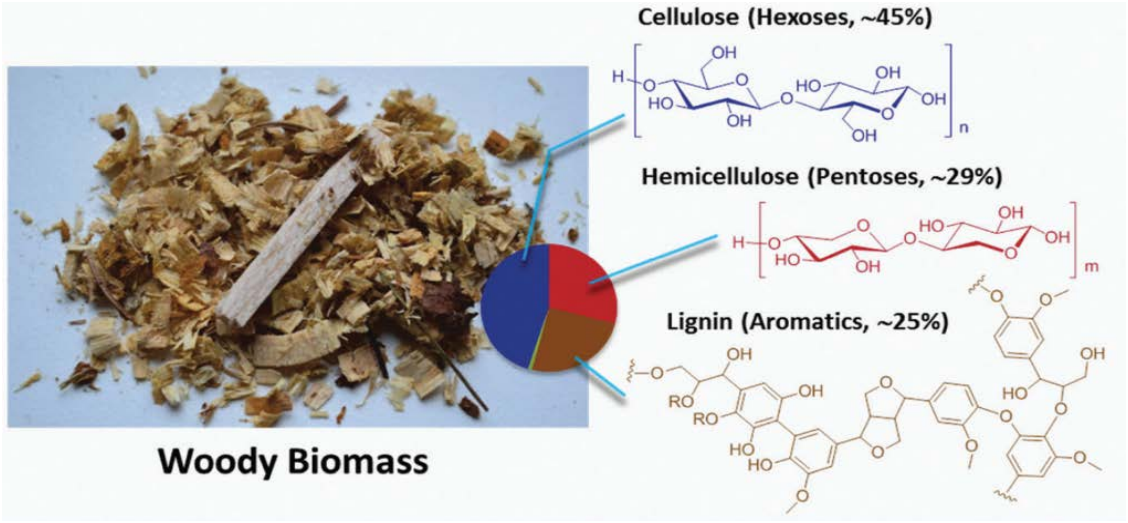

Figure 1.3. Woody mass composition

The first biorefinery approach towards woody biomass was to transform the solid state into processable liquid wood, that is the production of so-called biocrude oils (e.g., pyrolysis oils, hydrothermally derived oils), which have already found an economic position on the market by several companies. However, these bio-oils are not yet competitive if the final goal is the valorization process, such as building blocks and functional molecules. Since the biomass is very heterogeneous, the selective production of some fine and platform chemicals has proved technically far more difficult and problematic as any process aimed at the deconstruction of the biomass in its monomers acts in a non-selective way. The excessive cost of such separation procedures has been one of the major drawbacks of such approaches. So, it was crucial to develop new, more selective methods in the deconstruction phases of the lignocellulosic mass able to separate its components. An effective solution to solve this limit could be that of separating from the biomass the carbohydrate component from the lignin portion, thus obtaining two separate streams of products that will follow different dies. Among the simplest, most effective and environmentally friendly methods, surely the solvothermic one is the most considerable, which provides the treatment of biomass with organic solvents at high temperatures. The first optimization of this approach began originally for the isolation of the cellulose fraction from lignin, inspired by the knowledge of the pulping processes developed by the paper industry. In the present days, however, new methods have been designed that can simultaneously deconstruct polysaccharides and partially depolymerize the lignin. In this field, the degradative deconstruction processes (DD) are distinguished from non-degrading ones (NDD). NDD processes are basically based on dissolution

operations through specific organic solvents ("organosolv") or water and with the use of mild additives (catalysts, reagents, etc.). The process is based on the difference in solubility in the selected solvents and conditions, where cellulose, hemicellulose and lignin can be separated in the form of partially depolymerized substances. On the other hand, the DD processes involve the application of catalysts or reagents capable of promoting hydrolysis and cutting reactions to a more aggressive extent. Depending on the catalytic conditions chosen, DD processes can be adapted to different needs to generate a variety of different products ranging from partially and completely depolymerized carbohydrate blends and well-defined lignin and platform chemicals (Figure 1.4).

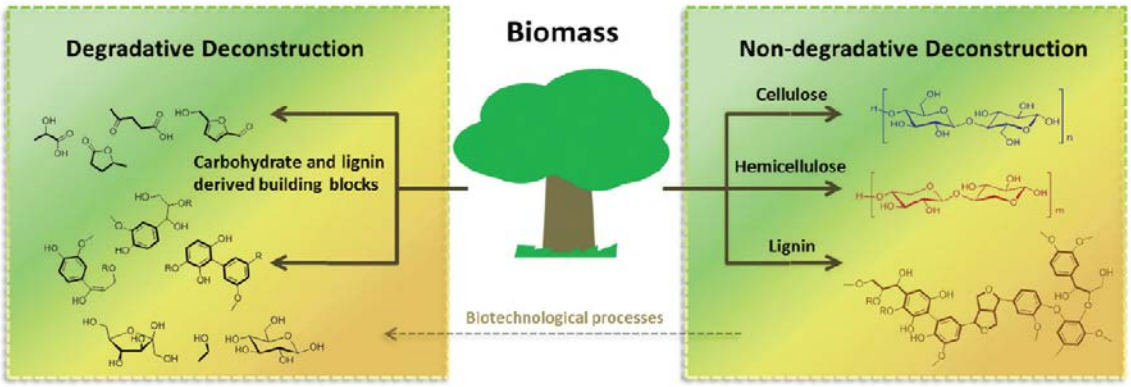

Figure1.4. A representation of degradative (DD) and non-degradative (NDD) deconstruction processes, for the valorization of biomass.

Here the attention will be focused on lignin, which can be obtained through both DD and NDD processes starting from wood.

1.3 Lignin valorization technologies

Nowadays, the integrated biorefinery generally includes four main sections: collection and storage of raw materials, pre-treatment, enzymatic hydrolysis and fermentation of sugar [14]. Lignin, the most abundant polyphenol in nature and the second most abundant biopolymer on Earth after cellulose, is underutilized in the first-generation biorefinery process, with about 60% more lignin being produced with respect to that used for the energy production[15]. So, new processes that generate value-added products from lignin

are required[16]. Lignin is composed of aromatic sub-units[17]. The U.S. Energy Security and Independence Act of 2007 mandates the development of 79 billion liters of second-generation biofuels annually by 2022. Assuming a yield of 355 liters per dry ton of biomass, 223 million tons of biomass will be used annually, producing about 62 million tons of lignin[18]. Without new applications, the lignin produced would far exceed the current world market [19]. Although research has historically focused on lignin conversion procedures in chemicals, materials and fuels, at the practical level very little of this effort has come to the final market. What has changed to address this paradigm? The lignin market comes from: i) bioengineering of lignin to modify and/or incorporate atypical components that reduce recalcitrance of the cell walls to bioprocessing and facilitate ease of recovery and conversion; (ii) advances in analytical chemistry and computational modelling that couple developments in genetic engineering of lignin to targeted physical and chemical properties; and (iii) biomass pre-treatment technologies that facilitate lignin recovery and catalytic modifications that yield tailored chemical and/or physical properties.

1.3.1 Lignin biosynthesis and recovery from biomass

Lignin is deposited predominantly in the walls of secondarily thickened cells together with cellulose, hemicellulose and pectin, especially in vascular and support tissues: xylem tracheitis, vessel elements and sclereid cells[20]. This polymer is covalently linked to the hemicellulose by crossing different plant polysaccharides, giving mechanical strength to the cell wall as well as other properties as rigidity, UV protection and important role in conducting water in plant stems[21]. Its biosynthesis can also be induced upon various biotic and abiotic stress conditions, including wounding, pathogen infection, metabolic stress, and perturbations in cell wall structure[22].

Lignin biosynthesis

Lignin is a polyphenol resulting from the oxidative coupling of 4-hydroxyphenylpropanoid units[23]. The main building blocks of lignin are the hydroxycinnamyl alcohols (or monolignols), namely coniferyl alcohol and sinapyl

alcohol, and minor amount of p-coumaryl alcohol (Figure 1.5). The pathway of the biosynthesis of the monolignols is reported [24], and it is still under study[25]. The monolignols are synthesized from phenylalanine (Phe) via the phenylpropanoid and monolignol-specific pathways. Phe comes from the shikimate pathway in plastids[26]. Enzymes that participate in lignin biosynthesis, such as cinnamate 4-hydrolase (C4H), p-coumarate 3-hydroxylase (C3H) and ferulate 5-hydroxylase (F5H), are present in the in the cytosolic side of the membrane of the endoplasmic reticulum[27]. Although in the metabolic pathway the interconnection between phenylalanine ammonia-lyase (PAL) and C4H[28] has been demonstrated, it remains unknown if the other enzymes of the pathway are included in other metabolic complexes of the endoplasmic reticulum. Units from the monolignol metabolism in the final lignin polymer structure are called guaiacyl (G), siringyl (S) and p-hydroxyphenyl (H) units. (Figure 1.5).

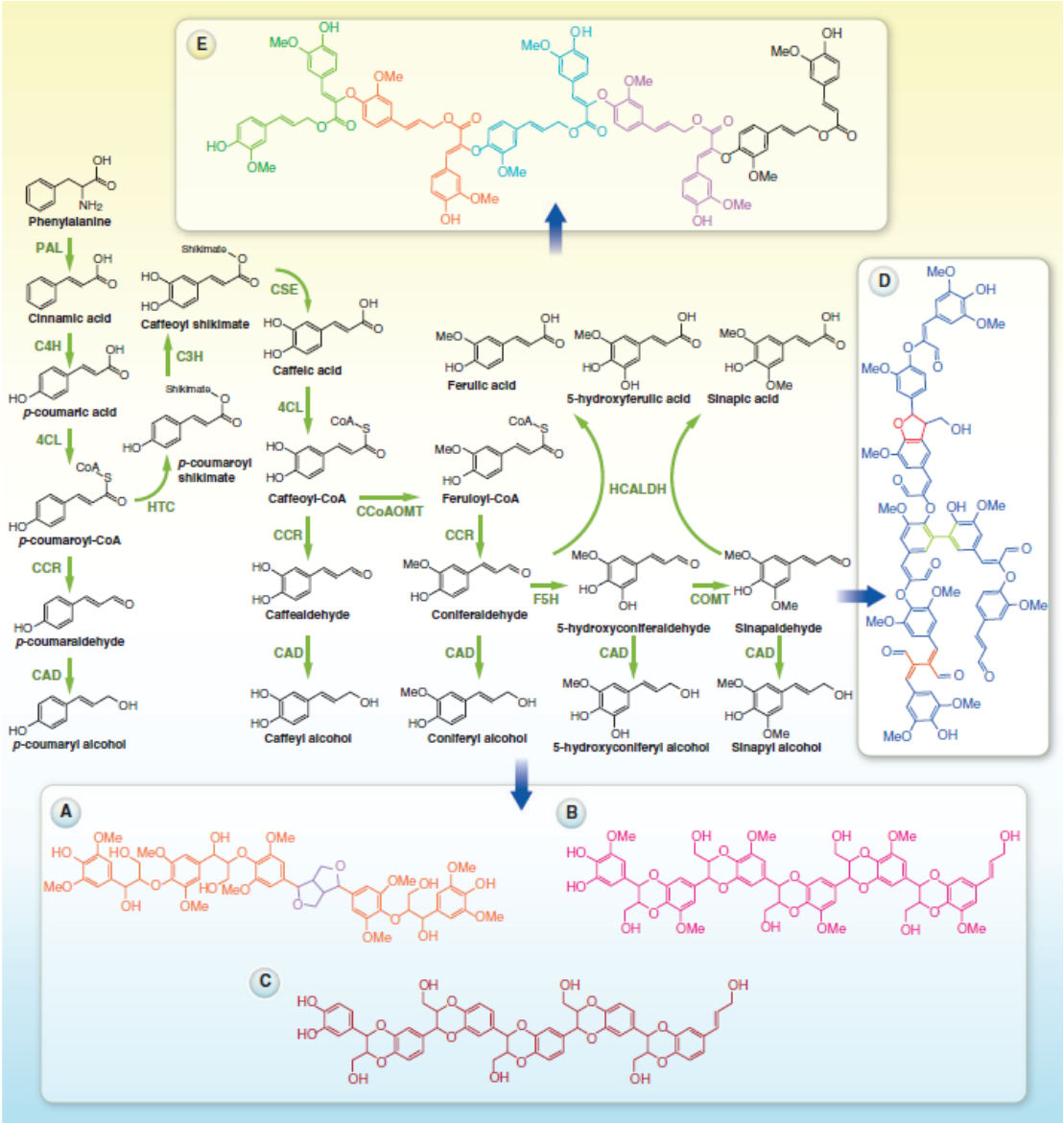

Figure 1.5. Biosinthesys pathway of lignin

Except for a few number of cases[29], lignin recovered from Gymnosperms is usually composed of G-units (with minor quantities of H-units), while the lignin presents in the angiosperm dicotyledonous consists mostly of both G- and S-units. H-units are found in high amount in softwood and in grass[23]. A variety of less abundant units have been identified from diverse species, and these units may be incorporated into the polymer at varying levels[30]. Some units, such as those derived from sinapyl acetate, can make up to 85% of all S-units in the polymer[31]. The lignin composition may also vary depending on the cell type, as can be visualized by the histochemical staining of Mäule, which is indicative of S-units[32].

Different biotechnological methodologies have led to the possibility of modulating the quantity and type of lignin produced by a specific plant, including copper transporters, vesicular trafficking genes, shikimate pathway genes, and transcription factors. However, most attempts to increase lignin levels in plants simply by overexpressing one or more enzymes in the monolignol pathway have not been successful. Examples are the down-regulation of cinnamyl alcohol dehydrogenase which leads to an increase of aldehydes in lignin[33] mutants, and the deprivation of cinnamyl alcohol dehydrogenase 1 gene (CAD1), which produce lignin exclusively composed of hydroxy- cinnamaldehydes rather than hydroxycinnamyl alcohol units[34]. Furthermore, it was also possible to introduce unnatural monomers in the polymer which are able to lead to the formation of several cleavable interunit bonds[35], reducing the degree of polymerization and facilitating the processing of biomass. An alternative approach was recently reported by Wilkerson et al.[36] whereby coniferyl ferulate feruloyl–coenzyme A (CoA) monolignol transferase was expressed in poplar. This transformation facilitated the incorporation of monolignol ferulate conjugates into lignin, which yields a polymer with an elevated number of ester linkages reactive towards mild alkaline depolymerization conditions. This flexibility in lignin monomer composition is potentially useful for reducing recalcitrance, enhancing extraction, and developing lignin as a high-value raw material.

Lignin Recovery

Lignin is one of the main products recovered from the NDD biomass processes. This polymer was historically produced mainly by the paper industry as a waste product after the separation step from cellulose. Nowadays, lignin-rich streams are produced from biorefineries by extracting plant carbohydrates to leave most of the lignin in the final solid

residue[37] or by applying pre-treatments to the biomass by extracting the lignin[38] before the conversion of carbohydrates (Figure 1.6).

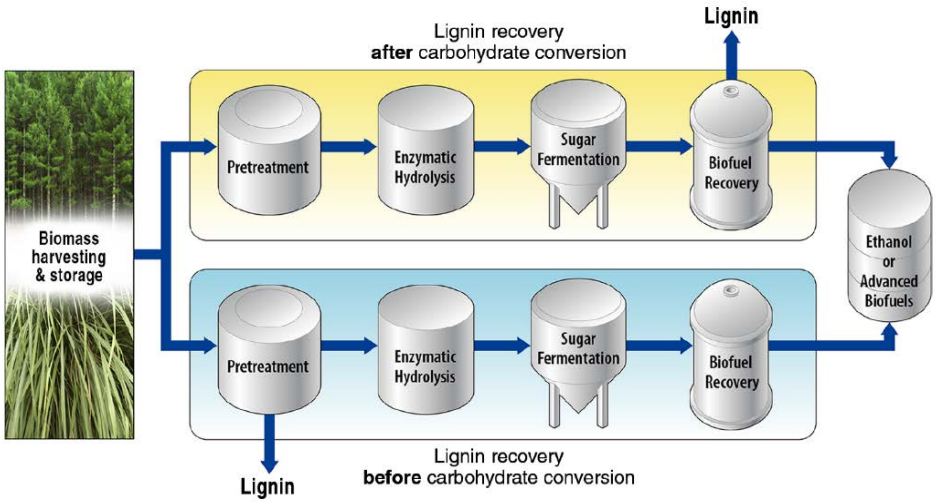

Figure 1.6. The two ways of lignin biorefinery

Lignin isolated after enzymatic deconstruction currently contains some recalcitrant polysaccharides, proteins, and mineral salts, a mixture that is generally considered to have a low suitability for direct material applications.

Hardwood, softwood and grass lignin incorporate the same pool of monomers, although the relative content of building blocks is quite different. However, the extraction type (NDD) is a factor that greatly influences the composition and variety of lignin. The most common types of industrial purification of lignin from biomass are summarized in Table 1.

For the most part, the various treatments provide lignin fragments with different degrees of polymerization and may alter the distribution of the various functional groups. Even the presence of additives used during the pulping process often leads to the introduction of new functionalities that were not originally present in the polymer. For example, in the case of Kraft lignin or lignosulphonate, a significant amount of sulfur is introduced in the polymer as thiol groups. Low molecular weight lignin polymers or even oligomers are usually obtained from all the pulping processes. Recently, alternative purification methods for lignin based on the use of IL have been proposed[39].

Lignin preparation *via* NDD ↓ Pulping Processes	
	Kraft Pulping. Based on the use of sodium hydroxide and hydrogen sulfide. This process results in the incorporation of sulfur in the form of aliphatic thiols into the resulting low molecular weight lignin fragments. Possible carbon-carbon bond formation via recombination of smaller fragments leads to a relatively inert structure.
	Sulfite Pulping. Based on the use of acids and sulfites (usually Ca/$MgSO_3$) at around 150°C. Also in this case, sulfur is incorporated into the final oligomers via introduction of sulphonic acid functionalities on the backbone. This confers to the product a relatively good water solubility.
	Alkali Treatment. The method relies on the use of hydroxides of alkaline and hearth alkaline metals under relatively high pressure and temperature, favoring to a good extent the cleavage of α and β ether linkages. In this way, oligomeric lignin in the range of 1-5 kDa are produced.
	Organosolv Treatment. This extractive technique is based on the use of organic solvents usually in combination with water. Acid or based catalysts can also be added leading to relatively short lignin fragments (ca. 5kDa).
	Ionosolv Treatment. This method is a special variant of organosolv in which ionic liquids are used as extracting media for lignin at moderate to elevated temperature. The method is based on the fact that ionic liquid have the ability to dissolve cellulose as well as lignin. Cellulose can be thus separated by addition of an anti solvent.

Lignin type	Sulfur-lignins		Sulfur-free lignins	
	Kraft	Lignosulfonate	Soda	Organosolv
Aspect				
Raw materials	Softwood Hardwood	Softwood Hardwood	Annual plants	Softwood Hardwood Annual plants
Solubility	Alkali Organic solvents	Water	Alkali	Wide range of organic solvents
Number-average molar mass (M_n – g mol^{-1})	1000–3000	15,000–50,000	800–3000	500–5000
Polydispersity	2.5–3.5	6–8	2.5–3.5	1.5–2.5
T_g (°C)	140–150	130	140	90–110

Table 1. Several kind of lignin extractions and their chemical and physical characteristic

The main disadvantage of this approach concerns the relatively high price and the non-sustainability of current commercial ionic liquids. In alternative, environmentally friendly eutectic solvents (NADES) were proposed[40].

Lignin Valorization

The growing search for eco-sustainable and low-cost biorefinery methodologies has allowed lignin to be introduced into the market thanks to its numerous applications. Although the low-volume chemical additives may derive from lignin, the amount of lignin coming from an industrial cellulosic ethanol plant can range from ~ 100,000 to 200,000 tons per year^{-1} [41]. This polymer can be applied for the replacement of more than 40-50% of the structural steel mass in light vehicles containing carbon fiber composite materials (Assessment of Fuel Economy Technologies for Light-Duty Vehicles)[42]. Unfortunately,

the commercial precursors of carbon fibers, derived from polyacrylonitrile (PAN), are still too expensive for low-cost production on a commercial scale (~ 300 × 106 kg year-1).

Another high-volume lignin application is related to bioplastics and composite materials. The design and production of techno-polymers and thermoplastic elastomers, polymer foams and lignin membranes with properties comparable to those of petroleum products has been reported for some time[43]. The most frequent lignin source for these studies become from chemical pulping operations that are directed primarily at lignin removal from cellulosic fibers through a series of alkaline depolymerization or lignin sulfonation reactions and extraction.

The most frequent source of lignin used for industrial application is alkaline or sulphonate lignin. They have nevertheless found a space in the market mostly as cement filler, dust suppression, and drilling fluids for oil recovery[44]. Other examples encompass the use as additive for lead acid batteries[45] and other select applications [46]. It has also been shown that oxiropropiation of lignin produces a promising polyol derivative in the production of polyurethane foam, exhibiting excellent physical strength properties[47]. The application of lignin for thermoplastic materials is also under development; for example, by mixing from 5.0% to 20% of hydroxyl propyl lignin with poly (methyl methacrylate) an increase of 200-MPa of the Young's modulus is obtained with respect to the pure polymer [48].

Furthermore, it has been demonstrated that lignin, in the presence of cationic conducting polymer necessary to provide electronic conductivity, can function as electron preservation material, with a total performance superior to that of non-sustainable traditional materials.

Phenols are the primary component of phenolic resins, such as resorcinol-formaldehyde (RF)-resin. Such compounds are nowadays used for the production of advanced mesoporous absorption materials[49], electrodes and materials for energy conservation[50]. Moreover, bis-phenol derivatives are an essential part of polycarbonates and epoxy resins, although their use has been the subject of controversial debate due to toxicity issues such as in the case of bisphenol A (BPA), known for its severe effect on the human endocrine system[51]. In this regard, the attention has shifted to lignin derivatives. Vanillin, a constitutive element of the lignin, has been proposed as a synthon for the design of different monomers that could replace the non-sustainable phenol derivatives in resins[52]. Even more interesting are the analogues of resorcinol, which

include natural metabolites such as dopamine or dihydroxy-L-phenylalanine, which have proved to be constituents of advanced biomimetic glues[53], able to bind leather (as known by the traditional art of " tanned skin "with tannic acid derivatives), cellulose fibers, paper and cotton (known to bind lignin in wood), or even minerals, also in the presence of water, as in the case of natural mussel adhesives[54]. Depolymerized lignin phenols appear to be a promising choice for the production of large-scale dopamine or dihydroxy-L-phenylalanine derivatives. In addition to lignin depolymerization, biorefinery processes include a robust strategy for the demethylation of phenols, considering the high percentage of phenyl methyl ethers in the native lignin structure (Fig. 9). Demethylation increases the number of phenolic groups that allows the application of such compounds in redox processes. The most effective demethylation process is based on catalytic hydrodeoxygenation[55]. Alternatively, constituent elements must be selected that do not require demethylation processes such as gallic acid, derived from tannin[56]. Some lignin fractions coming out from the biorefinery are not suitable for the design of materials, but they can still be valuable for conversion into fuels and chemicals.

New techniques involving the use of transition metal catalysts have been used for the hydrogenolysis of lignin, both as one- or two-steps process[57]. These approaches have received considerable academic and industrial attention for the production of petrol-based aromatic units, as well as benzene, toluene and xylenes[57-58]. These techniques include high temperatures and pressures (> 200 ° C and> 5 MPa) in combination with metal catalysts, such as Ni-Mo or Co-Mo/Al_2O_3, with the main function of removing heteroatoms from sulfur and nitrogen. Unfortunately, the catalysts are easily deactivated during the process due to the high formation of coke, the hydrothermal instability and the sintering effect[59]. Oxidative enzymes are also applied for the production of low molecular weight aromatic compounds from lignin [60], including laccase and peroxidase[61].

In the next chapter, the procedures and properties of lignin nanostructures will be described in detail because the generation of nanostructured lignin introduced several industrial advantages.

1.4 Nanostructures towards eco-sustainability

Nanostructures are the basis of nanosciences and nanotechnologies. These technologies represent a broad and interdisciplinary area of research and development that has grown exponentially throughout the world in recent years. It has the potential to revolutionize the ways in which the material and products are created and the range and nature of the features that can be accessed. Nanoscale materials are defined as a set of substances in which at least one dimension is less than about 100 nanometers. A nanometer is one millionth of a millimeter, about 100,000 times smaller than the diameter of a human hair. The real interest of nanostructures are the new properties that emerge in the transition from the macro to nanoscale.

Nanostructures can be classified according to their shape, planar (nano sheet), tubular (nano-fibers or nanotube), or spheres (nano particles and nanosphere). Nanostructured materials (particularly in the 1-100 nm range) offer unique properties due to their increasing surface area[62], and their chemical and physical interactions are governed by surface properties. Thus, a nanostructured material may have considerably different properties from a material of greater size and similar composition[63]. Therefore, the possible applications are provided as an alternative to toxic nanoparticles[64], supports for heterogeneous enzymatic or organometallic catalysts, for drug delivery systems[65], for the release of hydrophobic molecules[66] and to improve the UV barrier, antibacterial, antioxidant properties and polymer reinforcement.

1.4.1 Carbon nanotubes

Both the diamond and the graphite are composed entirely of pure carbon. The substantial difference lies in the atomic organization of carbon atoms. In fact, in the diamond, the atoms have the four ties oriented towards the angles of a normal tetrahedron. The resulting three-dimensional structure is extremely rigid, giving the diamond the known hardness. In graphite, each atom is uniformly connected to three carbon atoms with angles of 120° in the plane and a weak link is present in the axis forming the hexagonal lattice (honeycomb) [67]. In 1985 a new form of carbon was discovered, the fullerene[68]. Later in 1991 multiple-walled carbon nanotubes (MWCNT) were discovered in the carbon soot produced by an arc discharge method[69]. CNTs are tubular in shape, and are made of graphite. The tubes contained at least two layers, often many more, and had

an outer diameter of about 3 nm to 30 nm. Single-walled carbon nanotubes (SWCNTs) were also observed[70]. Single-walled carbon nanotubes are generally thinner than multiple-wall types, with diameters in the 1-2 nm range. They are curved rather than straight.

In recent years, the effort has focused on determining the structural, electrical, mechanical, electromechanical and chemical properties of CNTs as well as on the optimization of their synthesis. The structure of SWCNT can be imagined as a support for a graphene sheet consisting of several hexagonal rings of the benzene type (Figure 1.7). A MWCNT instead is a pile of graphene sheets rolled up in concentric cylinders. Each nanotube is a single macromolecule composed of millions of atoms whose length can reach tens of micrometers with diameters up to 0.7 nm[71]. CNTs are distinguished from carbon fibers, which are not single molecules but layers of stratified graphite layers[72].

In addition to these two classes of nanotubes, we can classify three different sub-types based on how the graphite is "rolled" during the carbon nanotube synthetic process: CNT armchair, CNT zigzag and CNT chiral.

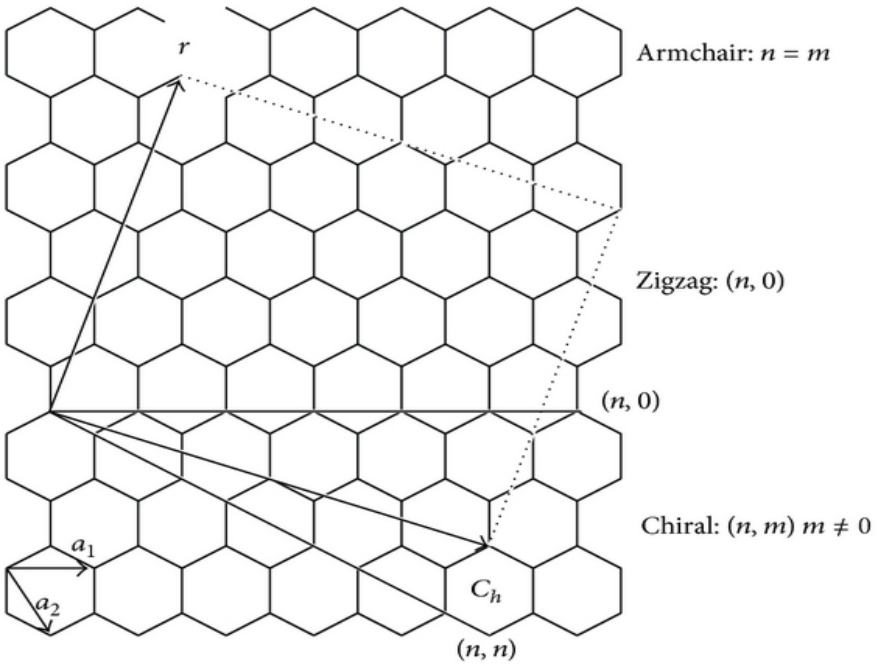

Figure 1.7. Schematic representation of formation of single-walled carbon nanotubes by rolling of a graphene sheet along lattice vectors which leads to armchair, zigzag, and chiral tubes

Properties of carbon nanotubes

The extraordinary mechanical properties of these nanostructures are due to the strength of the carbon-carbon bonds. The excellent mechanical, thermal and electronic properties combined have never been attributed to any material. Their density can reach up to 1.3 g/cm^3 (one-sixth of stainless steel). Young measured modules (material stiffness measurement) are superior to carbon fibers with values higher than 1TPa which is about 5 times higher than steel[73]. Carbon nanotubes are the most resistant materials ever discovered where the maximum tensile strength measured or breaking for a carbon nanotube was up to 63 GPa, which is about 50 times higher than steel[73].

In addition, CNTs have good chemical and environmental stability and a high thermal conductivity (~3000 W/m/K, comparable to diamond). These properties give them great potential in industrial applications.

The electronic properties of carbon nanotubes are also unique in their kind. They have high electrical conductivity, comparable to copper, and they can behave as a metal or a semiconductor.

Synthesis

During the characterization and application of carbon nanotubes, the need to obtain these nanostructures with high quality arisen. High quality means the absence of structural and chemical defects on a significant length scale (eg 1-10 micron) along the axes of the pipe. In most materials, however, due to the occurrence of defects in their structure, the actual observed material properties such as strength, electrical conductivity, and so on are limited very significantly. The number of patents and publications on the synthesis of carbon nanotubes has increased rapidly. However, there are currently four main challenges to overcome in the synthesis of nanotubes: (a) Mass production, ie the development of low-cost, large-scale processes for the synthesis of high quality nanotubes, including SWCNTs; (b) Selective production, ie control on the structure and electronic properties of the produced nanotubes; (c) Organization, ie control on the position and orientation of the nanotubes produced on a flat substrate; (d) Mechanism, ie the development of an in-depth understanding of nanotube growth processes. The growth mechanism is still the subject of controversy and more than one mechanism could be operational during the formation of the CNTs.

There are currently three commonly used methods for synthesizing CNT: bow discharge[74], laser ablation[75], and chemical vapor deposition (CVD)[76]. The basic elements

necessary for the synthesis of the nanotubes are the catalyst, a carbon source and sufficient energy. The common feature of these methods is the addition of energy to a carbon source to produce fragments (groups or individual carbon atoms) that can recombine to generate CNT. The energy source can be arc discharge electricity, heat from an oven (~ 900 °C) for CVD or high intensity light from a laser (laser ablation).

Applications

There are many fields of application in which nanotubes are used, including electronics (Supercapcitors and Actuators, Li Ion Batteries, Field Emission Sources), materials science (Scanning Probe Tips, Conductive Plastics), energy management (Gas and Hydrogen Storage), chemical processing, and others.

CNTs show the highest reversible capacity for use in lithium-ion batteries[77]. Moreover, CNTs are excellent materials for supercapacitor electrodes[78] and are currently being marketed for this application.

For structural applications, plastics have progressed tremendously, but not where electrical conductivity is needed, since plastics are very good electrical insulators. This deficiency can be ruled out by loading plastics up with conductive fillers, such as carbon black and larger graphite fibers (the ones used to make golf clubs and tennis rackets). In order to offer the necessary conductivity using conventional fillers, the loading required is typically high, however, leading to heavy parts and, more prominently, plastic parts whose structural properties are highly limited.

Furthermore, CNTs intrinsically possess an enormously high surface area; actually, for SWNTs, every atom is not just on one surface — but on two surfaces, the interior and exterior of the nanotube. The ability to attach basically any chemical species to their sidewalls (functionalization) offers a prospect for unique catalyst supports for enzymes or organometallic compound. Their electrical conductivity may also be used propitiously in the quest for new catalysts and catalytic behavior.

Other potential applications of CNTs include solar collection, nanoporous filters, catalyst supports, and coatings. There are almost certainly several surprising applications for this excellent material that will be revealed in the future, and which may prove to be the most significant and valuable ones of all. A number of researchers have been studying the conductive and/or waterproof paper produced using CNTs. CNTs have also been demonstrated to absorb infrared light and may hold applications in the I/R optics industry.

1.4.3 Lignin nanocapsules: synthesis, properties and applications

Lignin shows a series of interesting chemical and physical properties, such as the photo-absorbing UV capacity and antioxidant radical scavenging activity. The transition from the native state of the polymer to a nanostructured scale increases the intensity of these properties. Several approaches have been made to obtain nanostructured lignin, encompassing different types of nano-scaled structures, which include nanotubes, nanosheets, nanoparticles and empty nanospheres (Figure 1.8).

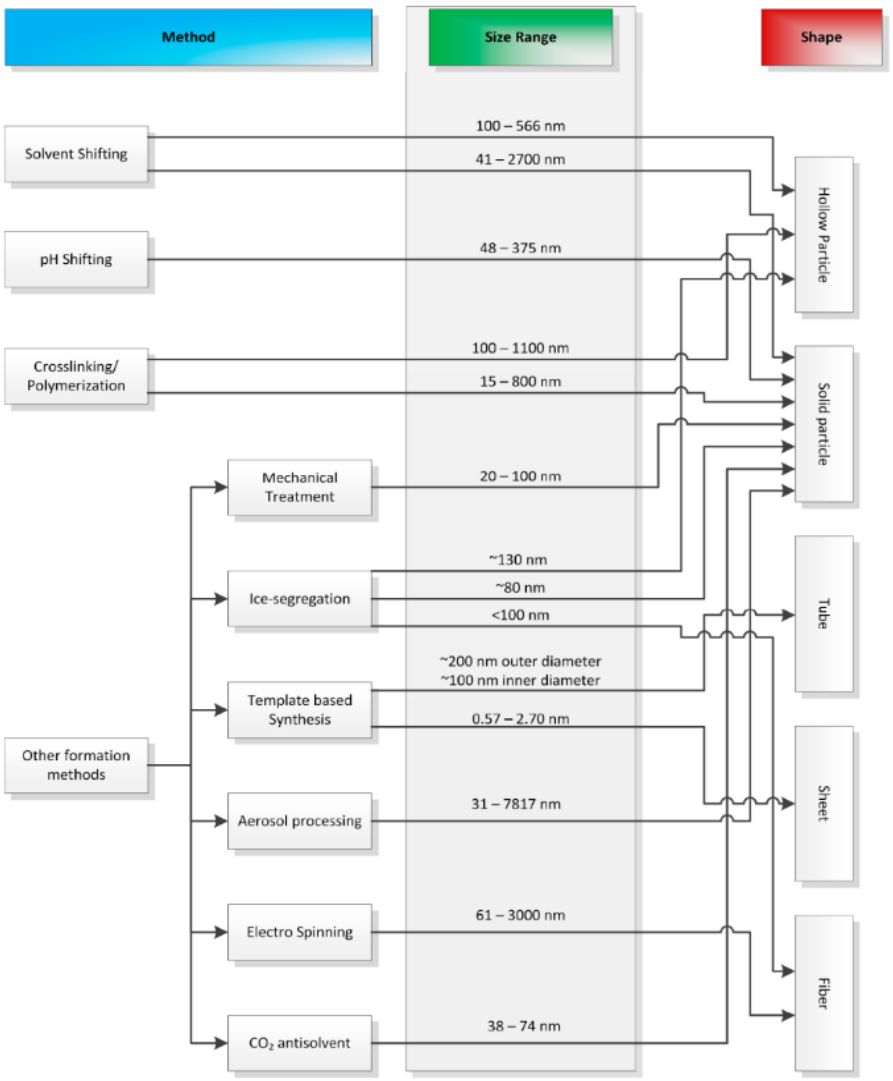

Figure 1.8. Illustration of the methods reported for nano- and micromaterial synthesis. Resulting nano- and micromaterials are classified in five main classes.

The nanospheres have proved to be very advantageous for a number of aspects, including the fact that their spherical shape is characterized by a greater surface to volume

ratio. In the last five years the methods for the preparation of lignin nanospheres increased significantly overcoming various drawback such as the low yield, the use of organic solvents, very long processing time, etc. The first procedure for the preparation of hollow lignin nanospheres was based on the sonication of a water/oil emulsion with or without the presence of cross-linking agents[66]. Subsequently, Lievonen et al.[79] introduced a new procedure based on slow solvent exchange between a Kraft lignin solution in THF and H_2O. The formation of lignin nanoparticles in the THF/water system is driven by the large difference in the solubility of lignin in these solvents. Lignin, which is notoriously non-water-soluble, tends to minimize contact with water, which slowly enters the dialysis tube and replaces THF. During this process the lignin exposes its polar chemical groups to the outside, interacting with the water and hides the apolar group, structuring it in a hollow spherical shape. Further work by Qian et al.[80] reported the preparation of nano- and micro sized spheres by applying the precipitation method from pine wood OS and corn cob EHL, which were in non-acetylated and acetylated form, respectively. The precipitation method required 8:1 vol/vol acetone/water as solvent under the following conditions: (1) Large spheres: a lignin solution with 100 mL acetone/water and 10 g/L was gradually diluted with 400 mL of 0.1 M NaCl aqueous solution while stirring at room temperature; (2) midsized spheres: a lignin solution with 100 mL acetone/water and 10 g/L was gradually diluted with 400 ml of deionized water while stirring at room temperature; (3) small spheres: a lignin solution with 100 mL acetone/water and 0.1 g/L was gradually diluted with 400 mL of deionized water while stirring at room temperature. Furthermore, Yearla and Padmasree[81] used acetone/water solutions (9:1 vol/vol) as solvent for the commercial alkali lignin and hardwood lignin isolated by an acidic dioxane method[82].

Li et al.[83] used KL in a solvent/antisolvent system of dioxane/water. Ultrapure water was added to the lignin/dioxane solution at rates ranging from 0.7 to 14 mL/min with decreasing particle sizes at higher rates. An initial lignin concentration in dioxane of 3.69 g/L with a water dropping rate of 3.3 mL/min yielded spheres with a hollow characteristic and an average hydrodynamic radius of 145.5 nm.

In another study, Li et al.[84] used ethanol as solvent for KL and water as antisolvent. The KL concentration in ethanol was set to 2.28 g/L and ultrapure water was added under stirring at dropping speeds ranging from 0.45 to 36 mL/min until the water content reached 90 wt %. Increasing dropping speeds resulted in smaller capsule diameter (ranging from around 60 to 350 nm). However, this preparation method produced closed capsules that do not open further.

In order to increase the yield of nanocapsules by slow solvent exchange method and decrease the time required for their preparation, optimization studies have been implemented to obtain a scale-up effect[85]. THF can completely dissolve lignin, while water solubility is very low (<5 m%). lignin is still very soluble in mixtures of these solvents when the THF concentration is higher than 50%. So, preparing a 2% lignin solution in a THF/water mixture (6:1), the lignin remains dissolved. After adding the lignin solution to water (double volume of lignin solution) under stirring at room temperature, colloidal nanospheres are obtained instantaneously.

Another important optimization was proposed to replace the organic solvent (THF, Acetone, EtOH), using a no-toxic surfactant to facilitate the dissolution of lignin in water, in accordance with a greater eco-sustainability[86]. The LNPs, having a hydrodynamic diameter ranging from ca. 80 to 230 nm, were formed by self-assembly in a recyclable and non-toxic aqueous solution of sodium p-toluenesulfonate (pTsONa) at room temperature, with a lowest concentration of up to 48 g/L.

It has been observed that the UV absorption and the antioxidant activity of lignin before and after structuring processes are quite different, although the chemical composition of the polymer is unmodified. The only difference is in the newly ordered molecular organization of the polymer at the nanoscale level, as a consequence of the pairing of the aromatic rings. Deng et al.[87] showed that the aromatic groups of Kraft lignin follow a specific type of pairing called J aggregation. In the J aggregation, the π–π paired aromatic units are oriented longitudinally with a head-to-tail arrangement (figure 1.9). According to the theory of the coupling of molecular excitons, the enhancement of the J aggregation would lead to a “red shift” of the UV spectrum (bathochromic shif[88]), therefore increasing the absorbing capacity.

Lignin nanosphere bearing reactive chemical group on the surface (like -COOH and -OH) can be easily functionalized (acetylation, carboxylation ecc.). This chemical property makes the nanospheres suitable for the preparation of improved medical devices (drug delivery system with specific target), and of biodegradable blends for composite polymers (bioplastic, food packaging…)[89].

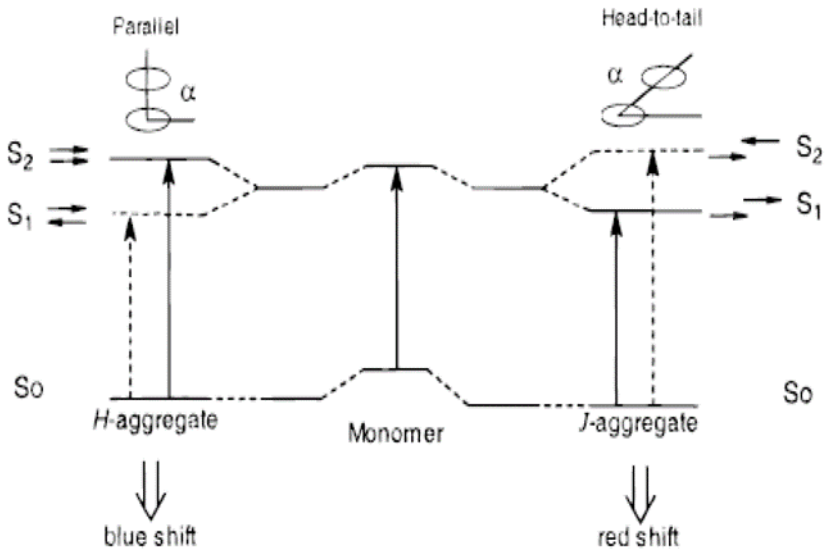

Figure 1.9. Schematic representation of different energy states in different molecular organization

When lignin nanosphere are dispersed in water, the phenolic hydroxyl and carboxyl groups provide a negative surface charge that promotes the formation of electrical double layers, which can stabilize the nanoparticle dispersion via electrical double layer repulsion. The surface shows a typical negative z-potential (-41 mV), stable at wide pH range (2.0 - 12.0) suitable for functional coating using positive charged polyelectrolytes, such as PDDA or chitosan.

A wide range of applications for lignin nanomaterials is reported in the literature (figure 1.10).

Lignin nanosphere can be used as reinforcer filler, improving mechanical properties like stiffness, strength and toughness. Del Saz-Orozco et al.[90] used 8.5 wt % of softwood calcium lignosulfonate particles with an average diameter of 1.6 µm to reinforce phenolic foams, showing greatest mechanical performance and makes it competitive with synthetic fiber-reinforced phenolic foams. In this latter case, the addition of lignin particles determined a compressive modulus and strength of 128% and 174%, respectively, compared to the neat phenolic foam. Another important application of lignin nanosphere is as surfactants in Pickering Emulsions.

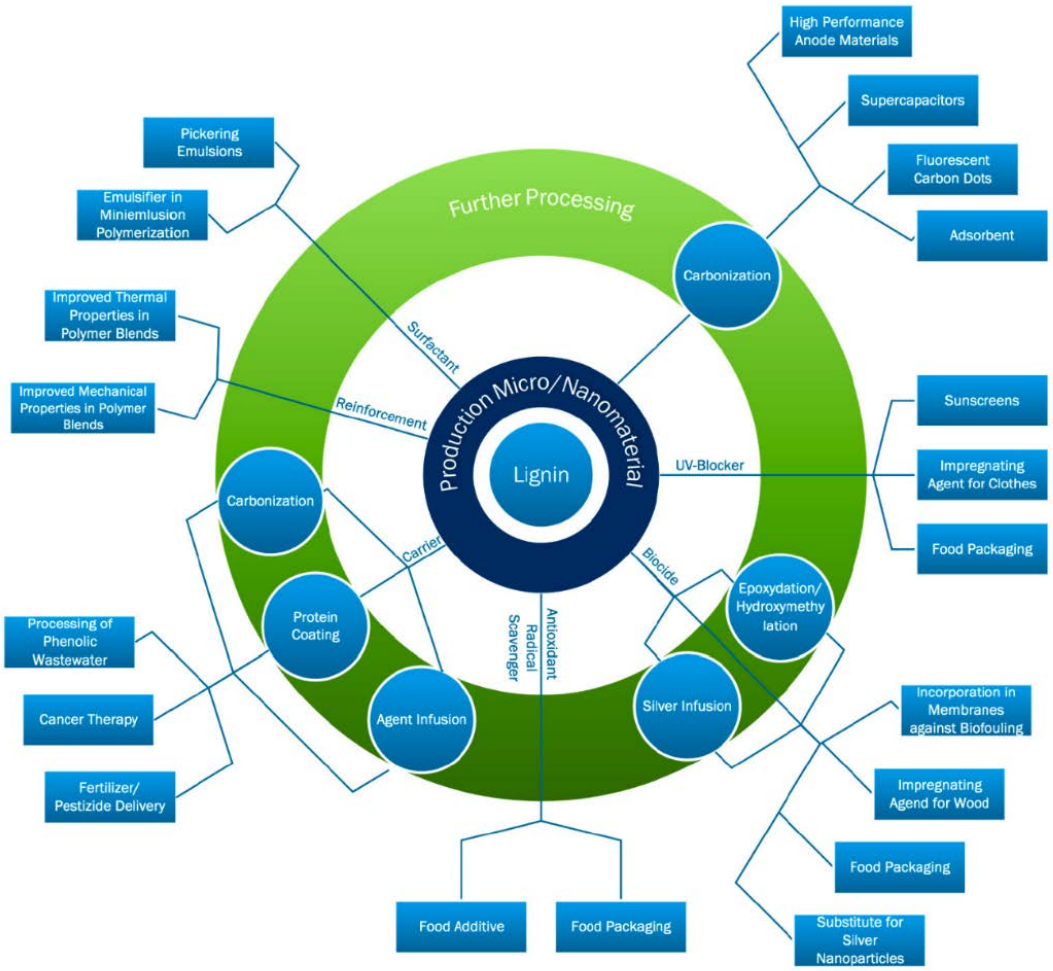

Figure 1.10. Overview of potential applications of lignin in the micro- and nanosized scale.

The large energetic barrier associated with the particle desorption from the interface makes them inherently more stable against coalescence than their surfactant-based counterparts. For example, lignin colloidal nanospheres coated with cationic lignin produced positively charged particles with tailored properties for the stabilization of Pickering emulsions[91].

The use of lignin nanostructures in the medical field as drug shuttle seems to be the most investigated field of application. Microencapsulation has potential applications in the delivery of soluble drugs[92], pesticides[93], gene[94] and food additives[95]. The major problem for controlled release systems is the initial burst which releases a great amount of active agents causing an acutely high concentration and therefore, a failure of the controlled release[96].

Encapsulation might solve this issue. Lignin nano- and microcapsules are reported for the transport of hydrophobic and hydrophilic substances with different releasing

properties [97]. Dai et al.[98] reported the precipitation of LNPs using ethanol, methanol and tetrahydrofuran (THF) as solvent and water or aqueous Fe_3O_4 nano-dispersion as antisolvent.

Here, resveratrol (RSV), a bioactive molecule, was used as active ingredient. In order to incorporate RSV in the LNP, it was mixed with the solvent and incorporated during the precipitation process and resulted in an average hydrodynamic LNP with a diameter of 180 nm. Cytological and animal tests were conducted and showed the presence of high anticancer effects, enhanced by in vitro RSV release. Moreover, LNPs showed a high drug-loading capacity of over 20 wt %, as well as reduced adverse effects compared to free RSV.

The use of sunscreens is essential for preventing skin damage and the potential appearance of skin cancer in humans. Lignin is found to significantly boost the sunscreen performance[99]. The presence of organosolv lignin (OL) in a basic sunscreen formulation can increase the Sun protection factor (SPF) in a significative amount. Moreover, the UV absorbance of lignin-modified sunscreen lotions was found to increase during the irradiation. Inorganic active components such as zinc oxide (ZnO) are commonly used in sunscreens due to their ability to block UVA radiation. This ultraviolet protection might be enhanced to cover the UVB frequency when combined with other components such as titanium dioxide (TiO_2). The photoprotection properties of organic nanoparticles made from lignin in combination with ZnO nanoparticles as active ingredients for sunscreens was evaluate by Toriz et al.[100]. Lignin nanoparticles were synthesized from *Agave tequilana* lignin and then mixed with a zinc oxide in different concentrations showing enhanced in-vitro sun protection factor (SPF) by boosting and synergistic effect.

Other applications of nanostructured lignin have been reported as biocide[101], due to natural antimicrobial activity of lignin[102], and as antioxidant/radical scavenger[103,104].

1.4 Bio-nanocatalysts: procedure for their preparation and applications

The biotechnology uses enzymes in various industrial processes, such as fine-chemical synthesis, pharmaceuticals, biosensors, and biofuel cells[105]. To improve enzyme stability and recovery, the immobilization of the active species on solid support has been developed during the time[106]. Nanomaterials can serve as excellent supporting materials for enzyme immobilization, because they offer the optimal equilibrium between the efficiency of the biocatalyst (including surface area, minimized mass transfer resistance, etc) and the effective enzyme loading[107].

Carbon nanotubes and lignin nanospheres are receiving a great deal of attention as alternative matrices for enzyme immobilization. These supports are supporting materials for enzyme immobilization with improved properties with respect to other common supports, like zirconia, silica, and epoxy resins.

CNTs are more stable under harsh condition, provide higher loading of enzyme, and enhanced catalytic activity of enzyme up to 2-fold greater than flat support and up to 10 times higher than native enzyme. Besides exhibiting extraordinary mechanical, electrical, and thermal properties, also provide high surface area for high values of the enzyme loading, reduced diffusion limitations, and a biocompatible microenvironment that helps enzymes to retain its catalytic properties[108]. Apart from proteins, other biological molecules can also be immobilized on these carriers such as nucleic acids, antigens, peptides, and drugs. The type of biomolecule immobilized on the CNTs lead to different applications which renders these conjugates of great versatility.

A wide variety of natural polymers, mainly water-insoluble polysaccharides like collagen, chitosan, alginate, cellulose, starch, agarose, etc., have been used as support matrix for the enzyme immobilization. The characteristic features of these polymers that make them good support systems include the avaibility in large quantities, the low cost, the high thermal and mechanical resistance, and the ability to form inert gels. Moreover, due to their chemical structure which can be activated easily, they can bind to proteins and enzymes in a reversible and irreversible way.

The interaction between lignin and protein has been also widely studied. Recent research on lignin model films reported that proteins and peptides adsorb easily on lignin surface[109]. Still, proteins are complex 3D-structured molecules and fundamental knowledge on amino acid specific interactions and influence of protein fold structures on

their interaction with the lignin surface remains limited. Aromatic and charged amino acid side-chains[109,110,111] are essential for lignin interactions, as confirmed by studying different aminoacid mutations on the binding face. Recently, Yamaguchi et al. (2016)[112] showed the importance of various amino acid side-chains on lignin interactions using synthetic 12-mers.

Immobilization Approaches

The immobilization of enzymes on appropriate supports is of central relevance for the design of bio-transformations and of novel biosensoring technologies. An immobilized molecule is a molecule whose movement in space has been restricted either completely or limited to a small region of space. Expensive and rare enzymes are not favored to be used in industries in the free state as they are difficult to be separated from the products and consequently are lost after the first use. Alternatively, enzymes can be immobilized on solid supports so that they can be easily separated from the products by simple filtration. The main advantage for enzyme immobilization is the easy separation of the enzyme from the reaction mixture (substrates and products) and its reusability, which reduces the cost of the overall process. Beside this advantage, the immobilization process imparts many other advantages to the enzyme such as: (a) the ability to stop the reaction rapidly by removing the enzyme from the reaction mixture; (b) product is not contaminated with the enzyme; and (c) the stability of the enzyme activity is gained with respect to pH, temperature, solvent, contaminants, and impurities modifications (Figure 1.11).

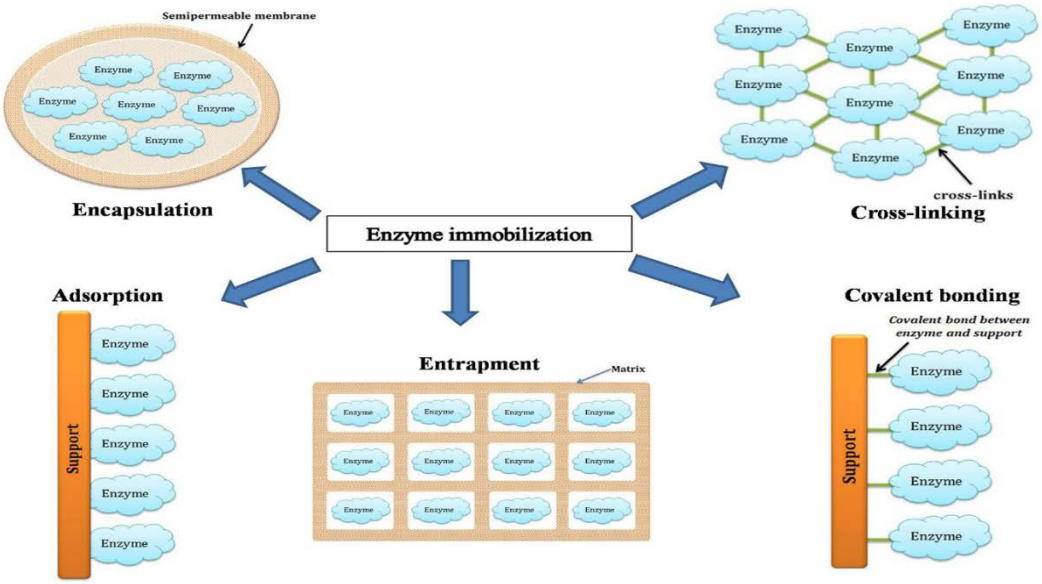

Figure 1.11. Representation of different enzyme immobilization pathways.

There are five principal methods for the immobilization process of enzymes and cells, namely adsorption, covalent, entrapment, encapsulation, and crosslinking procedures, and any of these methods is perfect for all molecules or purposes.

Non covalent procedure

The noncovalent approach is considered to be a more promising technique, because it comprises less distortion of the conformational structure of the enzymes[113]. In the adsorption procedure, the enzyme adheres to the surface of the carrier matrix by a combination of hydrophobic interactions and salt-like linkages. The process involves the simple suspension of the support with the enzyme or the deposition of the enzyme on a specific support. In this case, physiological conditions like high temperature or pH, may weaken the interaction between the enzyme and the support. The adsorbed enzymes are usually resistant to proteolysis and aggregation because of their hydrophobic interaction with the interface[114]. For example, the presence of OH moieties in silanized molecular sieves facilitate enzyme immobilization by hydrogen bonding[115]. For better immobilization, different chemical modifications of the support matrices would be promising.

The adsorption of protein onto the CNTs involves both hydrophobic and electrostatic interactions[116]. Pristine CNTs being highly hydrophobic will contribute to hydrophobic interaction through interaction of the side chains of hydrophobic amino acids of the proteins with the sidewall of CNTS. As for the electrostatic interaction, the electrons on the surface of the CNTs will interact with the electrons of the aromatic ring of amino acids (e.g., phenylalanine and tryptophan). Apart from electrostatic and hydrophobic interaction, hydrogen bonds, and nonspecific adsorption can also play a role for enzyme adsorption onto CNTs[113].

Whether the protein adsorption on different surfaces is driven by specific (e.g. ion pairing or hydrogen bonding) or non-specific mechanisms, such as hydrophobic driving force, is under debate[117]. Recently studies explain that peptides containing histidine, phenylalanine, proline, and serine residues had the best affinity to the lignin surface. Furthermore, the botanical origin of lignin was shown to affect peptide-lignin interactions. Besides a number of potentially interacting amino acid side-chains within a protein fold, alteration of their accessibility by denaturation influences proteins adsorption on lignin surfaces[110]. Penna et al.[118] proposed that protein adsorption on

hydrated surfaces occurs in different stages by a “statistical zippering” effect, mediated by strongly interacting amino acid side-chains.

Another interesting approach is the Layer by Layer (LbL) technique. Generally, this technique involves the sequential deposition of opposite charged polyelectrolytes, spontaneously stabilized by their electrostatic attraction (figure 1.12).

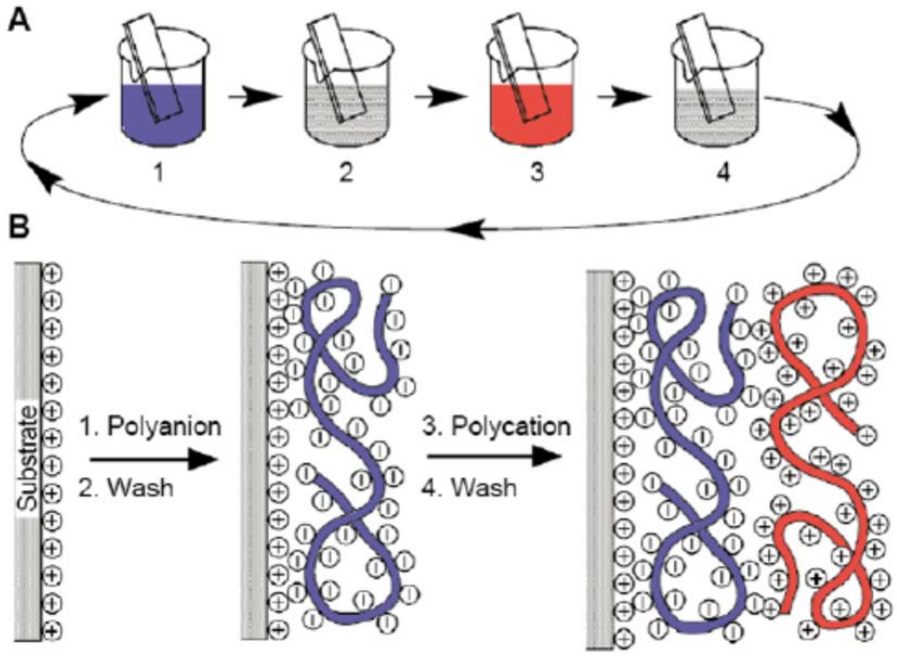

Figure 1.12. Schematic representation of Layer-by-layer procedure

LBL is a technique that finds application in different fields. In general, both carbon nanotube and lignin nanosphere, possessing a negative surface charge, can interact with cationic polyelectrolytes, increasing the possibility of immobilization of enzymes. In various projects described in this thesis work, the LBL technique was used with both natural and synthetic polyelectrolytes.

Covalent procedure

The covalent procedure requires the formation of covalent bond between the enzyme and the support. Covalent bond formation between the enzyme and the support usually happens through the side chain of amino acids like histidine, arginine, aspartic acid, etc. However, the specific reactivity depends on the presence of different functional groups such as carboxyl, amino, indole, phenol, sulfhydryl, thiol, imidazole, and hydroxyl groups. By preventing the active site amino acid residues inactivation, efficient enzyme activities can be achieved. Widely used protective strategies are:

1. Covalent binding of the enzyme with the matrix in the presence of substrate or a competitive inhibitor.
2. Formation of a reversible covalently linked enzyme–inhibitor complex.
3. Covalent linkage of a chemically modified soluble enzyme to the matrix obtained by incorporating new residues.
4. Zymogen precursor.

The covalent functionalization of CNTs can generally be achieved by two main approaches: (i) esterification or amidation of oxidized CNTs; and (ii) sidewall covalent attachment of functional groups[119]. An efficient one-step method for covalent attachment of alkyl groups terminated with a carboxylic acid to the sidewalls of carbon nanotubes have been performed[120].

Linking molecules which act as "bridge" between the support and protein are frequently used for covalent immobilization of protein and enzymes onto CNTs. They bind to CNTs through hydrophobic and π-π interactions[121] and also covalently bind the enzyme through, for example, an amide bond.[122] These linking molecules present advantages in the immobilization of enzymes. For example, the highly reactive succinimidyl ester groups were used for the immobilization of horseradish peroxidase on CNTs by reaction with 1-pyrenebutanoic acid succin1imidyl ester as the linking molecule[121]. Any covalent immobilization procedures is present day available for the functionalization of lignin nanospheres.

The entrapment procedure

The entrapment procedure is based on the caging of the enzyme within a polymeric network by covalent or noncovalent bonds that allow the passage of substrate and products but retain the enzyme[123]. In this method the enzyme is not bound to the support matrix unlike other methods which are described earlier. The caging of enzyme can be achieved by any of the following strategies: (1) inclusion of the enzyme within a highly cross-linked polymer matrix; (2) enzyme dissolution in a nonaqueous phase; (3) separation of the enzyme by the bulk solution using a semipermeable microcapsule.

Encapsulation of enzymes can be accomplished by wrapping the biological components inside different forms of semi permeable membranes [28,29]. Large proteins or enzymes cannot out or inter capsule, however small substrates and products can go freely

across the semi permeable membrane. Numerous materials have been utilized to form microcapsules in the 10-100 μm range of diameter; such as, nylon and cellulose nitrate.

Biological cells also may be used as capsules, and a famous example of this is the use of erythrocytes (red blood cells). The membrane of the erythrocytes is normally just permeable to small molecules. However, when erythrocytes are placed in hypotonic solution, they swell, expanding the cell membrane and substantially expanding the penetrability. In this condition, erythrocytes proteins go out of the cell and enzymes can inter into the cell.

Lignin nanosphere are excellent candidates for encapsulating enzymes for many applications[124]. The nanometric cavity allows to accommodate macromolecules and to protect them from aggressive microenvironments.

Chapter 2
Bio-nano technologies

2.1 Natural coating based on polyphenols to protect metal surfaces

The extraordinary stability of gold has been the focus of study since ancient times. Gold's resistance to oxidation and corrosion has led to its use in such diverse applications as the decorative gold leaf found on the exteriors of temples in Asia, the reflective coatings used in sun visors for astronaut spacesuits,[125] the caps and crowns in common use for dental work, the coinage and jewelry that have become a store of wealth in most cultures, and the metal of choice for a wide range of nanoparticle studies where biocompatibility is a concern. Gold nanoparticles also have become the focus of increasing interest in part due to their potential optical, electronic, and catalytic applications. The discovery of the relative ease of generating self-assembled monolayers (SAMs) via the adsorption of a variety of surfactants onto two-dimensional or "flat" gold substrates has dramatically increased the number of applications that utilize gold surfaces. SAMs have also been developed for a broad array of surfaces other than gold due to the many potential applications for these protective coatings in nanotechnology.

Details of the formation, characterization, properties, and/or applications of protected flat surfaces and gold nanoparticles have been reviewed[126]. Owing to the intense interest in the potential of such nanoscale coatings, one of the topics that has been widely studied is the need to enhance the stability of SAMs. Although several review articles have described the study and use of SAMs on flat gold and/or gold nanoparticles[127], none of these reviews has focused specifically on the issue of monolayer stability, save for a brief summary in the article by Salvarezza and co-workers[128].

This research project originated from an agreement between the University of Tuscia and the Valmet company, specialized in the recovery of noble metals from RAEE wastes and the reuse for high fashion costume jewelery.

The purpose of this convention was to design and develop a protection for surfaces that had a final galvanic coating of gold. However, this protection had to maintain the visual qualities of the treated object unaltered, to be easy to prepare without the need to use non-eco-friendly compounds.

Each developed protection was applied to helical-shaped testers that had a thin galvanic coating of gold, supplied by Valmet. Each tester that was treated with a type of protective was then subjected to certain chemical and physical stresses internally by the company in order to give the result of each test with a score.

The first approach was to exploit the chemistry of sulfur and therefore its known affinity with gold and other noble metals[129]. For several years this type of approach has been used to design new functional sulfur compounds able to have both affinity with gold and the possibility of creating cross-link bonds. The organization of organic molecules into monolayer films through self-assembly provides a facile method of preparing surfaces with a well-defined composition, structure, and thickness, and permits the control of chemical and physical properties of the surface. One type of film that exhibits these properties is obtained from the adsorption of n-alkyl organosulfur compounds to gold surfaces[130] (figure 2.1).

The self-assembly process is driven through the formation of chemisorptive bonds between the thiol and the gold surface, increased van der Waals interaction between the alkyl chains, and increased entropy of the system as a result of removal of the solvation layer around the thiol molecules (40-45 kcall mol).

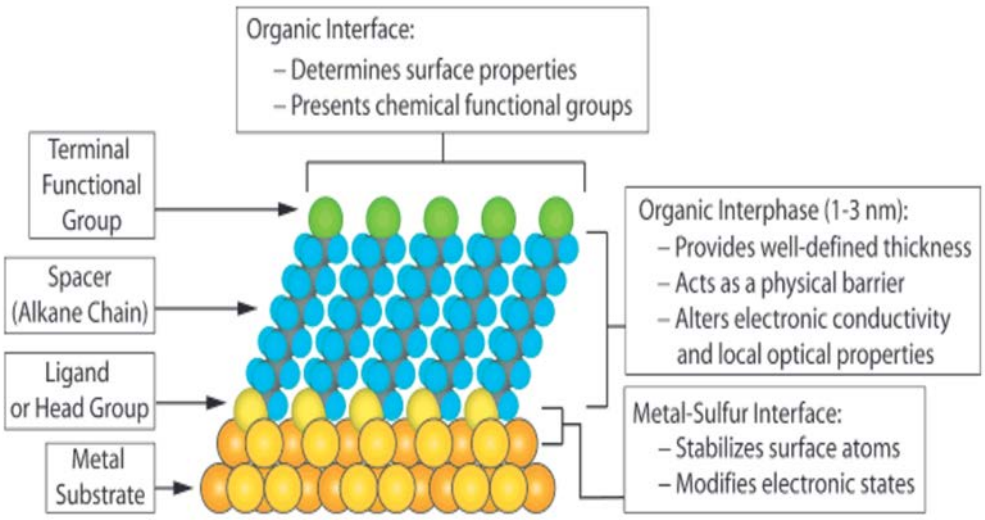

Figure 2.1. Schematic representation of spontaneous ordinated organization of sulfur monolayer

When a gold surface is exposed to alkyl thiol solutions an ordered alkyl thiol monolayer forms at the gold surface[131]. Properties of the deposited film can be modified by varying the length of the hydrocarbon chain and by attachment of different functional groups at the opposite end of the alkyl thiol. Incorporation of functional groups allows the control of the chemical and physical properties at the external surface of the self-assembled membrane. Alkyl thiols with over 10 carbons in the alkyl chain form a densely packed crystalline-like monolayer assembly with an extended all-trans alkyl chain tilted 20-30" to the normal surface [131].

Before applying the various designed coatings, three different selected alkylthiol (see Figure 2.2) were evaluated without further treatment. The application provides a thorough cleaning procedure to remove all traces of dirt from the surface (dust, grease, solvents, etc.): the plate is immersed in 3 different boiling solvents (2-isopropanol, $CHCl_3$, Acetone) and then dried. The deposition of the alkanethiol was carried out by immersing each plate in a 5 mM ethanolic solution of the corresponding monomer for 24 hours under magnetic stirring. Finally, after the treatment each sample was dried at 60 °C for 2 hours. This procedure was used in each type of coating described below as the first initial step.

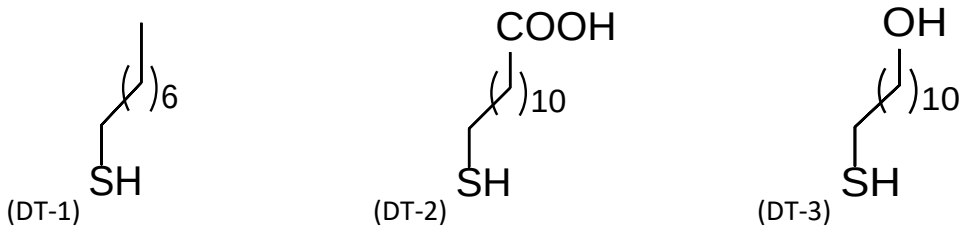

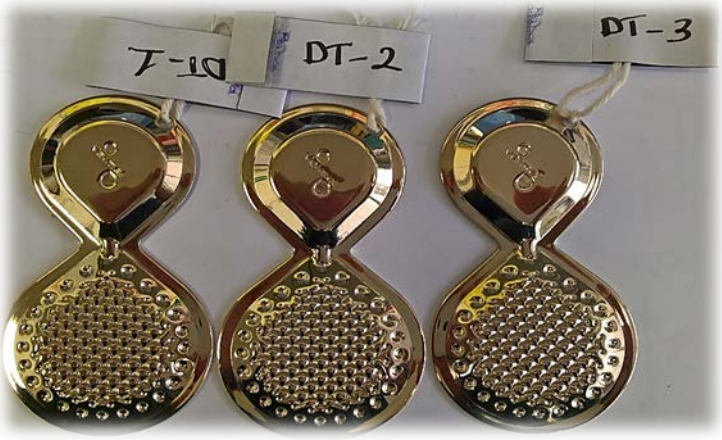

Figure 2.2. Molecular structure of thiols used for gold coating: mercaptoctane (DT-1), mercaptoundecanoic acid (MUA, DT-2) and mercaptoundecanol (DT-3).

Pathway A-1

The first coating procedure studied initially provided the deposition of DT-2 as described above. Thereafter the carboxylic functions of thiol were reacted with DIC (10mM) and NHS (10mM) in of MES buffer (50 mM, pH 6.0) for 3h at 25C° to form active ester groups. Afterwards, the substrates were rinsed with milli-Q water and immersed in isopropyl alcohol (IPA) containing ethylendiammine (ED) 1M. The

resulting substrates were rinsed thoroughly with Milli-Q water and dried under nitrogen flow.

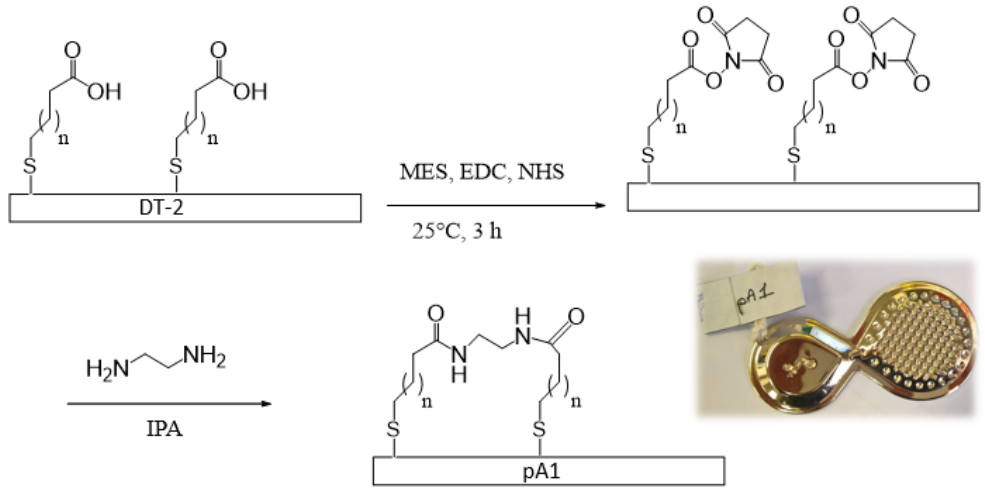

Figure 2.3. Schematic representation of chemical procedure for the pathway A-1

Pathway A-2

The first coating procedure studied provided the deposition of DT-2 as described above. Thereafter, the carboxylic functions of thiol were reacted with DIC (10mM) in MES buffer (50 mM, pH 6.0) for 3h at 25C° to form active ester groups, as in pA-1 procedure.

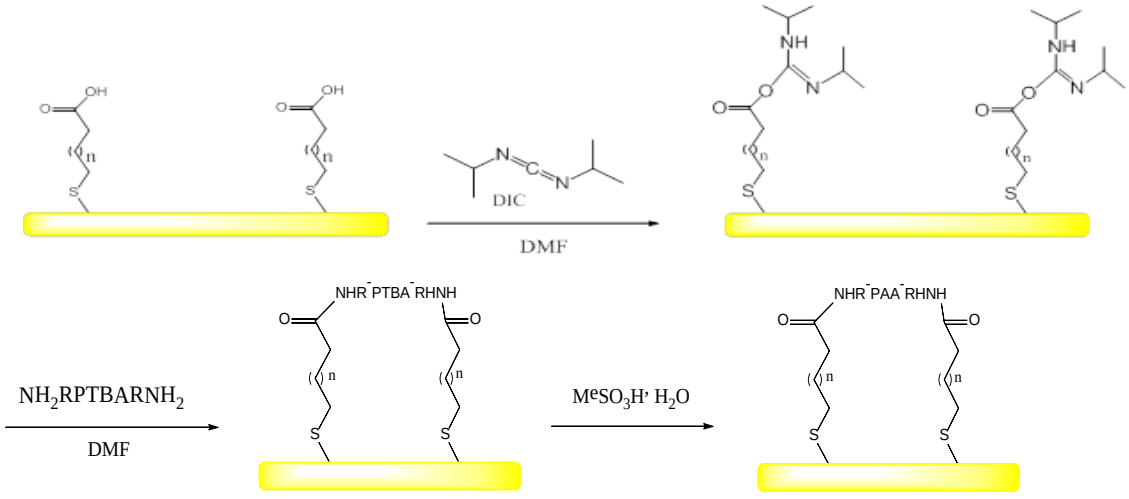

PTBA= poly-tert-butyl acrylate
PAA= poly acrylic acid

Figure 2.4. Schematic representation of chemical procedure for the pathway A-2

The active MUA substrate was reacted with diamino-terminated poly(tert-butylacrylate)(H_2NR-PTBA-RNH_2,$R=CH_2)_2NHCO(CH_2)_2C(CN)(CH_3)$) prepared following the reported procedure[132], to yield the amide-grafted polymer layer. The hydrolysis of PTBA with $MeSO_3H$ yielded the first layer of PAA. All activation, grafting, and hydrolysis steps were carried out at room temperature. The resulting substrates were rinsed thoroughly with Milli-Q water and dried under nitrogen flow.

Pathway A-3

The alcoholic functions of the thiols were reacted with the TDI in order to crosslink. The two isocyanate groups in TDI react at different rates: the 4-position is approximately four times more reactive than the 2-position. 2,6-TDI is a symmetrical molecule and thus has two isocyanate groups of similar reactivity, similar to the 2-position on 2,4-TDI. However, since both isocyanate groups are attached to the same aromatic ring, reaction of one isocyanate group will cause a change in the reactivity of the second isocyanate group.

The alcoholic functions of the thiols were reacted with the TDI. The reaction occurred in DMF at 60 °C in the presence of 10 mM of TDI.

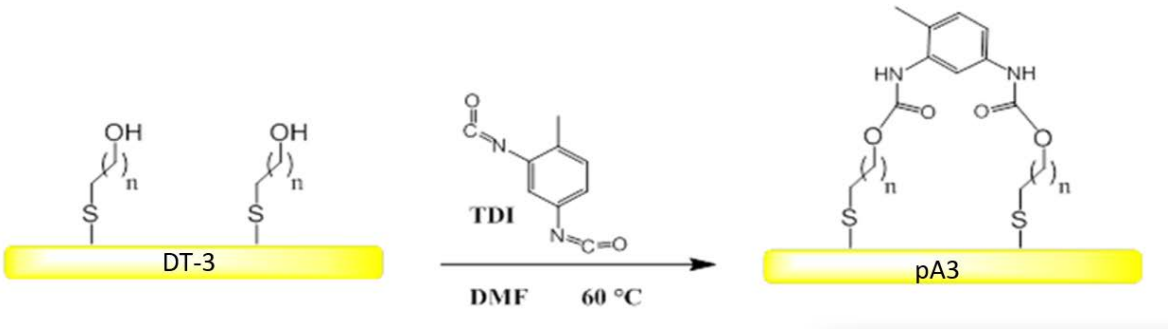

Figure 2.5. Schematic representation of chemical procedure for the pathway A-3

Pathway B

In present day, the surface coating technology to produce monolayers of functional molecules gained impressive results[133]. Polydopamine films[134] or films made from polyphenols[135] can be deposited on almost all known materials in one step from aqueous solutions and without complicated equipment. The development of these films relied on a biomimetic approach: the strong interactions between mussel foot proteins rich in l-lysine and in L-dopa with almost all surfaces. Many applications in the field of energy

storage and in the development of antibacterial and anti-inflammatory coatings immediately emerged from these first investigations on polyphenol coatings[135]. In particular, polyphenol-based films allow for good cell (3T3fibroblasts) adhesion and to scavenge radical and non-radical reactive oxygen species[135]. Controlled polyphenol-based reduction of metal cations can be performed when polyphenols are confined in polyelectrolyte multilayer films[136]. These are just few examples of possible applications of polyphenol-based films in diverse domains of surface science.

Therefore, this pathway was largely oriented towards a more eco-sustainable philosophy, thus replacing organic solvents with water and synthetic compounds with natural polyphenols, leaving the more complicated sulfur chemistry.

This approach consists of immersing the tester in the presence of different polyphenols aqeous solution (tannic acid and/or lignin sulfonate) at different concentrations (see table 2) for 12 hours under gentle magnetic agitation at room temperature in the dark.

		Procedure name			
		pB-1	**pB-2**	**pB-3**	**pB-4**
Monomer	**LS**	0.50 mg/mL	-	0.25 mg/mL	0.25 mg/mL
	TA	-	0.50 mg/mL	0.25 mg/mL	0.25 mg/mL
	MUA	-	-	-	5.0 mM

Table 2. Concentration and type of the polyphenol used for each treatment.

The various coating procedures were evaluated internally by the company using the following physical chemical tests: oxidation with sulfur dioxide (SO_2), resistance to moist heat, resistance to salt fog, resistance to thioacetamide and resistance to synthetic sweat. Based on the outcome of the resistance examination, a score of 1 (no resistance) to 5 (perfect resistance) was assigned. The table 3 shows the results for each type of treatment compared with a blank and with a homemade product already used by the company (Helmet).

CHEMISTRY STRESS

COATING PROCEDURE	SO_2 oxidation	moist heat	salt fog	thioacetamide	synthetic sweat
pA-1	3	3	2	3	2
pA-1	3	3	3	3	2
pA-1	2	3	2	3	2
pB-1	5	4	4	4	4
pB-2	4	4	5	4	5
pB-3	4	5	4	4	4
pB-4	4	4	4	4	5
Helmet	4	4	4	4	4
blank	1	2	1	2	1

Table 3. Score assigned from the company based on resistance of each kind of coating under different chemistry stress.

The results demonstrated the greater effectiveness of polyphenol-based coatings compared to those from sulfur chemistry. Generally, polyphenol-based treatments have achieved the same results as the HELMET commercial product but with the important difference in simplicity of preparation, high eco-sustainability and low cost.

2.2 Layer-by-Layer Preparation of Microcapsules and Nanocapsules of Mixed Polyphenols with High Antioxidant and UV-Shielding Properties

2.2.1 Aim of work

In recent years microcapsules and nanocapsules containing renewable materials have been prepared in order to explore innovative pharmaceutical and technological applications[137]. The main advantage of these devices resides in the high biocompatibility and in the emergence of specific scale-dimensional chemical and physical properties[138]. Present day, capsules containing only one type of polyphenol have been described, irrespective to the nature of the starting materials and to the specific preparation procedure. On the other hand, capsules of mixed polyphenols are expected to increase the physical and chemical properties with respect to their simple homo-polymer counterpart, as a consequence of possible synergistic effects between the different active components. The Layer-by-Layer (LbL) procedure, consisting on the sequential deposition of polyelectrolytes with opposite electrical charge, is a pivotal tool for the preparation of multicomponent devices[16], allowing the assembly of different compounds by electrostatic, dipole-dipole, hydrogen bonds, and van der Waals interactions.[139] In these systems, one layer is responsible for the chemical and physical properties, while the remaining one is mainly involved in the stabilization of the overall structure[140].

We studied the layer-by-layer preparation of microcapsules and nanocapsules of mixed polyphenols, sulfonate lignin (LS) and TA, using $MnCO_3$ and organosolv lignin nanoparticles as core templates, and polydiallyldimethylammonium chloride (PDDA) and chitosan (CH) as supporting layers. LS is a no toxic raw lignin produced in large amount during the sulfite pulping industrial process.

The novel microcapsules and nanocapsules showed antioxidant activity, UV-shielding properties, and electrochemical responsiveness higher than that of the respective homo-polymer counterparts, confirming the beneficial role of the contemporary presence of two different polyphenols in enhancing both chemical, physical and biological properties. These devices are useful ingredients in different application fields, such as the preparation

of bioplastics[89], drug delivery technology[98] and sunscreen development in cosmetic and cosmeceutical formulations[142].

2.2.2 Experimental Part

Materials

Tannic acid (TA, 90% pentagalloyl glucose, SigmaAldrich), chitosan (CH, low molecular weight) with 20% chitin units, sulfonate lignin calcium salt (LS, Mw ~18,000, average Mn ~2,500), organosolv lignin (OL), poly(diallyldimethylammonium chloride) (PDDA, 20%v/v water solution), poly(sodium 4-styrenesulfonate) (PSS), deuterated chloroform ($CDCl_3$), ethylenediaminetetraacetic acid (EDTA), 2-chloro-4,4,5,5-tetramethyl-1,3,2-dioxaphospholane, chrome (III) acetylacetonate, and 2,2-diphenyl-1-picrylhydrazyl (DPPH), were purchased from Sigma-Aldrich and were used without any further purification. Ascorbic acid (AA), 2,2'-Azino bis(3-ethylbenzothiazoline-6-sulfonic acid) (ABTS), boric acid (H_3BO_3), acetic acid (CH_3COOH), ortophosphoric acid 85% (H_3PO_4), potassium persulfate ($K_2S_2O_8$) and potassium chloride (KCl) were purchased from Sigma-Aldrich (Buchs, Switzerland). All solutions were prepared using Milli-Q water (ρ = 18.2 MΩ cm a 25 °C; TOC < 10 μg L^{-1}, Millipore, Molsheim, France).

Preparation of microcapsules

The microcapsules were prepared by the LbL protocol, consisting in the sequential addition of polyelectrolytes with different electric charge to inorganic particles used as templates[143]. Briefly, the sodium acetate solution (0.5 mL, pH 5.0) of the appropriate polyphenol (1 mg/mL; LS or TA as negative charged layer), and of the appropriate polyelectrolyte (1 mg/mL; PDDA or CH as positive charged layers), were alternatively added to $MnCO_3$ particles suspension (20 mg suspended in 4.0 mL in sodium acetate solution pH 5.0) at room temperature. After 20 min, the solution was centrifuged (6000 rpm, 20 min) and the supernatant removed. Experiments were performed by deposition of three and five couple of layers. At the end, the microcapsules were $MnCO_3$ core was dissolved with EDTA (3 mL, 0.1M; pH 5) to yield empty microcapsules with general formula (X/Y)n, where X and Y are the different polyphenol and polyelectrolyte in the sequential deposition order with respect to the inorganic core, and "n" represents the total number of coupled layers. Microcapsules $(PDDA/LS)_3$ **1**, $(PDDA/LS)_5$ **2**, $(CH/LS)_5$ **3**,

$(PDDA/TA)_5$ **4**, $(CH/TA)_5$ **5**, $(PDDA/TA/PDDA/LS)_5$ **6**, $(CH/TA/CH/LS)_5$ **7** and $(PDDA/LS+TA)_5$ **8** (where LS+TA is the mixture of sulfonate lignin and tannic acid in the 1:1 ratio) were prepared and successively characterized. Homo-polyphenol microcapsules **1**-**5** were used as references for the mixed polyphenol systems **6**-**8** in the chemical and physical assays.

Preparation of nanocapsules

Nanocapsules were prepared by the dialysis protocol using nanoparticles of organosolv lignin (OL) as organic template.[11] Briefly, commercially available OL (20 mg) was dissolved in THF (20 mL), followed by filtration (0.45 μm syringe filter) and dialysis against deionized water for 24h at 25°C. The solution (1 mL; sodium acetate buffer pH 4.5) of the appropriate polyphenol (0.5 mg/mL; LS or TA as negative charged layer), and of the appropriate polyelectrolyte (0.5 mg/mL; PDDA or CH as positive charged layers), were alternatively added to 30 mL of previously prepared organosolv lignin nanoparticles (NOL) in sodium acetate buffer (0.1 mL/mg; sodium acetate buffer pH 4.5) at room temperature. After 20 min, the solution was centrifuged (6000 rpm, 20 min) and the supernatant removed. Experiments were performed by deposition of five couple of layers. The nanocapsules were rinsed with deionized water, recovered by centrifugation (6000 rpm, 20 min) and lyophilized to yield nanocapsules with general formula (X/Y)n, where X and Y are the different polyphenol and polyelectrolyte in the sequential deposition order with respect to the organic NOL ore, and "n" represents the total number of coupled layers. Nanocapsules $NOL(CH/TA)_5$ **9**, $NOL(CH/LS)_5$ **10** and $NOL(CH/TA/CH/LS)_5$ **11**, were prepared and characterized. Nanocapsules **10**-**11** were used as references for the mixed polyphenol system **9**. The mass percentage of polyphenols in microcapsules and nanocapsules has been evaluated by use of the Folin-Ciocalteu assay to measure the amount of polyphenol content in the residual solution after any layer deposition[144]. As reported in Table 4, microcapsules and nanocapsules showed a similar total amount of coated polyphenol.

Typically, the calibration curve was prepared using gallic acid solution as standard at different concentrations (20%, 40%, 60% and 80% from a 10 mg/mL starting solution). The samples were obtained from the residual solutions recovered during the layer-by-layer deposition, and were analyzed at the appropriate dilution factor after addition of 800 μL of $NaCO_3$ (5% water solution) and Folin (100 μL) reagent at 40 °C for 20 min. Finally, the samples were analyzed at 560 nm by UV-vis spectrophotometer. The total amount of

polyphenols (mg of polyphenols for mg of capsules) was calculated as a difference between the starting amounts of polyphenol with respect to the recovered one in the residual solutions. Note that the various types of microcapsules and nanocapsules did not released appreciable number of polyphenols in the solution after 7 days of storage in water (pH 7.0) at room temperature, as evaluated by UV-vis analysis (Folin-Ciocalteu assay). Similarly, the novel capsules showed mechanical stability as they retained the original spherical shape under similar experimental conditions in optical microscopy analysis (Leitz. Ergolux AMC).

Table 4. Total amount of polyphenols deposited in microcapsules and nanocapsules.

Entry	Sample	Adsorbed polyphenols (mg/mL)
1	$(PDDA/LS)_3$ **1**	0.45
2	$(PDDA/LS)_5$ **2**	0.47
3	$(CH/LS)_5$ **3**	0.51
4	$(PDDA/TA)_5$ **4**	0.46
5	$(CH/TA)_5$ **5**	0.52
6	$(PDDA/TA/PDDA/LS)_5$ **6**	0.52
7	$(CH/TA/CH/LS)_5$ **7**	0.55
8	$(PDDA/LS+TA)_5$ **8**	0.54
9	$NOL(CH/TA)_5$ **9**	0.58
10	$NOL(CH/LS)_5$ **10**	0.59
11	$NOL(CH/TA/CH/LS)_5$ **11**	0.69

[a]The amount of polyphenols is expressed as mg of adsorbed polyphenols for mg of each capsule. All experiments were conducted in triplicate.

Electron microscopy analysis

For Scanning Electron Microscopy (SEM), microcapsules **1-8**, and nanocapsules **9-11** were fixed with 3% glutaraldehyde in 0.1 M cacodylate buffer (pH 7.2), washed and post-fixed in OsO_4 (1% weight) in the same buffer at room temperature. Specimens were dehydrated in a graded ethanol series. They were then air dried, sputter-coated with gold in a Balzers MED 010 unit. The bservation was made by a JEOL JSM 6010LA electron microscope. For Transmission Electron Microscopy (TEM), nanocapsule **11** was fixed and dehydrated as described above and embedded in LRWhite resin (Multilab Supplies, Surrey, England) as a selected sample. The resin was polymerised in tightly capped gelatine for 48 h at 50°C. Thin sections were cut with Reichert Ultracut and LKB Nova ultra-microtomes using a diamond knife, collected on copper grids, stained with uranyl acetate and lead citrate, and observed with a JEOL 1200 EX II electron microscope.

Micrographs were acquired by the Olympus SIS VELETA CCD camera equipped the iTEM software.

Phosphorus Nuclear Magnetic Resonance ^{31}P-NMR analysis

The qualitative and quantitative analysis of phenolic moieties in microcapsules and nanocapsules was determined by ^{31}P-NMR analysis[145]. Typically, the appropriate sample (10 mg) was dissolved in pyridine/$CDCl_3$ (300 μL; 1.6/1.0 v/v), followed by addition of chrome (III) acetylacetonate solution 50 μL, 11.4 mg/ml) as relaxing agent. Then, the phosphitylation reagent 2-chloro-4,4,5,5- etramethyl-1,3,2-dioxaphospholane (200 μl) was added under magnetic stirrer and gentle heating at 45 °C for 2 hours. NMR analysis was performed in the presence of cholesterol as an internal standard on a Bruker 400MHz apparatus. The total amount of characteristic OH groups of polyphenols in microcapsules and nanocapsules was evaluated by comparing the ^{31}P NMR integral area of each specific signal with respect to standard reference. The ^{31}P NMR (ppm) characteristic range for any OH groups have been derived from data in the literature[146].

Antioxidant activity

The antioxidant activity of selected microcapsules $(CH/LS)_5$ **3**, $(CH/TA/CH/LS)_5$ **7** and $(PDDA/LS+TA)_5$ **8**, and of nanocapsules NOL$(CH/LS)_5$ **10** and NOL$(CH/TA/CH/LS)_5$ **11**, was evaluated by the 2,2'-diphenyl picrylhydrazyl (DPPH) radical scavenging analysis[147]. using the same concentration of polyphenols (0.5 mg/mL). Briefly, the appropriate amount of the sample (depending on data in Table 4) was dissolved in EtOH 60% and added to freshly prepared DPPH solution (6 x10^{-5} M in MeOH). The decrease in absorbance (517 nm) was determined at different times and concentrations until the reaction reached a plateau. The kinetic of the process was analyzed for each concentration tested, and the rate of DPPH remaining at the steady state was estimated. This value was used to calculate the IC_{50} (defined as the concentration of substrate in μg/mL that causes 50% loss of DPPH activity). The data were expressed as percentage of inhibition of the DPPH activity and were calculated according to the following equation: % inhibition of DPPH = {(Abs control - Abs sample)/Abs control} × 100 where "Abs control" is the absorbance of the DPPH solution without the sample.

UV shielding assay

The UV absorption properties of micro and nano-capsules, were spectrophotometrically determined by Varian Cary UV 50 scan using the same concentration of polyphenol (0.1 mg/mL). The analysis was carried out thought UV-vis scan using deionized H_2O suspension (pH 7) of the appropriate amount of sample (depending on data in Table 1) in quartz cuvette (3.0 mL), working in the range from 190 nm to 600 nm at 25°C under gentle stirring.

Electrochemical analyses

Cyclic voltammetry and amperometric experiments were performed by using a PGSAT204N potentiostat (Eco Chemie, The Netherlands) controlled by Nova 2.1 software (Eco Chemie, The Netherlands), using a conventional three-electrodes electrochemical cell equipped with a modified glassy carbon (GC) electrode as working electrode (d=3 mm, Cat. 6.1204.300, Metrohm, Herisau, Switzerland), and a saturated calomel electrode (SCE, 244 mV vs. NHE, Cat. 303/SCG/12, AMEL, Milano, Italy) and a glassy carbon rod electrode (d=2 mm, Cat. 6.1241.020, Metrohm, Herisau, Switzerland) as reference and counter electrodes, respectively. Cyclic voltammetry experiments were performed in 120 mM Britton-Robinson buffer pH 6.5 + 100 mM KCl containing 250 μM ABTS as mediator, while the pH experiments were performed by varying the pH of Britton-Robinson buffer in the range 2.5-7.5. Amperometric experiments were performed in 120 mM Britton-Robinson buffer pH 6.5 + 100 mM KCl injecting $ABTS^{+\bullet}$ radical solution (7mM) followed by sequential addition of ascorbic acid (AA) as antioxidant.

Electrode preparation

GC electrodes (d=3 mm, Cat. 6.1204.300, Metrohm, Herisau, Switzerland) were polished with alumina slurries (Al_2O_3, particle size of 0.3 and 0.05 μm) on cloth pads wet with Milli-Q water (SIEM, Bologna, Italy), thoroughly rinsed with Milli-Q water and further sonicated for 5 min between each polishing step. For the bio-modification, GC electrodes were modified by drop casting 5 μL of the appropriate sample (2 mg/mL). For each different modification, three replicates have been performed.

Amperometric antioxidant activity experiments

In order to prepare in situ the $ABTS^{+\bullet}$ radical cation, $K_2S_2O_8$ (140 mM, aqueous solution) was added to ABTS (2.5 mL; 7 mM, aqueous solution) at 4 °C for 8h.

Afterwards, 1.0 mL of the so prepared solution was injected in 10 mL of 120 mM Britton-Robinson buffer pH 6.5 containing 100 mM KCl as supporting electrolyte. Next, 30 µL of 1 mM AA solution were sequentially injected. The potential applied for the analysis was 0.550 V vs. SCE.

2.2.3 Result and discussion

Preparation of microcapsules of mixed polyphenols

The LbL procedure for the preparation of microcapsules of mixed polyphenols is reported in Figure 2.6. LS and TA were used as negative charged polyelectrolytes, PDDA and CH as positive charged counterparts. We started with the deposition of the first positive layer in accordance with the slightly negative charge showed by the surface of $MnCO_3$ particles[148]. Microcapsules containing LS and TA alone, associated to PDDA, were also prepared as references.

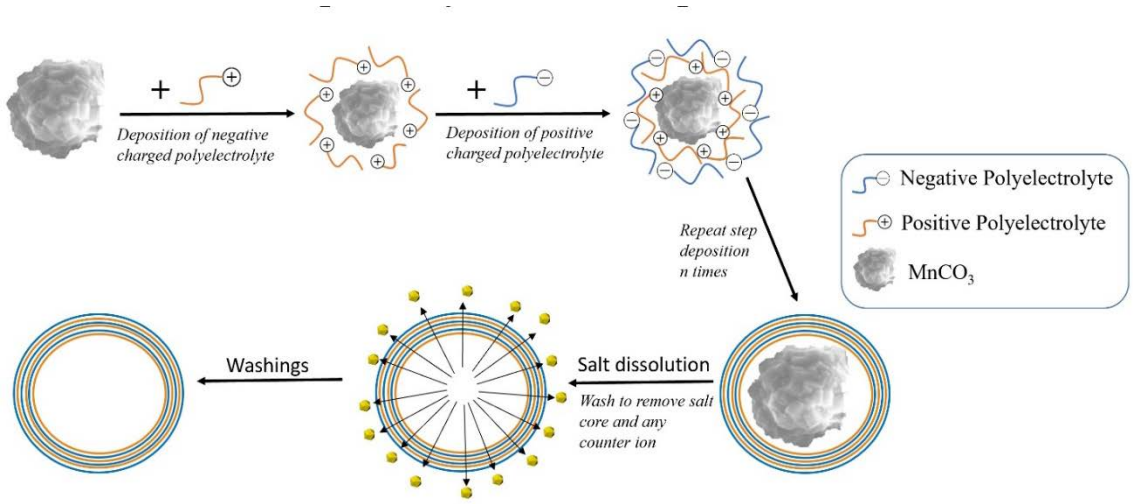

Figure 2.6. Procedure for the preparation of microcapsules of mixed polyphenols LS and TA using $MnCO_3$ particles as templates. Positive polyelectrolyte: PDDA or CH. Negative polyelectrolyte: LS and TA. The layer deposition was performed at pH 5.

As a general procedure, PDDA (0.5 mL, 1.0 mg/mL in sodium acetate buffer pH 5.0) was slowly added to a dispersion of $MnCO_3$ particles in MilliQ-grade water at pH 5 to build up the first layer. The coated particles were treated under similar conditions with LS (0.5 mL, 1.0 mg/mL in sodium acetate buffer pH 5.0). Then, PDDA and LS layers were continuously built up in the same way as above, to yield $(PDDA/LS)_n$, where "n" represents the number of the couple of the deposited layers. The scanning electron microscopy images (SEM) of $(PDDA/LS)_3$ **1** and $(PDDA/LS)_5$ **2**, are reported in Figure 2.7.

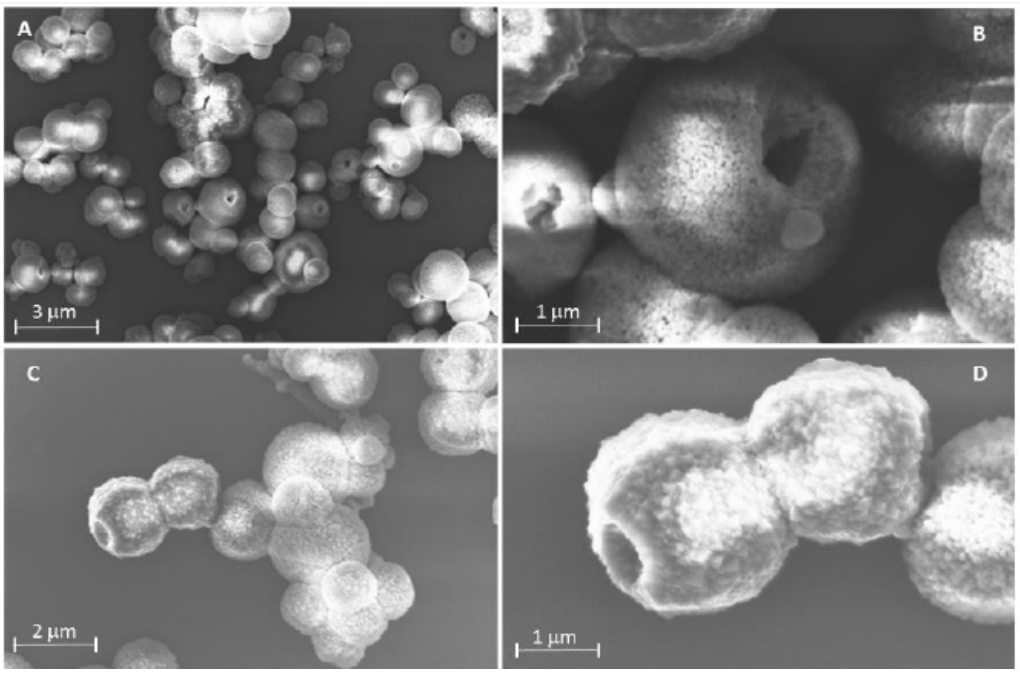

Figure 2.7. SEM image of (PDDA/LS)3 **1** (panels A and B) and (PDDA/LS)5 **2** (panels C and D).

The SEM image of $(PDDA/LS)_3$ **1** showed spheres of regular shape with an average diameter of 2.0±0.1 μm, some of which are characterized by an "open mouth" at the lateral side of the capsule, probably as a consequence of the rush out effect of the solvent in the interior of the sample during the drying conditions required for the microscopy analysis (Figure 2.7, panels A-B)[84]. Examples of "open mouth" have been previously reported in the case of LS capsules prepared by precipitation of lignin from THF[149]. At a larger magnification, the surface of the capsules appeared as a roughly aggregate of small clumps (Figure 2.7, panel B). This morphology was found to be changed by increasing the number of the layers, as for $(PDDA/LS)_5$ **2**, in which case the clumps are associated to each other to form large homogeneous zones with a regular bee nest-like structure (Figure 2.7, panels C-D). Next, chitosan (CH, 0.5 ml, 1.0 mg/ml in sodium acetate buffer pH 5.0) was used as natural alternative to PDDA for the preparation of $(CH/LS)_5$ **3**, due

to its high biodegradability and nontoxicity[150.] The SEM images of **3** showed microcapsules with an average diameter of the same order of magnitude than **2** (Figure Figure 2.8, panel A), characterized by an irregular surface. This morphology is different from that observed for microcapsules of CH alone, showing a homogeneous distribution of small globules (Figure 2.8, panel B).

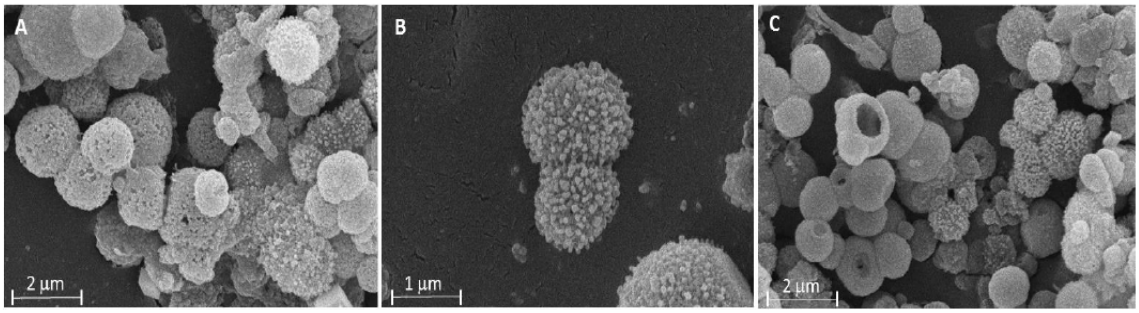

Figure 2.8. SEM image of (CH/LS)5 **3** (panel A and panel C). Panel B shows microcapsules of CH alone.

Again, an "open mouth" was observed in some of the detected capsules (Figure SI-3, panel C, left side). Microcapsules of TA alone, namely $(PDDA/TA)_5$ **4** and $(CH/TA)_5$ **5** (Figure 2.9, panels A-D), were prepared as references[151]. In this latter case, hydrogen bonding interactions were mostly responsible for the stability of the aggregate[152]. Microcapsules of **5** were spherically shaped with a regular distribution (Figure 2.9, panel B) and homogeneous surface morphology, probably due to the formation of stable hydrogen bonding networks between the TA and CH layers[153]. Fragmented particles of **5** showed the presence of sub-structure motifs inside the external shell (Figure 2.9, see arrow).

Finally, we focused our attention on the preparation of microcapsules of mixed polyphenols containing both LS and TA, using PDDA as the support layer. Microcapsules $(PDDA/TA/PDDA/LS)_5$ **6** (with LS as the external layer) showed two main morphologies (Figure 1, panel A). The prevalent motif was a regular spherical shape (Figure 2.10, panel B), besides to a scratched motif (Figure 2.10, panel C).

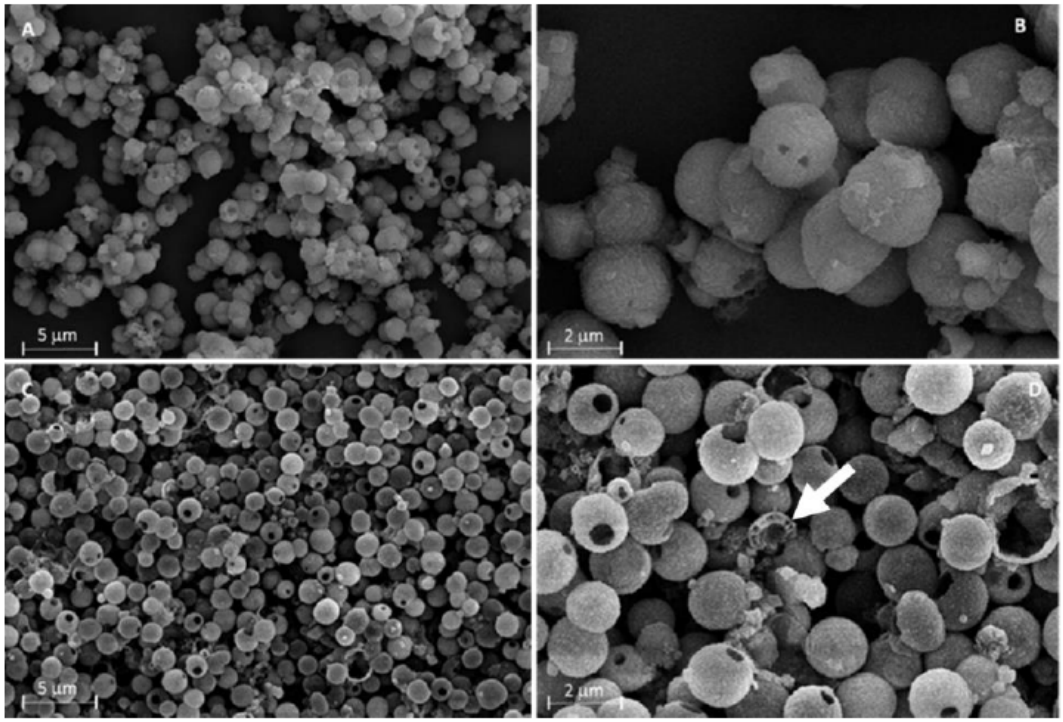

Figure 2.9. SEM image of (PDDA/TA)5 **4** (Panel A-B) and (CH/TA)5 **5** (Panel C-D).

Probably, the presence of the scratched motif might be due to incomplete deposition of the PDDA layer. The contemporary presence of LS and TA layers in **6** was confirmed by ^{31}P-NMR analysis (see next)[145].

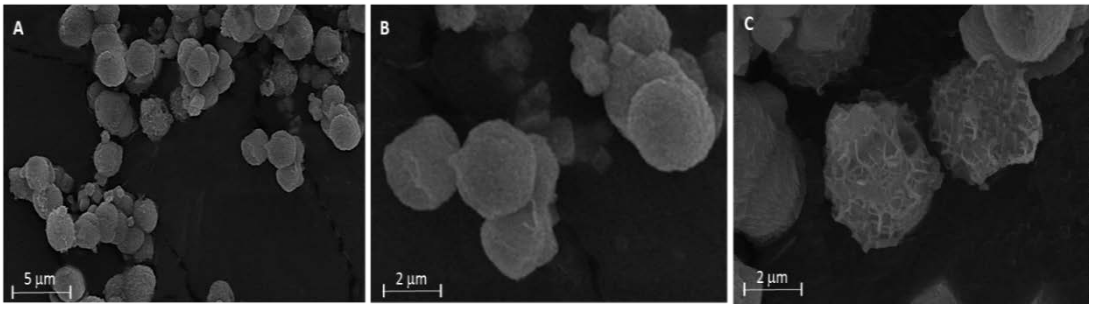

Figure 2.10. SEM images of (PDDA/TA/PDDA/LS)5 **6** at different magnification. Panel A: General particles view. Panel B: Detail of the predominant regular spherical shape motif. Panel C: Detail of the scratched surface motif.

Microcapsules (CH/TA/CH/LS)$_5$ **7**, bearing the CH layer instead of PDDA, were prepared in a similar way. The SEM analysis of **7** showed capsules with a regular spherical shape (Figure 2.10, panels A-B), characterized by well-defined networks (Figure 2.10, panel A, see arrow).

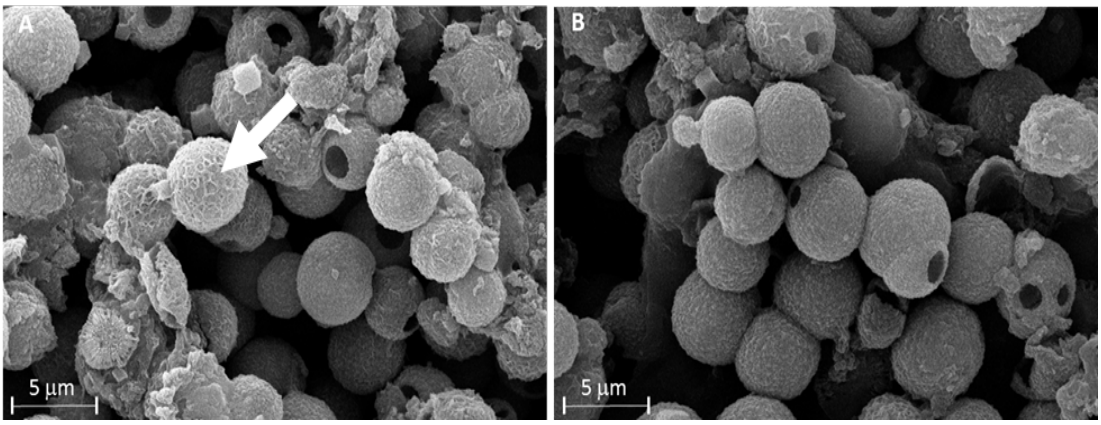

Figure 2.11. SEM images of $(CH/TA/CH/LS)_5$ **7** at different magnification.

Microcapsules containing the mixture of LS and TA (1:1 w/w ratio), namely $(PDDA/LS+TA)_5$ **8**, were also prepared as an alternative to the previously studied sequential deposition of the individual layers of the single polyphenols. In this latter case, spherical capsules formed large aggregates (Figure 2.12, panel A), with a pronounced film-like surface motif (Figure 2.12, panel B). These large aggregates were most probably produced as a consequence of the known coordination properties of the external layer of TA[154].

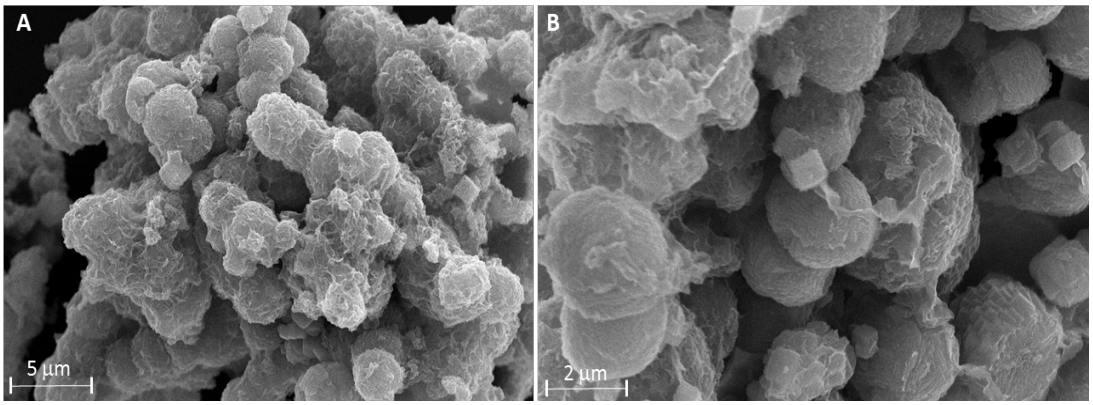

Figure 2.12. SEM images of (PDDA/LS+TA)5 **8** at different magnification. Panel A: large aggregates of partial fused spherical capsules. Panel B: magnification of the surface film-like motif.

Preparation of mixed LS and TA nanocapsules

The procedure for the preparation of nanocapsules of mixed polyphenols is reported in Figure 2.13 (Panels A-B). Nanoparticles of organosolv lignin (NOL) were used as a template instead of $MnCO_3$. We started with the deposition of CH as positive charged counterpart, since NOL are characterized by a negative surface charge[124].

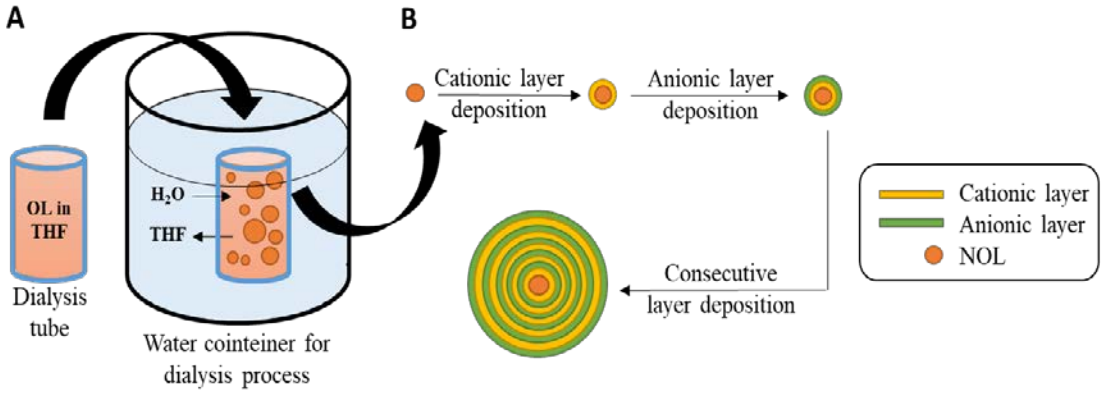

Figure 2.13. Preparation of mixed LS and TA nanocapsules. Panel A: Organosolv Lignin (OL) dissolved in THF was dialyzed against deionized water to yield NOL. Panel B: Preparation of NOL(CH/TA)5 **9**, NOL(CH/LS)5 **10** and NOL(CH/TA/CH/LS)5 **11**. Cationic layers: CH. Anionic layers: TA and LS.

Then, LS, CH and TA layers were continuously built up as previously described, to yield NOL(X/Y)$_n$, where "n" represents the number of couple of layers, while X and Y are the single polyphenol and polyelectrolyte components. SEM images of NOL(CH/TA)$_5$ **9**, NOL(CH/LS)$_5$ **10** are reported in supporting information (Figures SI-6 and Figure SI-7), that of NOL(CH/TA/CH/LS)$_5$ **11** in Figure 2.14. NOL(CH/TA)$_5$ **9** and NOL(CH/LS)$_5$ **10** showed capsules of regular spherical shape similar to that previously observed for **7**, the sample **10** being characterized by the highest size uniformity. A different morphology was observed in the case of the mixed polyphenol NOL(CH/TA/CH/LS)$_5$ **11** (Figure 2.14), which is characterized by a morphological structural motif similar to **7**, probably as a consequence of the presence of the same sequence of deposited layers (that is: TA, LS and CH).

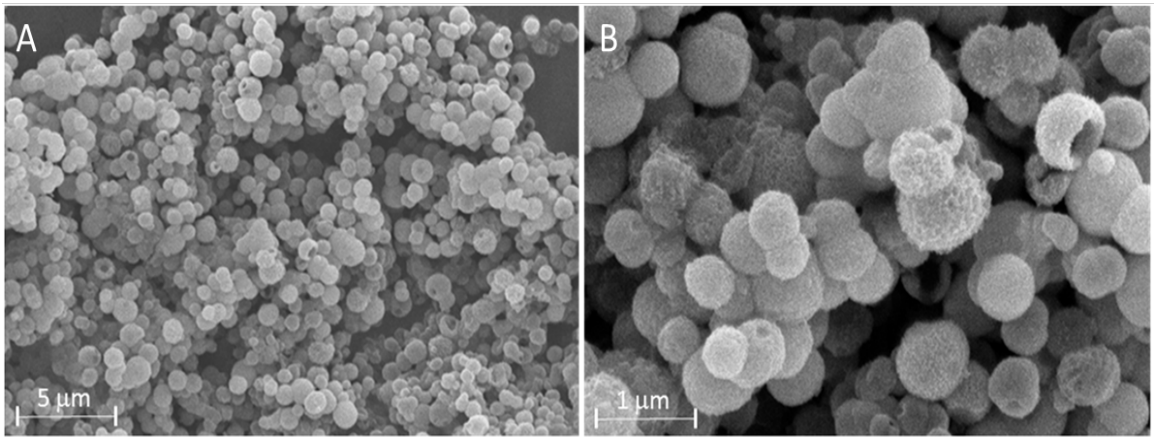

Figure 2.14. SEM images of NOL(CH/TA/CH/LS)5 **11** at different magnification. Quantitative 31P-NMR characterization of microcapsules and nanocapsules of mixed polyphenols.

In order to verify the contemporary presence of the different polyphenol layers, capsules (CH/TA/CH/LS)$_5$ **7** and NOL(CH/TA/CH/LS) **11** were characterized by ^{31}P-NMR spectroscopy. PDDA containing capsules, e.g. (PDDA/TA/PDDA/LS)$_5$ **6**, were not analyzed due to the lack of PDDA signals in ^{31}P NMR analysis. Briefly, the samples were dissolved in pyridine/$CDCl_3$ (300 µL; 1.6/1.0 v/v) under sonication conditions and phosphitylated in situ with 2-chloro-4,4,5,5- tetramethyl-1,3,2-dioxaphospholane. The ^{31}P-NMR analysis of native LS, OL, TA, and CH were also performed as references (Figure 2.15).

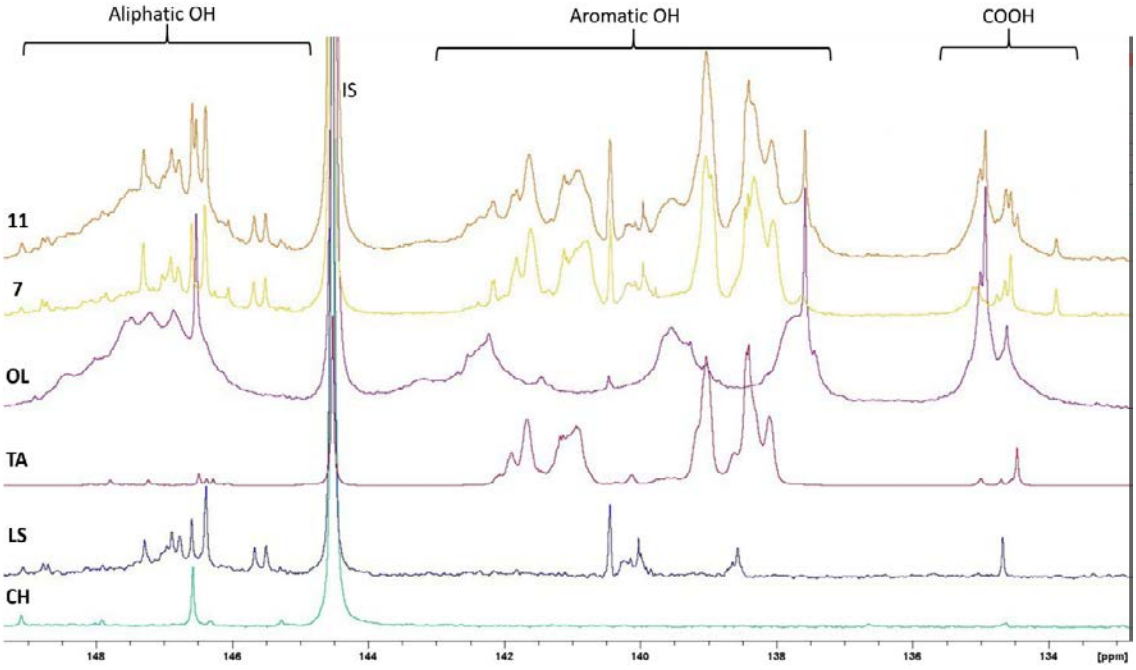

Figure 2.15. Quantitative 31P-NMR spectra and signal assignment of commercial CH, LS, OL and TA, and of capsules (CH/TA/CH/LS)5 **7** and NOL(CH/TA/CH/LS)5 **11** after dissolution in pyridine/CDCl3 (300 µL; 1.6/1.0 v/v) under sonication conditions and phosphitylation with 2-chloro-4,4,5,5-tetramethyl-1,3,2-dioxaphospholane. OL: Organosolv lignin; LS: Sulfonate lignin; TA: Tannic acid: CH: Chitosan. Typical lignin chemical shift (ppm): A) *para*-phenolic groups - 138.5-138.8 ppm; B) guaiacyl groups-138.7-140.1 ppm; C) condensed phenol groups-140.3-140.5 ppm; D) syringyl groups-142.0-144.0 ppm; E) aliphatic hydroxyl groups-146.0-149.0 ppm; F) carboxylic acids groups-134.0-135.5 ppm. Typical tannin chemical shift (ppm): A) *ortho*substituted phenol groups-138.0-138.7 ppm; B) catechol hydroxyl groups-138.8-139.4 ppm; C) *ortho*-disubstituted phenol groups (internal gallate units)-140.6-141.4 ppm; D) *ortho*-disubstituted phenol groups (external gallate units)-141.5-142.2 ppm.

LS, OL and TA showed characteristic ^{31}P-NMR signals in the range of 145-149 ppm, and 137- 142 ppm, respectively. These signals were also detected in the spectra of **7** and **11**. The spectrum of LS (Figure 2.15, blue-line) exhibited typical *para*-phenolic groups

at 138.5-138.8 ppm, followed by guaiacyl groups in the range of 138.7-140.1 ppm, and condensed phenol units at 140.3-140.5 ppm. In a similar way, the spectrum of OL (Figure 2.15, purple-line) exhibited the *para*-phenolic groups at 137.3-138.0 ppm, followed by the guaiacyl groups in the range of 139.5-140.1 ppm, and the syringyl groups at 142.0-144.0 ppm. Both lignin samples showed aliphatic hydroxyl groups in the range of 146.0-149.0 ppm, and carboxylic acids groups at 134.0-135.5 ppm. The spectrum of TA (Figure 2.15, red-line) showed a different pattern. In particular, the *ortho*-substituted phenol and the catechol hydroxyl groups were detected at 138.0-138.7 ppm, and 138.8-139.4 ppm, respectively, while the *ortho*-disubstituted phenols were found at 140.6-141.4 ppm (internal gallate units), and at 141.5-142.2 ppm (external gallate units), respectively. In this latter case a low contribute of the aliphatic hydroxyl peaks was observed. Finally, CH showed signals only in the range of aliphatic hydroxyl groups. The most representative signals expected for LS and OL, and for TA, were clearly identified in the ^{31}P-NMR spectra of **7** and **11**, confirming the presence of the wo polyphenols. Table 5 reports the quantitative distribution of the phenolic and alcoholic functional groups (millimoles/gram) in the samples for which the spectra are displayed in Figure 2.165.

Table 5. Functional group distribution (mmol/gram) for LS, OL, TA, (CH/TA/CH/LS)5 **7** and NOL(CH/TA/CH/LS)5 **11.**[a]

sample	carboxylic acids	aliphatic-OH	phenolic -OH				
			Ortho-disubstituted -OH	Ortho-substituted -OH	Syringyl -OH	Guaiacyl	p-hydroxyl phenyl
11	3.97	6.89	4.92	6.71	2.89	2.21	7.21
7	1.98	3.81	4.71	6.57	-	1.29	0.95
LS	1.12	2.79	-	-	-	1.31	0.98
TA	0.92	0.75	4.51	6.23	-	-	-
OL	2.01	3.96	-	-	2.91	0.81	6.11

[a]Quantitative ^{31}P-NMR spectra were performed after dissolution of the sample in pyridine/$CDCl_3$ (300 μL; 1.6/1.0 v/v) under sonication conditions and phosphitylation with 2-chloro-4,4,5,5-tetramethyl-1,3,2-dioxaphospholane. OL: Organosolv lignin; LS: Sulfonate lignin; TA: Tannic acid.

Antioxidant activity and UV-absorbing properties of microcapsules and nanocapsules of mixed Polyphenols

Lignin and tannic acid are characterized by radical scavenging activity due to the presence of free phenolic groups which are able to capture the radical species by formation of stable phenoxy radicals. The presence of ortho-substituents in the aromatic

ring, such as the methoxyl substituents of the guaiacyl and syringyl moieties, further increases the antioxidant activity by both steric hindering and resonance effects[41]. The antioxidant activity of selected microcapsules $(CH/LS)_5$ **3**, $(CH/TA/CH/LS)_5$ **7** and $(PDDA/LS+TA)_5$ **8**, and of nanocapsules $NOL(CH/LS)_5$ **10** and $NOL(CH/TA/CH/LS)_5$ **11**, was evaluated by the 2,2'-diphenyl picrylhydrazyl (DPPH) radical scavenging analysis. These microcapsules and nanocapsules have been selected in order to compare samples containing both polyphenols and having the same sequence in the layer composition. Moreover, sample **8** has been selected to evaluate the antioxidant effect of capsules containing both polyphenols in the same layer. Native LS and TA were also studied as references. The appropriate sample was suspended in EtOH and added to standard DPPH solution. DPPH is a table free radical, that is applied for the spectrophotometric evaluation of the radical scavenging ability of polyphenols. The decrease of DPPH absorbance (517 nm) was determined for each sample and the collected data were used to calculate the IC_{50} (defined as the μg/mL concentration of substrate that causes 50% loss of DPPH activity)[155]. Figure 2.6 reports the percentage of DPPH radical scavenging activity and the IC_{50} value for the analyzed samples. As a general trend, the nanocapsules **10**-**11** showed antioxidant activity higher than microcapsules **3** and **7**-**8**. Moreover, the antioxidant activity of nanocapsules **10**-**11** was higher than that of native LS and TA. The higher antioxidant activity of **11** with respect to **7** is in accordance with the total amount of aromatic phenolic groups as measured by ^{31}P-NMR analysis, that is 23.94 (mmol/gram) for **11 v**ersus 13.52 (mmol/gram) for **7**, respectively (Table 5, entries 1 and 2). Nanoscale lignin showed highest antioxidant activity when compared to micro-scale lignin, probably due to a combination between the highest surface-area-to-volume ratio and the emergence of specific π-π interactions[43]. As a general trend, the capsules of mixed polyphenols were the most active antioxidants, showing an IC_{50} value of the same order of magnitude than that of standard food antioxidants, such as BHT and ascorbate (IC_{50} c.a. 10 μg). Irrespective to the scale dimension, the presence of TA always enhanced the antioxidant activity, probably as a consequence of the higher amount of ortho-substituted and ortho-disubstituted phenol moieties, as detected by ^{31}P-NMR analysis (Table 5, entry 4).

The UV-absorbing ability of microcapsules $(CH/LS)_5$ **3**, $(CH/TA/CH/LS)_5$ **7** and $(PDDA/LS+TA)_5$ **8**, and of nanocapsules $NOL(CH/LS)_5$ **10** and $NOL(CH/TA/CH/LS)_5$ **11**, was determined by irradiation experiments in the energy range from 190 nm to 600 nm (from UV to visible regions) LS, TA and NOL were studied as references. As reported

in Figure 2.17, microcapsules **3** and **7-8** showed a similar absorbance ability in the UV-C and UV-B regions.

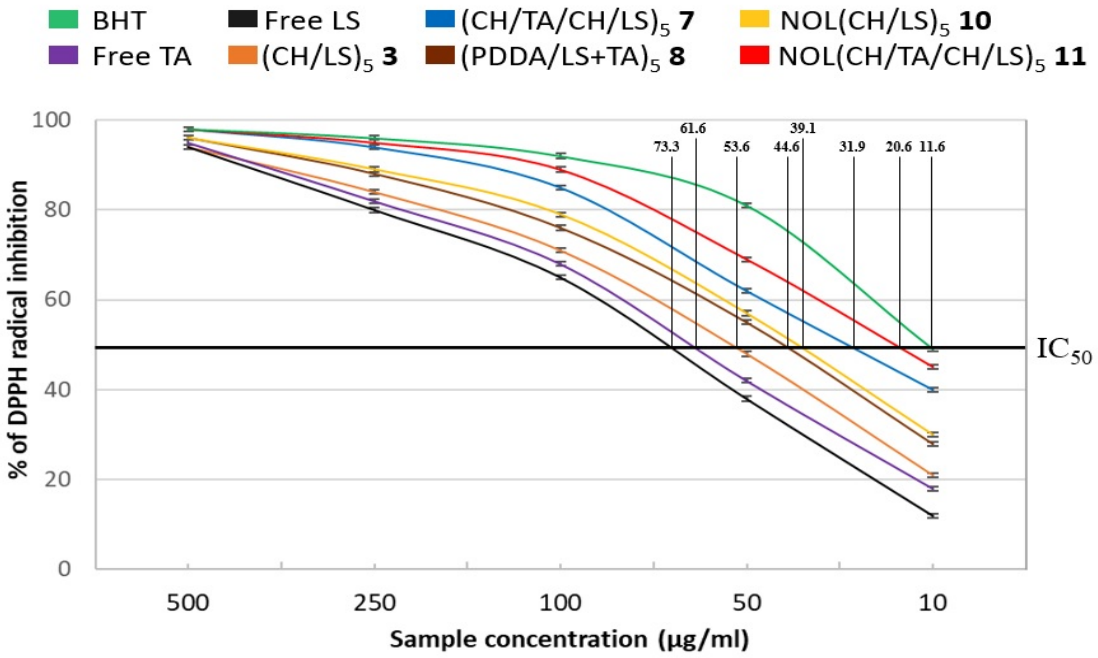

Figure 2.16. DPPH antioxidant scavenging activity of investigated microcapsules and nanocapsules presented as % of DPPH radicals inhibitions and IC50 values (µg/mL). Relative standard deviation was less than 3.0 %.

Note that microcapsules **3** and **7-8** were more active than native LS and TA. As a general trend, nanocapsules **10** and **11** were photoabsorbers more efficient than **3** and **7-8**, sample **11** being the most active system. Moreover, nanocapsules **10** and **11** were more efficient than NOL. This effect was particularly pronounced in the UV-B and UV-A regions. The high UV-A absorption property of **10** and **11** is noteworthy, since native LS and TA, and the corresponding microcapsules, showed only a low absorbance capacity in this UV-region. Moreover, a bathochromic shift of the absorption peak at 280 nm (accredited to guaiacyl units and/or to unconjugated phenolic groups)[156] was observed for both microcapsules and nanocapsules in the following order: **11**>**10**>**7**,**8**>**3**. Previous studies showed that the lignin macromolecule is organized as a flat and disk-like aggregate in solution45, stabilized by π–π interactions between the aromatic rings[157]. conferring an UV absorbing enhancement[158]. The bathochromic shift observed in microcapsules and nanocapsules has been related to formation of J-aggregates in which the orientation of the adjacent aromatic rings is parallel to the longitudinal direction of

the layer, following a head-to-tail like arrangement. A similar bathochromic shift was also observed in the case of nanocapsules produced from Kraft lignin. The appreciable UV absorbing enhancement suggested that nanocapsules have stronger π-π interactions than microcapsules, while the order of the bathochromic shift previously reported highlight that capsules containing mixed polyphenols were more aggregated than the homo-polymeric counterpart.

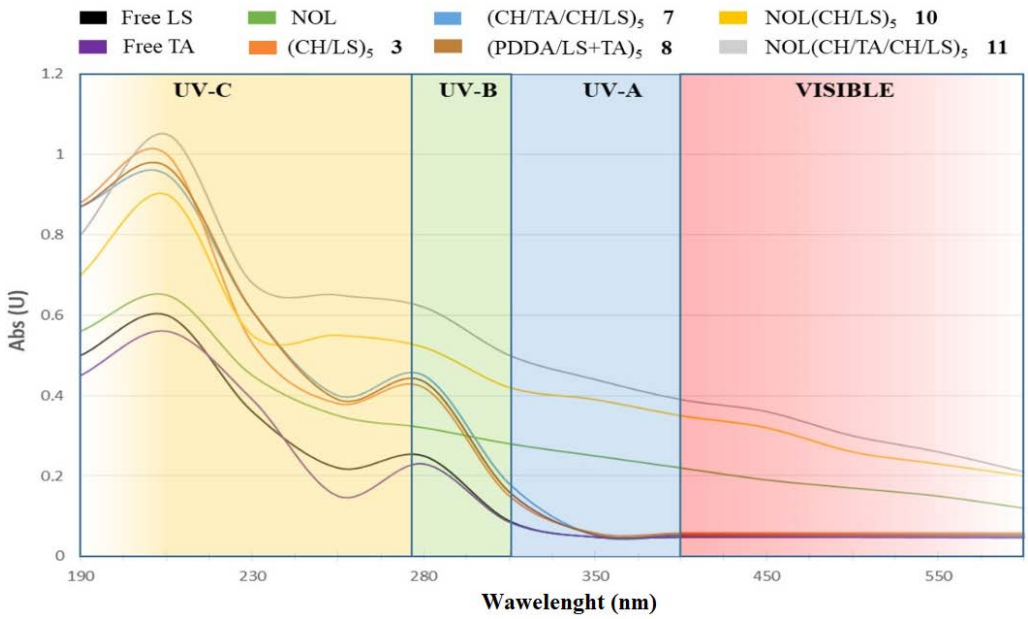

Figure 2.17. UV-Visible radiation absorbing capacity of investigated micro and nano-capsules.

Voltammetric and amperometric characterization of nanocapsules

Cyclic voltammograms (CVs) of NOL, NOL(CH/TA)$_5$ **9,** NOL(CH/LS)$_5$ **10**, and NOL(CH/TA/CH/LS)$_5$ **11** were performed, as selected examples, in the presence of ABTS (250 μM) in the Britton-Robinson buffer (pH 6.5, 120 mM) and KCl (100 mM) as supporting electrolyte (Figure 2.18). The CV at slow potential scan rate for the naked modified glassy carbon (GC) electrode (dotted black line) showed two stable and reversible redox couples, where the first anodic peak 0.5 V vs. SCE) is associated to the formation of the $ABTS^{+\bullet}$ radical cation, while the second peak (0.89 V vs. SCE) corresponds to the formation of the $ABTS^{2+}$bis-cation species. As reported in Figure 2.17, a remarkable increasing in the anodic peak current densities was observed in the presence of nanocapsules **9-11**, due to the reactions taking place between the two oxidized forms of ABTS and the lignin and tannic acid residues exposed on the surface of the nanocapsules[159]. In accordance with the DPPH antioxidant data previously reported, the

polyphenol mixed nanocapsules NOL(CH/TA/CH/LS)$_5$ **11** showed an inhibitory activity against the electrochemical induced oxidation of ABTS (purple line) higher than that of its homo-polymer counterparts, NOL(CH/TA)$_5$ **9** (blu line) and NOL(CH/LS)$_5$ **10** (red line), respectively. The samples **9** and **10** were more effective than NOL as reference, confirming the beneficial role of the sequential deposition of the TA and LS layers on the antioxidant activity. Moreover, **9** showed lower oxidation current densities with respect to **10**, probably due to the higher amount of ortho-substituted and ortho-disubstituted phenolic moieties in TA with respect to LS[160] (Table 5).

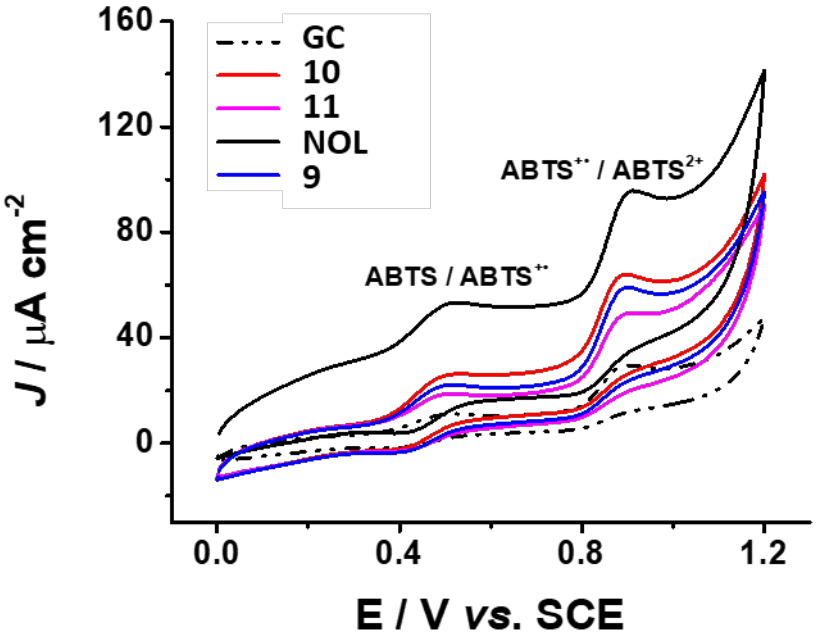

Figure 2.18. CVs performed with GCE (dash-dotted line), NOL (black line), NOL(CH/TA)5 **9** (bluline), NOL(CH/LS)5 **10** (red line), and NOL(CH/TA/CH/LS)5 **11** (purple line). Measurements were performed in 250 μM ABTS solution (120 mM Britton-Robinson buffer pH 6.5 containing 100 mM KCl as supporting electrolyte) at scan rate 20 mV s-1, T=25°C.

The effect of the pH on the antioxidant activity of nanocapsules **9-11** was successively evaluated by analyzing the variation of the formal potential (E_0') of the system depending on the specific pH range applied[49]. Cyclic voltammograms have been recorded at a scan rate of 50 mV s^{-1} under previously described experimental conditions. Nanocapsules retained their antioxidant activity in the pH range of 2.5-7.5 units, with the only exception of NOL(CH/TA)$_5$ **9**, which displayed the E_0' shifting versus pH only in the pH range of 4.5-7.5 units (Figure 2.19, panels A-D).

Generally, nanocapsules showed a similar pH dependence being all slopes very close to -60 mV/pH, which s the calculated slope for $2H^+/2e^-$ redox processes in the reduction of quinone to hydroquinone, according to the Nernst equation[161].

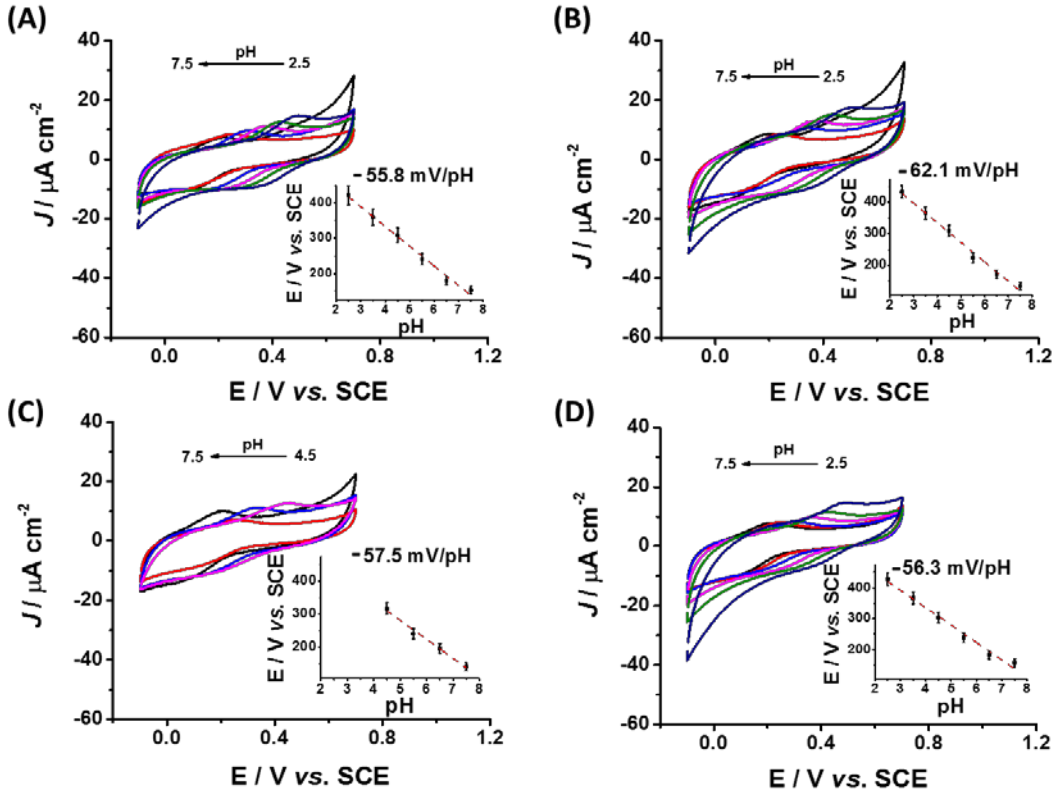

Figure 2.19. CVs of NOL (A), NOL(CH/TA)5 **9** (C), NOL(CH/LS)5 **10** (B), and NOL(CH/TA/CH/LS)5 **11** (D). CVs were recorded in 120 mM Britton-Robinson buffer containing 100 mM KCl as supporting electrolyte in the range 2.5-7.5. Insets: linear dependence of the formal potential (E0') versus pH.

Next, the $ABTS^{+\bullet}$ scavenging activity of nanocapsules **9-11** was measured in comparison with ascorbic acid (AA) by amperometry analysis[162]. Amperograms of nanocapsules **9-11** were recorded at the applied potential +0.55 V vs. SCE (required for the oxidation of $ABTS^{+\bullet}$), followed by the addition of several aliquots of ascorbic acid (30 µL of 1.0 mM AA solution). The progressive decolouration of $ABTS^{+\bullet}$ from blue-green to colourless was observed during the increase of the AA concentration. As a general trend, the oxidation current densities of $ABTS^{+\bullet}$ decreased by increasing the AA concentration, confirming the radical scavenging activity of nanocapsules (Figure 2.20, panel A). In accordance with the previously reported voltammetric data, polyphenol mixed nanocapsules **11** were more effective than the corresponding homo-polymer counterparts **9-10**, showing the highest slope values (Figure 10, panel B). Again, LbL nanocapsules **9-11** were more active than simple NOL.

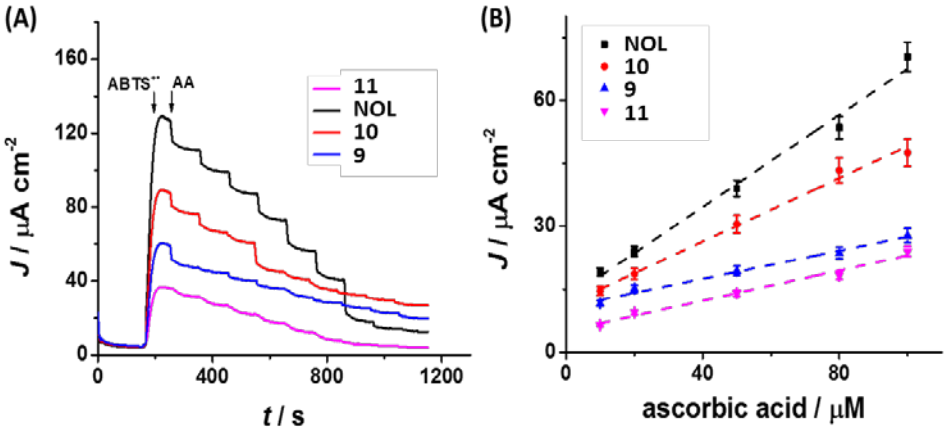

Figure 2.20. (A) Amperograms of NOL (black line), NOL(CH/TA)5 **9** (blu line), NOL(CH/LS)5 **10** (red line), and NOL(CH/TA/CH/LS)5 **11** (purple line). Measurements were performed in 120 mM Britton-Robinson buffer pH 6.5 containing 100 mM KCl as supporting electrolyte, adding 7 mM ABTS+• solution followed by several additions of AA. Experimental conditions: applied potential (Eapp): +0.55 V vs. SCE; stirring: 400 rpm ant T=25°C. **(B)** linear dependence of antioxidant activity on AA concentration.

2.3 Functionalized Tyrosinase-Lignin Nanoparticles as Sustainable Catalysts for the Oxidation of Phenols

2.3.1 Aim of work

The supramolecular interaction between lignin and proteins has been studied in details, identifying lignin-binding peptide sequences of affinity[112] and analyzing the role that conformational changes of the polymer played in the molecular recognition process [163].

The folding structure of the protein, associated to the prevalence of Coulombic forces in non-ionic medium with respect to hydrogen bonding and hydrophobic polar type interactions, emerged as crucial parameters in the self-assembly of proteins on the lignin surface[164]. Moreover, lignin showed high boosting activity towards copper oxidative enzymes, such as Lytic Polysaccharide MonoOxygenases (LPMOs), through long-range electron transfer mechanisms between the aromatic moieties and the metal atoms in the active site of the enzyme[165]. In this context, tyrosinase (EC 1.14.18.1) showed to further improve the LPMOs oriented boosting activity of lignin[166], performing the ortho-hydroxylation of phenol moieties to corresponding low redox-potential catechol derivatives (1, 2-benzene diols; monophenolase activity)[167]. Thus, lignin and tyrosinase cooperate in synergy to realize efficient oxidative processes. Tyrosinase has been widely studied because of its relevance in several applied areas[168], showing better performances in industrial applications when used in the immobilized form, as a consequence of its reusability, enhanced stability, and easier purification procedures[169].

In recent years, we described the preparation of heterogeneous catalysts for the synthesis of bioactive catechol derivatives by immobilization of tyrosinase on microcapsules of the epoxy resin Eupergit[170] and in alternative, by Layer-by-layer coating on Multi Walled Carbon Nanotubes (MWCNTS)[171]. These catalysts provided high catalytic efficiency in the synthesis of neuroactive 3,4-dihydroxyphenylalanine (DOPA)-containing peptides[172] and of lipophilic catechols with broad spectrum antiviral activity against both DNA and RNA viruses[173]. As a general trend, nanostructured catalysts showed greater activity, storage life, and reusability than the microcapsule counterparts[174]. This project describes the immobilization of tyrosinase from *Agaricus*

bisporus (T3824, multimeric enzyme with H2L2-type structure)[175] in nanoparticles of organosolv lignin (OL)[176] by four different procedures, namely: i) encapsulation, ii) surface adsorption, iii) Layer-by-layer (LbL) coating, and iv) LbL coating in the presence of bovine serum albumin (BSA) and glutaraldehyde (GA). At difference from native lignin and other technical lignins, OL has a relatively low molecular weight and a distinct solubility in organic solvents[177]. The novel catalysts have been characterized regarding to their structural and kinetic properties, and they have been successively applied for the oxidation of selected phenols to corresponding bioactive catechols.

2.3.2 Experimental

Materials

Organosolv lignin (OL) were purchased from Chemical Point. Mushroom tyrosinase, bovine serum albumin (BSA), glutaraldehyde (GA), poly(diallyldimethylammonium chloride) (PDDA, 20% v/v water solution), 2-chloro-4,4,5,5-tetramethyl-1,3,2-dioxaphopholane, chrome (III) acetylacetonate; deuterated chloroform ($CDCl_3$), ascorbic acid, Bradford reagent, *L*-tyrosine, *para*-cresol, tyrosol, 4-hydroxyphenylacetic acid, 3-(4-hydroxyphenyl)propionic acid, catechol, potassium chloride (KCl) and organic solvents were purchased from Sigma–Aldrich and were used without any further purification. All experiments were done in triplicate using native and immobilized tyrosinase in Phosphate buffer saline (PBS).

Reactivity of tyrosinase with organosolv lignin

An appropriate amount of OL (70 mg) was treated with tyrosinase (1000 U) in PBS (5.0 mL, 0.1 M; pH 7) under dioxygen atmosphere at room temperature for 24 h. This mixture was acidified (pH 3, 1.0 M HCl) and successively centrifuged (6000 rpm, 20 min) to remove the supernatant. The residue was rinsed with deionized water and then freeze-dried. The qualitative and quantitative analysis of alcoholic, acidic, and phenolic OH groups in the residual crude after tyrosinase treatment was determined by quantitative ^{31}P-NMR analysis[145]. Typically, the lignin sample (10 mg) was dissolved in pyridine/$CDCl_3$ (300 μL; 1.6/1.0 v/v), followed by addition of chrome (III) acetylacetonate solution (50 mL, 11.4 mg/ml) as relaxing agent. Then, the phosphitylation reagent 2-chloro-4,4,5,5-tetramethyl-1,3,2-dioxaphopholane (200 μl) was added under

magnetic stirrer and gentle heating at 45 °C for 2 h. NMR analysis was performed in the presence of cholesterol as an internal standard on a Bruker 400MHz apparatus. Gel Permeation Chromatography (GPC) analysis of OL was carried out following the procedure of acetobromination[178]. Briefly, an appropriate amount of lignin sample (10 mg) was suspended in acetic glacial/acetyl bromide mixture (2.5 mL of 92:8 v/v) and stirred at room temperature. After 2 h the solvent was evaporated under vacuum and the residue was dissolved in THF (5 ml). The GPC analysis were performed using a Shimadzu LC 20AT liquid chromatograph with a SPD M2OA ultraviolet diode array (UV) detector at 280 nm.

*Preparation of catalyst **I***

The preparation of catalyst **I** required the encapsulation of tyrosinase within the OL nanoparticles. Briefly, an appropriate amount of tyrosinase (3.0 mg, 900 U/mg) was added to a solution of OL in THF (2.0 mg/mL, 7.5 mL) previously filtered by 0.45 μm filter membrane. The solution obtained was dialyzed against deionized MilliQ water (500 mL) for 24 h at 25°C under slow magnetic stirring, using Spectrapore™ dialysis membrane (3,5 kD MWCO). Catalyst **I** was recovered by centrifugation (20 min at 6000 rpm) and the surnatant was used for the calculation of the activity parameters. The catalyst was washed several times with PBS in order to ensure the complete removal of unbounded tyrosinase (as evaluated by the Bradford method).

*Preparation of catalyst **II***

Catalyst **II** was prepared by direct adsorption of tyrosinase on preformed OL nanoparticles prepared by the dialysis protocol [11]. Briefly, OL solution (THF, 2 mg/mL) previously filtered by 0.45 μm filter membrane, was dialyzed against deionized water for 24h at 25°C with slow magnetic stirring, using Spectrapore™ dialysis membrane (3,5 kD MWCO). Finally, the OL nanoparticles obtained were centrifuged (20 min at 6000 rpm), washed with Milli-Q water and lyophilized. The appropriate amount of tyrosinase (3.0 mg, 900 U/mg), dissolved in sodium phosphate buffer PBS (3.0 mL, 0.1 M; pH 7), was added to a suspension of OL nanoparticles (15 mg) in PBS (15 mL) under orbital shaking at room temperature for 24 h. Catalyst **II** was recovered by centrifugation (20 min at 6000 rpm) and the surnatant was used for the calculation of

activity parameters. The catalyst was washed several times with PBS in order to ensure the complete removal of unbounded tyrosinase (as evaluated by the Bradford method).

*Preparation of catalyst **III***

The OL nanoparticles were coated with PDDA applying the LbL procedure[179]. Briefly, a suspension (15 mL) of OL nanocapsules in MilliQ water (1mg/mL, pH 4.2) was added dropwise to PDDA solution (1mg/mL, Milli-Q water) under slow magnetic stirring. After 2 h, the final suspension was centrifuged in order to recover OL-PDDA nanoparticles followed by washing with Milli-Q water and lyophilization. Tyrosinase (3.0 mg, 900 U/mg) was added to a suspension of OL-PDDA nanoparticles (15 mg) in PBS (15 mL) under orbital shaking at room temperature for 24 h. Catalyst **III** was recovered by centrifugation (20 min at 6000 rpm) and the surnatant was used for the calculation of the activity parameters. The catalyst was washed several times with PBS in order to ensure the complete removal of unbounded tyrosinase (as evaluated by the Bradford method).

*Preparation of catalyst **IV***

The OL-PDDA nanoparticles were prepared as described above and then used in order to immobilize BSA and tyrosinase by crosslinking with GA. Briefly, tyrosinase (300 μL, 3.4 mg/ mL in PBS) and BSA (1.5 ml, 2.0 mg/mL) were added to OL-PDDA nanoparticles suspension (3.5 mg ml^{-1}, PBS 1.4 ml), and the mixture was shaken for 30 min at room temperature. Finally, GA (150 μl, 2.5% v/v water solution) was added and the mixture was shaken again at room temperature for 30 min and then at 4 °C overnight. Catalyst **IV** was recovered by centrifugation (20 min at 6000 rpm) and the surnatant was used for the calculation of activity parameters. The catalyst was washed several times with PBS in order to ensure the complete removal of unbounded tyrosinase (as evaluated by the Bradford method).

SEM caracterization

For Scanning Electron Microscopy (SEM), catalysts (**I-IV**), were fixed with 3% glutaraldehyde in 0.1 M cacodylate buffer (pH 7.2), washed and post-fixed in OsO_4 (1.0% in weight) in the same buffer at room temperature. The samples were dehydrated in a graded ethanol series before the analysis. They were then air dried and sputter-coated with gold in a Balzers MED 010 unit. The observation was made by a JEOL JSM 6010LA electron microscope.

DLS and Zeta potential

Measurements of particle size and Zeta potential were performed on freshly prepared aqueous suspensions (pH = 7) of OL nanoparticles and Catalyst **I-IV** dispersed in water were performed before and by dynamic light scattering (DLS) using using a Zetasizer Nano ZS (Malvern Instruments, Malvern, UK) equipped with a He-Ne laser (633 nm, fixed scattering angle of 173°, 25°C). Prior to perform size measurements, suspensions were filtered with a 0.45-mm filter membrane. Measurements were performed at least in triplicate at room temperature (T=25°C).

Determination of the catalyst activity

The catalyst activity of the native and immobilized enzyme was determined by measuring the tyrosinase-catalyzed oxidation of L-tyrosine. The reaction was started by adding the substrate to the solution containing the appropriate amounts of the native enzyme, and in alternative, of catalysts **I−IV** in PBS under magnetic stirring. The initial rates were measured as the linear increase of the optical density at 475 nm, due to dopachrome formation. One unit of enzyme activity was defined as the increase in absorbance of 0.001 unit per minute at pH 7 and 25 °C, measured in a 3.0 mL reaction cuvette containing 0.83 mM of *L*-tyrosine and 67 mM PBS (pH 7.0). Spectrophotometric data were analyzed with Cary WinUV. All experiments were conducted in triplicate using free and immobilized tyrosinase.

Determination of the kinetic constants

Kinetic parameters, K_m, V_{max} and V_{max}/K_m, were determined spectrophotometrically by measuring the enzyme activity at different concentrations of *L*-Tyrosine (0.33–0.10 mM) and by plotting data in Lineweaver−Burk. All experiments were conducted in triplicate using native and immobilized tyrosinase. Reactions were carried out by means of the same procedure as for activity assay and measuring absorbance at 475 nm as described above.

Electrochemical characterization

Cyclic voltammetry experiments were performed by using a PGSAT204N potentiostat (Eco Chemie, The Netherlands) controlled by Nova 2.1 software (Eco Chemie, The Netherlands) with a conventional three-electrodes electrochemical cell equipped with a modified glassy carbon (GC) electrode as working electrode (d=3 mm, Cat. 6.1204.300,

Metrohm, Herisau, Switzerland), a saturated calomel electrode (SCE, 244 mV vs. NHE, Cat. 303/SCG/12, AMEL, Milano, Italy) and a glassy carbon rod electrode (d = 2 mm, Cat. 6.1241.020, Metrohm, Herisau, Switzerland), as reference and counter electrodes, respectively. All electrochemical measurements were performed in 50 mM PBS buffer pH 6.5 plus 100 mM KCl containing 250 µM cathecol, used as electrochemical mediator. GC electrodes (d=3 mm, Cat. 6.1204.300, Metrohm, Herisau, Switzerland) were polished with alumina slurries (Al_2O_3, particle size of 0.3 and 0.05 µm) on cloth pads wet with Milli-Q water (SIEM, Bologna, Italy), thoroughly rinsed with Milli-Q water and further sonicated for 5 min between each polishing step. For the bio-modification, GC electrodes were modified by drop-casting 5 µL of sample OL nanoparticles (2 mg/mL), catalyst **I** (2 mg/mL), catalyst **II** (2 mg/mL), catalyst **III** (2 mg/mL), and catalyst **IV** (2 mg/mL), respectively. For each different modification, three replicates have been performed.

General procedure for the oxidation of phenols

As a general procedure, phenols **1-4** (0.02 mmol), tyrosinase (540 IU) and ascorbic acid (2 eq) were placed in PBS 5.0 mL (0.1 M; pH 7) at 25°C for 24 h, and the mixture was stirred under O_2 atmosphere. Oxidations were performed using homogeneous and heterogeneous conditions. The reactions were monitored by thin layer chromatography (TLC, n-hexane/EtOAc=2.0:1.0). After the disappearance of the substrate, the reaction mixture was acidified with a solution of HCl 2.0 M and extracted twice with EtOAc. The organic extracts were treated with a saturated solution of NaCl and dried over anhydrous Na_2SO_4, then filtered and concentrated under vacuum. In the case of immobilized enzyme, catalysts **I-IV** were recovered by centrifugation (6000 rpm) for 20 minutes and the solution was subjected to the same work up as described above. The residue was treated with pyridine, HMDS and TMCS (HMDS–TMCS, 2:1 v/v) under vigorous stirring at room temperature for 2 h. Products were identified by gas-chromatography associated to mass-spectrometry analysis (GC–MS). The analyses were performed by 450 GC-320 MS apparatus using a VF-5MS column and an isothermal temperature profile of 100 °C for 2 min, followed by a 10 °C/min temperature gradient to 280 °C for 25 min. The injector temperature was 280 °C. Chromatography-grade helium was used as the carrier gas with a flow of 2.7 mL/min. Mass spectra were recorded with an electron beam of 70 eV.

2.3.3 Results and discussion

Reactivity of tyrosinase towards organosolv lignin (OL)

The reactivity of tyrosinase towards lignin is debated. Lignans, the secondary metabolites resembling the dimeric units of lignin, generally showed inhibitory activity against tyrosinase[180], and the catalytic effect of tyrosinase in the oxidation of milled wood lignin was found to be negligible with respect to that of laccase and horseradish peroxidase[181]. On the other hand, tyrosinase from *Agaricus bisporus* was reported to cleave the 4-*O*-5 and Cα-Cβ bonds of some representative dimeric lignin model compounds (4-phenoxylphenol and guaiacyl glycerol-β-guaiacylether)[182]. For this reason, we decided to study the reactivity of tyrosinase from *Agaricus bisporus* towards organosolv lignin (OL) before the immobilization procedures. OL (70 mg) was treated with tyrosinase (1000 U) in phosphate buffer (5.0 mL, 0.1 M; pH 7) under dioxygen atmosphere at room temperature.

After 24 h, the mixture was acidified (pH 3, 1.0 M HCl) and successively centrifuged (6000 rpm, 20 min) to remove the supernatant. The residue was washed with deionized water and freeze-dried to yield OL-tyr. A sample of OL, treated under similar experimental conditions in the absence of tyrosinase, was used as reference. The amount of characteristic OH groups in OL-tyr and OL samples was determined by quantitative ^{31}P NMR. Briefly, the samples were dissolved in pyridine/$CDCl_3$ (300 μL; 1.6/1.0 v/v) under sonication conditions and phosphitylated in situ with 2-chloro-4,4,5,5-tetramethyl-1,3,2-dioxaphopholane. Table 6 shows the relevant experimental data collected. More specifically, aliphatic, condensed, guaiacylic, para-hydroxy phenyl, and acidic lignin OH groups were measured. Data are averages of three phosphitylation experiments. The ^{31}P-NMR data showed a modest decrease of the total phenolic OH and of the total OH groups after the enzyme treatment (11% and 9%, respectively), confirming the low reactivity of tyrosinase towards lignin.

Table 6. Functional OH distribution (mmol/gram) for parent OL and for OL-tyr after treatment with tyrosinase.[a]

Sample	Carboxylic acid	Aliphatic -OH	Condesed -OH	Para-hydroxy Phenyl -OH	Guaiacyl -OH	Total phenolic -OH	Total group -OH
OL	0.22	0.99	1.95	0.24	0.68	2.87	4.08
OL-tyr	0.19	0.97	1.79	0.17	0.59	2.55	3.71

[a]Quantitative ^{31}P-NMR spectra were performed after dissolution of the sample in pyridine/$CDCl_3$ (300 μL; 1.6/1.0 v/v) under sonication conditions and phosphitylation with 2-chloro-4,4,5,5-tetramethyl-1,3,2-dioxaphopholane. OL: original sample of organosolv lignin; OL-tyr: organosolv lignin after treatment with tyrosinase. [b]Maximum standard deviation: 2 x 10^{-2} mmol/gram. Maximum error: 1x10^{-2} mmol/gram.

Structural modifications in OL-tyr were further evaluated by Gel Permeation Chromatography analysis (GPC) of the residue. In Table 7 are reported the weight average molecular weight (M_w), the number average molecular weight (M_n) and the polydispersity (M_w/M_n) of OL-tyr compared to parent OL. Tyrosinase treatment induced an appreciable increase in the M_w and M_n values.

Table 7. M_w, M_n and M_w/M_n of OL tyr compared with the parent OL.

Sample	**M_w**	**M_n**	**M_w/M_n**
OL	154.670[a]	15.104	10.2
OL-tyr	202.828	18.803	18.8

[a]Analyses were repeated in triplicate.

Thus, in our hand tyrosinase showed a low reactivity towards OL, affording a modest decrease of the total amount of phenolic OH, associated with a modest, although if significant, increasing in the weight average molecular weight of the polymer, probably as a consequence of oxidative coupling processes[183].

Encapsulation and direct adsorption procedures

Alkali Lignin nanoparticles have been previously reported as containers for drug delivery systems[184]. The encapsulation procedure consisted in the formation of nanoparticles by slow solvent exchange in the presence of the bioactive principle to be immobilized, such as resveratrol, sorafenib, benzazulene and ibuprofen[98]. Lignin nanoparticles showed high antioxidant protective effect, successfully releasing the bioactive principle in the cell. A similar procedure was applied in the encapsulation of dyes[185]. We decided to apply this procedure for the encapsulation of tyrosinase in OL nanoparticles. Tyrosinase (3.0 mg, 900 U/mg) was added to a solution of OL in THF (2.0 mg/mL, 7.5 mL) at room temperature, and the solution was dialyzed against MilliQ water (500 mL) for 24 h. During the slow exchange of the solvent, the lignin molecules

interacted together to close the nanoparticles, tyrosinase being entrapped inside their empty core cavity. At the end, the encapsulated tyrosinase system (catalyst **I**) was recovered by centrifugation and washed to remove the excess of the enzyme (Scheme 2.21, pathway A). Scanning electron microscopy (SEM) images of catalyst **I** are reported in Figure 2.21.

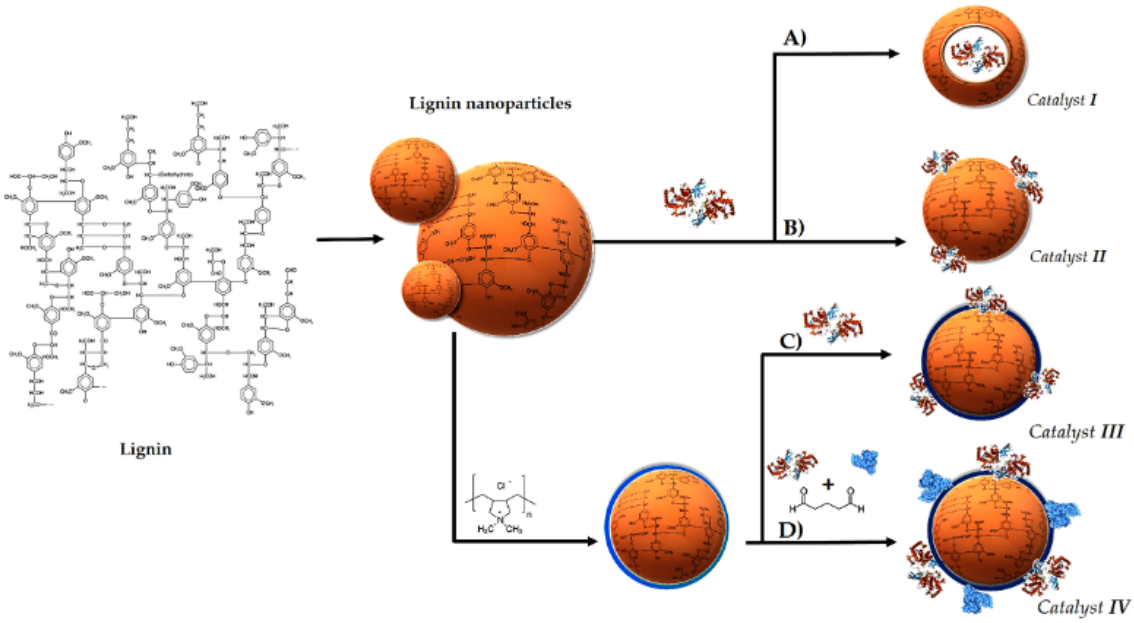

Figure 2.21. Schematic representation for the preparation of catalysts **I-IV**.

The SEM image of catalyst **I** showed spheres of regular shape (Figure 2.22, panel A) with an average diameter of 0.19±0.01 μm, as evaluated by Dinamic Light Scattering (DLS) analysis (Figure 2.23).

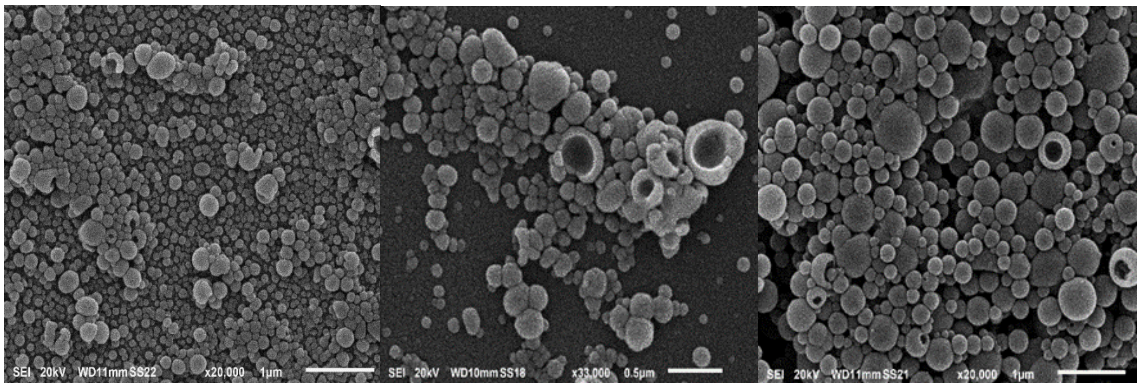

(a) (b) (c)

Figure 2.22. SEM images of catalyst **I** and catalyst **II**. (**a**) General overview of catalyst **I**; (**b**) Selected magnification of catalyst **I;** (**c**) General overview of catalyst **II.**

Fragmented particles were characterized by the presence of empty cavity (Figure 2.22, panel B). The presence of the enzyme in catalyst **I** was observed by confocal analysis using a tyrosinase previously marked with Fluorescein isothiocyanate (FITC)[186]. As reported in (Figure 2.24, panel A), catalyst **I** showed the expected green fluorescence signal inside nanoparticles. The entrapment of tyrosinase was further confirmed measuring the value of the Zeta potential of the particle surface, that was found to be very similar to the value obtained for the parent OL nanoparticles (Figure 2.25).

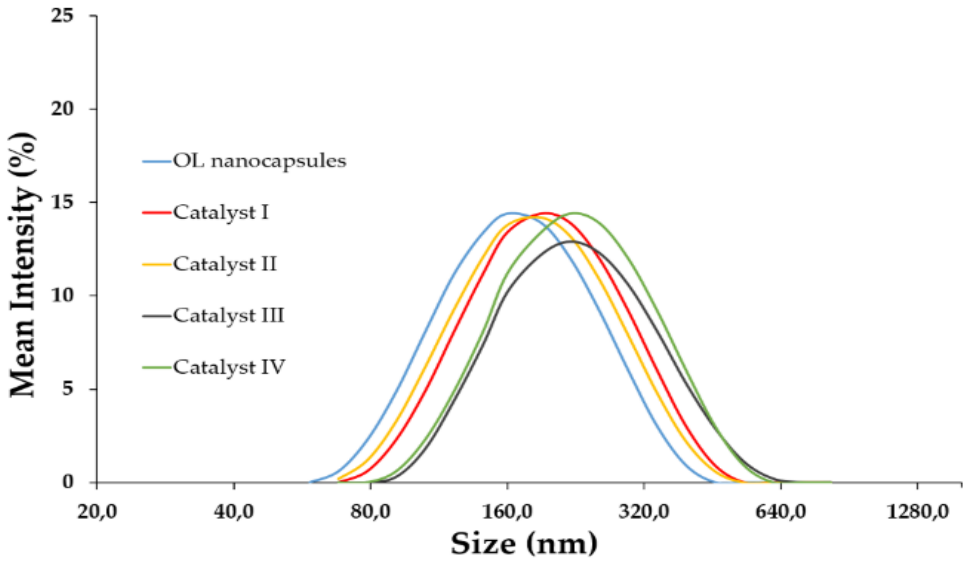

Figure 2.23. Particle diameter distributions of OL nanocapsules and Catalyst **I-IV**

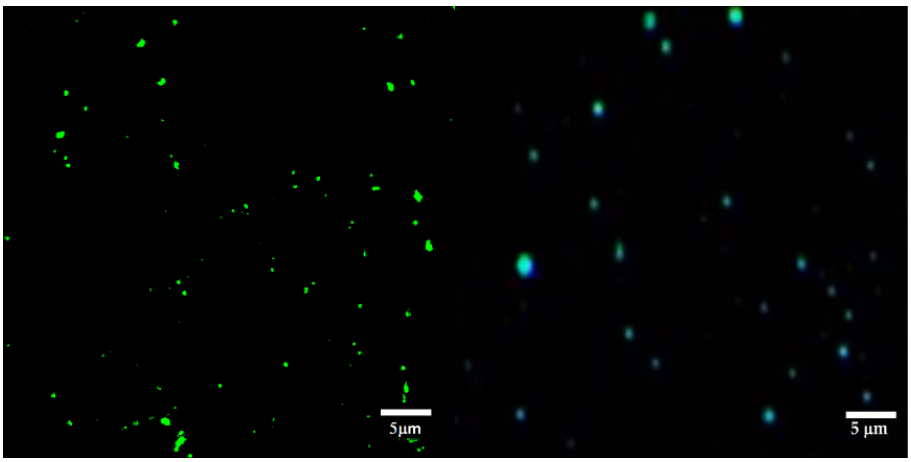

Figure 2.24. Confocal images of (**a**) Catalyst **I**; (**b**) Catalyst **II**.

As an alternative, catalyst **II** was prepared by direct adsorption of tyrosinase on preformed OL nanoparticles (Scheme 2.21, pathway B). Briefly, tyrosinase (3 mg, 900 U/mg) dissolved in sodium phosphate buffer PBS (3.0 mL, 0.1 M; pH 7) was added to a

suspension of OL nanoparticles (15 mg) in PBS (15 mL) under orbital shaking at room temperature overnight. Catalyst **II** was recovered after centrifugation and rinsed with PBS to remove the excess of the enzyme. (Figure 2.21, panel C) reports the SEM image of particles of catalyst **II,** characterized by an average diameter of 0.20±0.01 μm (Figure 2.23). The confocal image of catalyst **II** (Figure 2.24, panel B), performed in the presence of the marked enzyme, showed a relatively weak green fluorescence signal only on the surface of nanoparticles (the background azure emission of the core being associated to the known auto-fluorescence of lignin[187]. Moreover, the Zeta potential of catalyst **II** varied with respect to parent OL nanoparticles (Figure 2.25). These data confirmed that the adsorption of tyrosinase was limited to the surface of the nanoparticles.

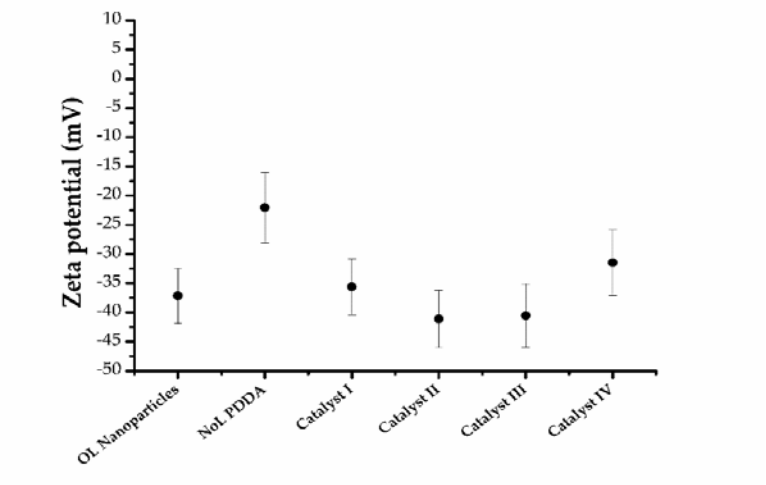

Figure 2.25. Zeta potential values of OL nanoparticles, OL PDDA nanoparticles and catalysts **I-IV.**

Layer-by-layer immobilization procedure

The LbL procedure, based on the consecutive deposition of alternatively charged polyelectrolytes onto an appropriate support, protects enzymes from denaturing agents and allows regulation of the permeability towards small substrates, which can cross the multilayer and react with the catalytic site[188]. The use of the LBL procedure for the immobilization of tyrosinase from *Agaricus bisporus* on Multiwalled Carbon Nanotubes (MWCNTs) has been previously reported to increase the activity of the enzyme. Since lignin nanoparticles are characterized by a negative value of the Zeta potential (-42 mV at pH 4.2), we started by the deposition of a first positive charged layer of polydiallyldimethylammonium chloride (PDDA), able to efficiently interact with the lignin surface by cation-π interactions[188]. Briefly, a suspension (15 mL) of OL nanoparticles in MilliQ water (1.0 mg/ml, pH 4.2) was added dropwise to PDDA solution

(1.0 mg/mL, Milli-Q water) under slow magnetic stirring for 2 h. The deposition of the PDDA layer was monitored by UV-visible analysis, following the appearance of typical peak at 276 nm, which corresponds to the shift of the characteristic PDDA B-band after adsorption on lignin. This result was further confirmed by the Zeta potential analysis (Figure 2.25), the system reaching the value of -22 mV. Tyrosinase (3 mg, 900 U/mg) was then added to OL/PDDA nanoparticles (PBS; 3mL) to yield catalyst **III** (Figure 2.20, pathway C). Scanning electron microscopy (SEM) image of catalyst **III** (Figure 2.26, panel A) showed regular spherical particles with a wrinkled surface and an average diameter of 0.22±0.02 μm. Catalyst **III** showed a Zeta potential value of -40 mV (Figure 2.25).

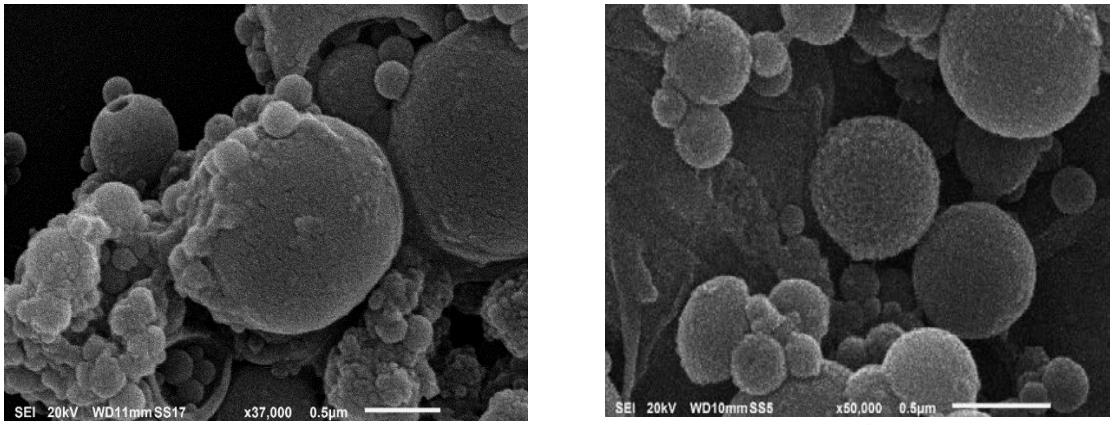

(**a**) (**b**)

Figure 2.26. SEM images of catalyst **III** in the first panel (**a**) and of catalyst **IV** in the second panel (**b**).

Finally, we applied the glutaraldehyde (GA)-assisted co-immobilization of tyrosinase in the presence of Bovine Serum Albumin (BSA)[189]. As a general trend, the immobilization efficiency of tyrosinase is dependent upon the number of the enzyme molecules loaded on the selected surface. The enzyme strives for the greatest surface coverage, leading to conformational changes that could influence the activity. BSA performs as an inert protein with an isoelectric point close to that of tyrosinase, to partially reduce the amount of surface area available for the enzyme, while GA forms a protective three-dimensional network[190]. Briefly, the suspension of OL/PDDA nanoparticles (3.5 mg/mL) in PBS (1.4 mL) was added to tyrosinase (300 μL, 3.4 mg/mL in PBS) and BSA (1.5 ml, 2.0 mg/mL) under gentle shaken for 30 min at room temperature. Finally, GA (2.5% v/v water solution) was added to yield catalyst **IV** (Figure 2.21, pathway D). Figure 2.26 (panel B) reports the SEM image of catalyst **IV**. The surface of catalyst **IV** appeared

as a roughly aggregate of small clumps with an average diameter of 0.22±0.02 μm (Figure 2.22) and a value of the Zeta potential of -32 mV, that is significantly different from that previously measured for catalyst **III**.

*Activity parameters of catalysts **I-IV***

The Tyrosinase (Tyr) activity was determined by the dopachrome assay[191] following the oxidation of L-tyrosine at 475 nm, the enzyme unit being defined in terms of the increase in absorbance of 10^{-3} unit/min at 25 °C in 0.1M phosphate buffer (pH 7.0). The immobilization and activity yields were evaluated as reported in equations 1 and 2, respectively:

$$\text{Activity (units/mg)} = Ux/Wsupport \quad (1)$$

$$\text{Activity yield (\%)} = [Ux/(Ua - Ur)] \times 100 \quad (2)$$

$$\text{Immobilization yield (\%)} = [(Ua - Ur)/Ua] \times 100 \quad (3)$$

Where Ua is the total activity (units) of the enzyme added to the solution and Ur is the residual activity (units) evaluated by the dopachrome method in the washing solutions.

As reported in Table 8, catalysts **III**-**IV** showed a value of the immobilization yield higher than that of catalysts **I**-**II**, suggesting a better performance of the LbL procedure in the immobilization of tyrosinase with respect to encapsulation and direct adsorption processes (entries 3-4 versus entries 1-2). The activity yield followed a similar trend. Note that catalyst **IV** was characterized by the highest value of the activity yield confirming the beneficial role of BSA and GA in the retention of the tyrosinase catalytic performance after the immobilization process. The activity of catalyst **II-IV** was comparable to that previously reported tyrosinase based nanocatalysts[171].

Table 8. Activity parameters of catalysts **I-IV.**

Entry	Catalyst	Immobilization yield %	Activity yield %[a]	Activity (units/mg)[b]
1	**I**	69	34	6.8
2	**II**	71	31	6.2
3	**III**	90	42	8.4
4	**IV**	87	58	11.6

[a] The activity of native tyrosinase, evaluated by the dopachrome method, was 900 units/mg of enzyme.
[b]The enzyme loading is referred to the percentage of the initial tyrosinase supported on the catalyst.

Cyclic voltammetry analysis

Cyclic voltammograms (CVs) of catalysts **I-IV** were recorded at 25°C in comparison with parent OL nanoparticles as a reference. The analyses were carried out in 250 µM catechol solution (PBS buffer, 50 mM; pH 6.5), in the presence of KCl (100 mM) as supporting electrolyte. Irrespective to the catalysts studied, the electrocatalytic wave in CVs started in the correspondence of the formal potential ($E^{0'}$) of catechol (0.190 V) measured *versus* Saturated Calomel Electrode (SCE). Data are reported in Figure 2.27 (panels A-D; catalysts are marked by a red line, while the reference is reported as black line). As a general pattern, the CVs confirmed the previously observed trend for the activity parameters (Table 8). In particular, the CV of catalyst **I** (Figure 2.27, panel A) showed a well-defined electrocatalytic wave starting from 0.190 V *vs*. SCE and rising up to -20 µA cm^{-2} at -0.2 V *vs*. SCE. This data indicated that tyrosinase retained an appreciable electrocatalytic activity also in the encapsulation state. Catalyst **II** (Figure 2.27, panel B) was characterized by a weakly electrocatalytic responsiveness (electrocatalytic wave from 0.190 V *vs*. SCE to -4 µA cm^{-2} at -0.2 V *vs*. SCE), in accordance with the low activity yield previously measured (Table 8, entry 2). Afterwards, the electrocatalytic responsiveness of catalyst **III** was found to be increased (electrocatalytic wave from 0.190 V *vs*. SCE to -30 µA cm^{-2} at -0.2 V *vs*. SCE). Finally, catalyst **IV** showed the highest electrocatalytic wave compared to the other catalysts starting from 0.190 V *vs*. SCE to -56 µA cm^{-2} at -0.2 *vs*. SCE.

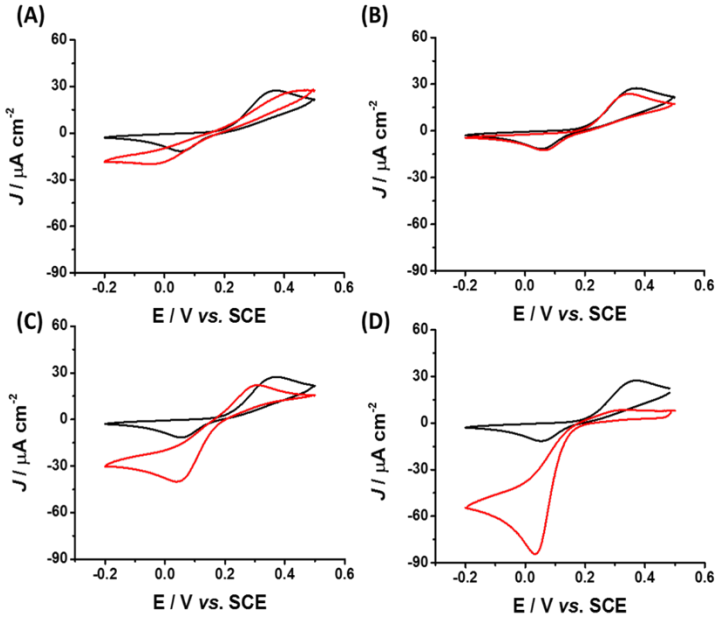

Figure 2.27. Cyclic voltammograms of OL nanocapsules (black line, A-D), Catalist **I** (red line, A), Catalyst **II** (red line, B), Catalyst **III** (red line, C) and Catalyst **IV** (red line, D) performed in 250 µM catechol solution (50 mM PBS buffer pH 6.5 + 100 mM KCl) at scan rate 5 mV s^{-1}.

*Kinetic properties of catalysts **I-IV** and synthesis of catechol derivatives*

Catalysts **I–IV** were characterized for their kinetic properties using L-Tyrosine (in the range 0.33–0.1 mM) as substrate and plotting data to a double reciprocal Lineweaver–Burk plot (Table 9). Data for native Tyrosinase are also reported as a reference (table 9, entry 1). Irrespective from the procedures used for the immobilization, V_{max} decreased and K_m increased for supported tyrosinase, which led to a partial reduction in the catalytic efficiency with respect to free enzyme. Similar trends in K_m and V_{max} values have been reported for tyrosinase immobilized on other carriers, they being attributed to mass transfer limitation processes[192].

Table 9. Kinetic parameters of Tyr and catalysts **I-IV**.

Entry	Catalyst	K_m (mM)	$V_{max} \times 10^{-3}$ (ΔAbs min μg_{enzyme})$^{-1}$	V_{max}/K_m ($x10^{-3}$)
1	Tyr	0.18	6.02	33.44
2	**I**	0.51	3.40	6.77
3	**II**	0.67	1.14	1.70
4	**III**	0.37	3.89	10.51
5	**IV**	0.25	4.10	16.40

All experiments were conducted in triplicate using free and immobilized tyrosinase. Average errors in kinetic parameters were 2–4% for Km and 1–3% for Vmax. L-Tyrosine was used as substrate.

Catalysts **III-IV** showed a higher rate and catalytic efficiency than catalysts **I-II** (Table 9, entries 4-5 versus entries 2-3), confirming the beneficial role of the LbL. Note that catalyst **I** was more active than catalyst **II** (Table 9, entry 2 versus entry 3), probably as a consequence of conformational changes occurring when the enzyme was directly adsorbed on the surface of the OL nanoparticles.

The synthetic versatility of catalysts **I-IV** was then evaluated in the oxidation of a panel of selected phenols **1**−**4** (Figure 2.28) to obtain the corresponding catechol derivatives **5-8**, including bioactive hydroxytyrosol **6**[192], and 3,4-dihydroxydihydrocinnamic acid **8**[193].

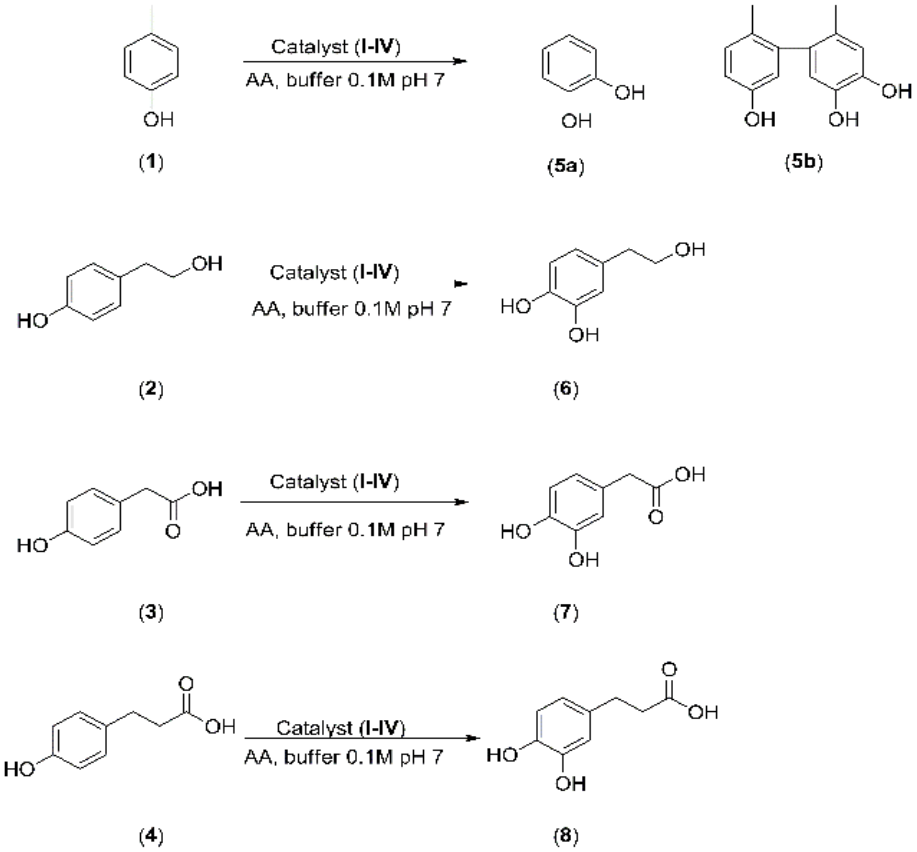

Figure 2.28. Oxidation of phenols **1**–**4** with catalysts **I–IV**

Catechols are characterized by several biological activities and are well recognized as antioxidant compounds[194]. The biotechnological potential of tyrosinase in the synthesis of catechols has received a great degree of attention because they are difficult to obtain under environmentally friendly conditions by means of traditional chemical procedures[195]. As a general procedure, phenols **1-4**, catalysts **I-IV** (540 units), and ascorbic acid AA (2.0 equiv) were stirred in PBS (0.1 M, pH 7.0, 5.0 mL) at room temperature, under a dioxygen atmosphere (O_2). Ascorbic acid was used as an internal reducing agent to avoid the polymerization of the quinone intermediates[196]. As a general trend, catalysts **I-IV** were able to oxidize phenols to corresponding catechols from moderate to high yield. No oxidation was observed in the presence of OL alone. Irrespective from the experimental conditions, catalysts **III** and **IV** were more reactive than catalyst **II**, affording the desired catechol in acceptable yields. The oxidations were very selective, catechol derivatives being the only isolated products besides to unreacted substrate. In the case of catalyst **I**, a lower selectivity was observed, since catechols were detected only in low yield with respect to the total conversion of substrate (Table 10, entry 2-5).

Table 10. Oxidation of Phenols **1**−**4** with Native Tyrosinase and Catalysts **I-IV**.

Entry	Catalyst	Substrate	Product(s)	% Conversion	%Yield
1	Tyr	1	5a	99	98
2	**I**	1	5a[5b]	91	20
3	**II**	1	5a	40	39
4	**III**	1	5a	59	59
5	**IV**	1	5a	75	75
6	Tyr	2	6	96	96
7	**I**	2	6	35	25
8	**II**	2	6	20	18
9	**III**	2	6	38	37
10	**IV**	2	6	46	46
11	Tyr	3	7	77	77
12	**I**	3	7	18	7
13	**II**	3	7	15	15
14	**III**	3	7	21	20
15	**IV**	3	7	28	28
16	Tyr	4	8	78	78
17	**I**	4	8	34	12
18	**II**	4	8	30	30
19	**III**	4	8	57	56
20	**IV**	4	8	67	65

The oxidation was performed on 0.02 mmol of substrate with the appropriate catalyst (540 units) in PBS (0.1 M pH 7) at 25°C under O_2 atmosphere for 24 h.

The low mass balance was probably due to over-oxidation processes, as confirmed by the isolation of a product of oxidative coupling, compound **5b**, in the oxidation of *para*-cresol **1** (Table 10, entry 2). Moreover, the low yield observed in the oxidation of phenol **3** (Table 10, entries 11-15) was probably ascribable to the known inhibitory activity reported for this compound against tyrosinase[197]. Recycling experiments proceeded with success in the oxidation of phenol **1**, as a selected example. After the first oxidation, catalysts **I-IV** were recovered by centrifugation, washed, and reused with fresh substrate. As shown in Table 11, catalysts **I-IV** were used for at least 5 cycles with only a slight decrease of activity.

Table 11. Recycling of catalyst **I-IV** in the oxidation of *para*-cresol **1.**

Entry	Run	Catalyst I (Yield %)	Catalyst I (Yield %)	Catalyst III (Yield %)	Catalyst IV (%Yield)
1	**1**	20	39	59	75
2	**2**	20	39	59	75
3	**3**	15	32	51	70
4	**4**	11	27	46	67
5	**5**	9	21	42	61

Reusability is expressed as the yield in % of catechol **5a** obtained by oxidation of 1 with catalyst **I-IV**.

2.4 Functionalized Laccase-Lignin Nanoparticles as Sustainable Catalysts for the Oxidation of Alcohol

2.4.1 Aim of work

In line with the previous work, in this project we exploited the ability of lignin to interact with laccase[112]. Laccases (benzenediol:oxygen oxidoreductases, EC 1.10.3.2)(Lac) are the simplest multi-copper enzymes in nature[198]. They oxidize phenols and other organic compounds by copper-mediated four electrons reduction of molecular oxygen to water, without the intermediate formation of hydrogen peroxide[199]. The industrial interest in these enzymes lies in their low substrate selectivity, high catalytic constants and thermal resistance[200], useful properties for bio-refinery processes[201], biosensors and biofuel cells[202]. The immobilization of Lac on solid supports improves the electro-chemical efficiency[203], the recovery of products and the multiple reuses in catalysis, with rapid termination of reactions and greater variety of bioreactor designs[204].

Different strategies have been reported for the Laccase immobilization on several support, including 1-aminopyrene mediated π-stacking interactions[205], amino linkers[206], hydroxyapatite nanocomposites[207], and cross-linking with glutaraldehyde/bovine serum albumin (BSA)[208], with or without the presence of redox mediators[209]. Redox mediators act as electron shuttles for the oxidation of substrates with high redox potential, diffusing far away from the active site[210]. These procedures show different degree of efficiency, due to conformational changes that can partially deactivate the enzyme (mainly in the case of covalent bonds)[211].

The folding structure of the protein, associated to the prevalence of Coulombic forces in non-ionic medium with respect to hydrogen bonding and hydrophobic polar type interactions, emerged as crucial parameters in the self-assembly of proteins on the lignin surface[164].

Moreover, lignin showed high boosting activity towards copper oxidative enzymes, such as Lytic Polysaccharide MonoOxygenases (LPMOs), through long-range electron transfer mechanisms between the aromatic moieties and the metal atoms in the active site of the enzyme[165].

The novel catalysts have been characterized regarding to their structural and kinetic properties, and they have been successively applied for the oxidation of selected alcohol to corresponding aldehyde.

Laccase is a promising biocatalyst with many possible applications, including bioremediation, chemical synthesis, bio-bleaching of paper pulp, biosensing, textile finishing and wine stabilization.

2.4.2 Experimental part

Preparation of cationic lignin

The cationization reaction of lignin was performed following the procedure from literature[91]. Briefly, a 10 mg/ml solution of lignin organosolv was prepared in 0.1 M NaOH followed by addition of glycidyl tetramethyl ammonium chloride (2 mg per mg of lignin) dropwise. The reaction occurred at 60 °C for 2 hours under magnetic stirring. Reaction product was dialyzed for 24 hours against deionized H2O using Spectrapore™ dialysis membrane (3.5 kD MWCO) (SPECTRUM, Dallas, TX, USA). The final yields of pH 7 soluble was 100% respect to initial lignin dry weight.

*Preparation of Catalyst **I***

Catalyst **I** preparation consist of encapsulating the enzyme in the OL nanocapsule. Briefly, an appropriate amount of laccase (2.0 mg, 1,05 U/mg) was added to a solution of OL in THF (2.0 mg/mL, 5.0 mL) previously filtered by a 0.45 µm filter membrane (PALL, Port, Washington, NY, USA). The solution obtained was dialyzed against deionized MilliQ water (SIEM, Bologna, Italy) (500 mL) for 24 h at 25 °C under slow magnetic stirring (STUART, Staffordshire, UK), using a Spectrapore™ dialysis membrane (3.5 kD MWCO) (SPECTRUM, Dallas, TX, USA). Catalyst **I** was recovered by centrifugation (20 min at 6000 rpm) (HETTICH, Tuttlingen, Germany) and the surnatant was used for the calculation of the activity parameters. The catalyst was washed several times with sodium acetate buffer 0.1M in order to ensure the complete removal of unbounded laccase (as evaluated by the Bradford method).

*Preparation of Catalyst **II***

Catalyst **II** was prepared by the random adsorption of laccase on preassembled OL nanoparticles prepared by the dialysis protocol[79]. Briefly, OL solution (THF, 2 mg/mL) previously filtered by a 0.45 µm filter membrane, was dialyzed against deionized water for 24 h at 25 °C with slow magnetic stirring, using a Spectrapore™ dialysis membrane (3.5 kD MWCO). Finally, the OL nanoparticles obtained were centrifuged (20 min at 6000 rpm), washed with Milli-Q water, and lyophilized. The appropriate amount of laccase (2.0 mg, 1.04 U/mg), dissolved in sodium acetate buffer (1.0 mL, 0.1 M; pH 5), was added to a suspension of OL nanoparticles (10 mg) in same buffer (15 mL) under orbital shaking at room temperature for 24 h. Catalyst **II** was recovered by centrifugation (20 min at 6000 rpm) and the surnatant was used for the calculation of activity parameters. The catalyst was washed several times with sodium acetate 0.1M buffer in order to ensure the complete removal of unbounded laccase (as evaluated by the Bradford method).

*Preparation of Catalyst **III***

The OL nanoparticles were coated with PDDA applying the LbL procedure[151]. Briefly, a suspension (15 mL) of OL nanocapsules in MilliQ water (1 mg/mL, pH 4.2) was added dropwise to PDDA solution (1 mg/mL, Milli-Q water) under slow magnetic stirring. After 2 h, the final suspension was centrifuged in order to recover OL-PDDA nanoparticles followed by washing with Milli-Q water and was then lyophilized. Laccase (2.0 mg, 1,04 U/mg) dissolved in sodium acetate buffer 0.1M (1.0 mL, 0.1 M; pH 5) was added to a suspension of OL-PDDA nanoparticles (10 mg) in same buffer (15 mL) under orbital shaking at room temperature for 24 h. Catalyst **III** was recovered by centrifugation (20 min at 6000 rpm) and the surnatant was used for the calculation of the activity parameters. The catalyst **III** was washed several times with sodium acetate buffer 0.1M in order to ensure the complete removal of unbounded laccase (as evaluated by the Bradford method).

*Preparation of Catalyst **IV***

The OL-PDDA nanoparticles were prepared as described above and then used in order to immobilize BSA and laccase by crosslinking with GA. Briefly, laccase (2.0 mg) and BSA (2.0 mg) were added to OL-PDDA nanoparticles suspension (4 mg/mL, 3 mL sodium acetate buffer 0.1M), and the mixture was shaken for 30 min at room temperature.

Finally, GA (150 μL, 2.5% v/v water solution) was added and the mixture was shaken again at room temperature for 30 min and then at 4 °C overnight. Catalyst **IV** was recovered by centrifugation (20 min at 6000 rpm) and the surnatant was used for the calculation of activity parameters. The catalyst was washed several times with sodium acetate buffer 0.1M in order to ensure the complete removal of unbounded laccase (as evaluated by the Bradford method).

*Preparation of Catalyst **V***

The OL nanoparticles were coated with CATLIG applying the LbL procedure[91]. Briefly, a suspension (15 mL) of OL nanocapsules in MilliQ water (20 mg/mL, pH 4.2) was added dropwise to CATLIG solution (1 mg/mL, Milli-Q water) under slow magnetic stirring. After 2 h, the final suspension was centrifuged in order to recover OL-CATLIG nanoparticles followed by washing with Milli-Q water and was then lyophilized. Laccase (2.0 mg, 1,04 U/mg) dissolved in sodium acetate buffer 0.1M (1.0 mL, 0.1 M; pH 5) was added to a suspension of OL-CATLIG nanoparticles (10 mg) in same buffer (15 mL) under orbital shaking at room temperature for 24 h. Catalyst **V** was recovered by centrifugation (20 min at 6000 rpm) and the surnatant was used for the calculation of the activity parameters. The catalyst **V** was washed several times with sodium acetate buffer 0.1M in order to ensure the complete removal of unbounded laccase (as evaluated by the Bradford method).

SEM Characterization

For Scanning Electron Microscopy (SEM), catalysts (**I**–**V**) were fixed with 3% GA in 0.1 M cacodylate buffer (pH 7.2), washed, and post-fixed in OsO_4 (1.0% in weight) in the same buffer at room temperature. The samples were dehydrated in ethanol series before the analysis, air dried, and sputter-coated with gold in a Balzers MED 010 unit (Balzers, Liechtenstein). The observation was made by a JEOL JSM 6010LA electron microscope (Tokyo, Japan).

Enzyme activity assay

Free laccase and each catalyst activity were assayed using 2,2'-azino-bis (3-ethylbenzothiazoline-6-sulfonic acid) diammonium salt as the substrate. The reaction mixture for the standard assay contained 5 mM ABTS, sodium acetate buffer (pH 5.0), and the enzyme solution in a total volume of 200 μL. The formation of the cation radical

was detected by measuring the absorbance increase at 420 nm (ε420= 36,000 M-1 · cm-1). One unit of laccase activity was defined as the amount of enzyme that catalyzed the oxidation of 1 μmol of ABTS in 200 μL reaction mixture at 25 °C in 1 min.

Kinetic Constants of Laccase

Michaelis-Menten constants (K_m) and catalytic constants (K_{cat}) of free laccases and each system were determined using various ABTS concentrations (125 μM–5000 μM) in sodium acetate buffer (pH 5.0). Lineweaver-Burke plots were drawn from the initial rates obtained at various substrate concentrations while the amount of enzyme was kept constant. The value are calculated by GraphPad software.

Identification and characterization of products

GC-MS analyses were performed on a Varian 450GC-320 MS apparatus using a SPB column (25 m × 0.25 mm and 0.25 mm film thickness) and an isothermal temperature profile of 70◦C for 2 min, followed by a 10 °C min−1temperature gradient to 280 °Cfor 25 min. The injector temperature was 280 °C. Chromatography-grade helium was used as the carrier gas with a flow of 1 ml/min. Mass spectra were recorded using a Varian 300 MS/MS with an electron beam of 70 eV. Acetophenone was used as internal standard.

Catalyst recycling

The reusability of catalysts **III**–**IV** was evaluated as follows: 4-methoxybenzyl alcohol (20 mM), immobilized Lac (0.65 U), and TEMPO (6 mM) were placed in Na-acetate buffer 0.1 M pH5 (1.0 ml). After 16 h, the catalyst was recovered by centrifugation and reused with fresh TEMPO (6.0 mM) and substrate (20 mM). For each run, the reaction mixture was extracted with EtOAc and the products analyzed by GC–MS.

Oxidation of alcohols: General procedure

Several aliphatic and aromatic alcohols was oxidized, including benzylalcohol **1**, 4-methoxybenzyl alcohol **2**, cinnamyl alcohol **3**, geraniol **4**, 4-cholorobenzyl alcohol **5**. The oxidations were carried out using the following conditions: alcohol (20 mM), catalysts I–V (0.65 U) and the mediator (TEMPO; 6.0 mM) were placed in 0.1 M Na-acetate buffer pH 5 (1.0 ml) in vigorous stirring at room temperature in presence of O_2. Reactions were monitored by thin layer chromatography (TLC). After the disappearance of the substrate,

the reaction mixture was extracted with ethyl acetate (EtOAc) (10 ml × 2 times). The organic extracts were treated with a saturated solution of NaCl and dried over anhydrous Na_2SO_4, then filtered and concentrated under vacuum to yield the crude. In the case of immobilized enzyme, catalysts **I**–**V** were recovered by filtration and the solution were subjected to the same work up described above.

2.4.3 Results and discussion

*Preparation of catalyst **I-V***

A total of five enzyme immobilization procedures were used: encapsulation (**I**), random adsorption (**II**), layer-by-layer adsorption using PDDA (**III)** or cationic lignin (CatLig) as positive layer, (**V**) and cross-linking method (**IV**).

Alkali Lignin nanoparticles have been previously reported as containers for drug delivery systems[184]. The catalyst **I** consisted in the formation of nanoparticles by slow solvent exchange in the presence of the Laccase to be immobilized. At the end, the encapsulated laccase was recovered by centrifugation and washed to remove the excess of the enzyme (Figure 2.29). Scanning electron microscopy (SEM) images of catalyst **I** are reported in Figure 2.30.

Catalyst **II** was prepared by exploiting the random interactions between the enzyme and the surface of lignin nanospheres such as π-π interaction, H-bond, hydrophobic and Van der Waals interactions.

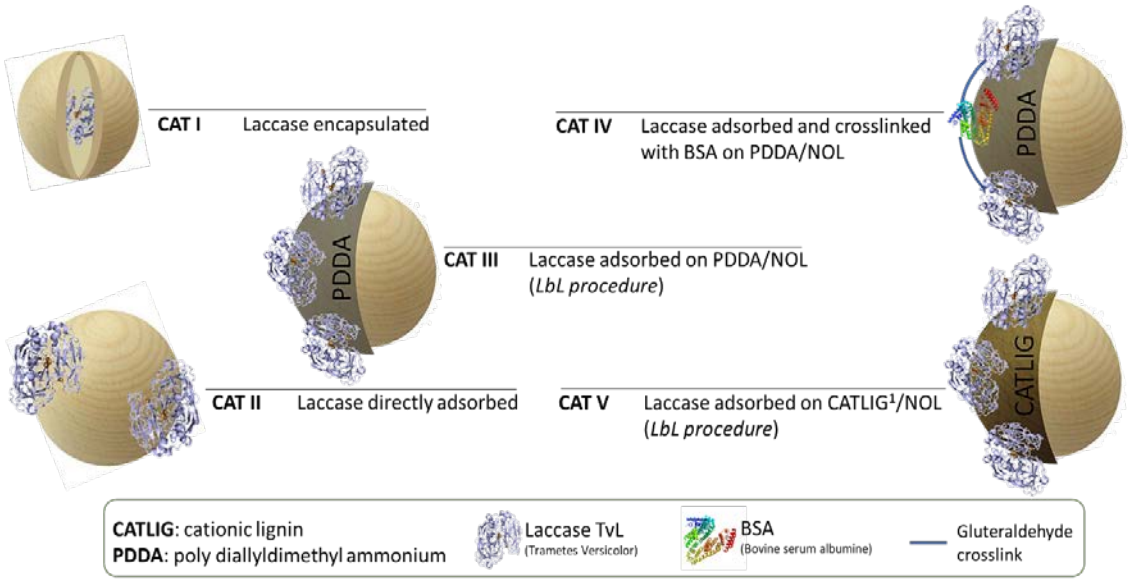

Figure 2.29 Schematic representation of the lignin nanosphere/laccase preparation procedure.

Recent studies explain that the peptides containing histidine, phenylalanine, proline, and serine residues had the best affinity to the lignin surface[112]. In this procedure the enzyme is immobilized maintaining its catalytic efficiency. Here the preformed lignin nanospheres are immersed directly in the enzyme solution. At the end, the randomly adsorbed laccase was recovered by centrifugation and washed to remove the excess of the enzyme. Scanning electron microscopy (SEM) images of catalyst **II** are reported in Figure 2.30.

Lignin nanospheres have a typical negative surface Z potential. This property makes it possible to coat the lignin surface with an opposite charge polyelectrolyte stabilized by the electrostatic attractions, typical of Layer by Layer technique (LbL). Catalyst **III** and **V** were prepared using LbL procedure, where the lignin nanosphere was coated with PDDA or Catlig respectively. The preformed nanospheres were coated by immersion in the appropriate polyelectrolyte solution and subsequently washed to remove the non-adsorbed excess. The coated nanospheres obtained are suitable for immobilization of the enzyme which instead shows an opposite negative charge. Generally, the nanospheres were immersed in the enzymatic solution where adsorption will take place. Scanning electron microscopy (SEM) images of catalyst **III** and **V** are reported in Figure 2.30.

The PDDA coated nanospheres were also used to prepare catalyst **IV** via cross-linking technique. Briefly, they were immersed in a solution of Laccase and BSA to achieve a co-adsorption process. After the washing step to remove the non-adsorbed protein excess, the nanospheres were inserted into a glutaraldehyde solution that cross-links the proteins

together. BSA performs as an inert protein with an isoelectric point close to that of tyrosinase, to partially reduce the amount of surface area available for the enzyme, while GA forms a protective three-dimensional network. Scanning electron microscopy (SEM) images of catalyst **IV** are reported in Figure 2.30.

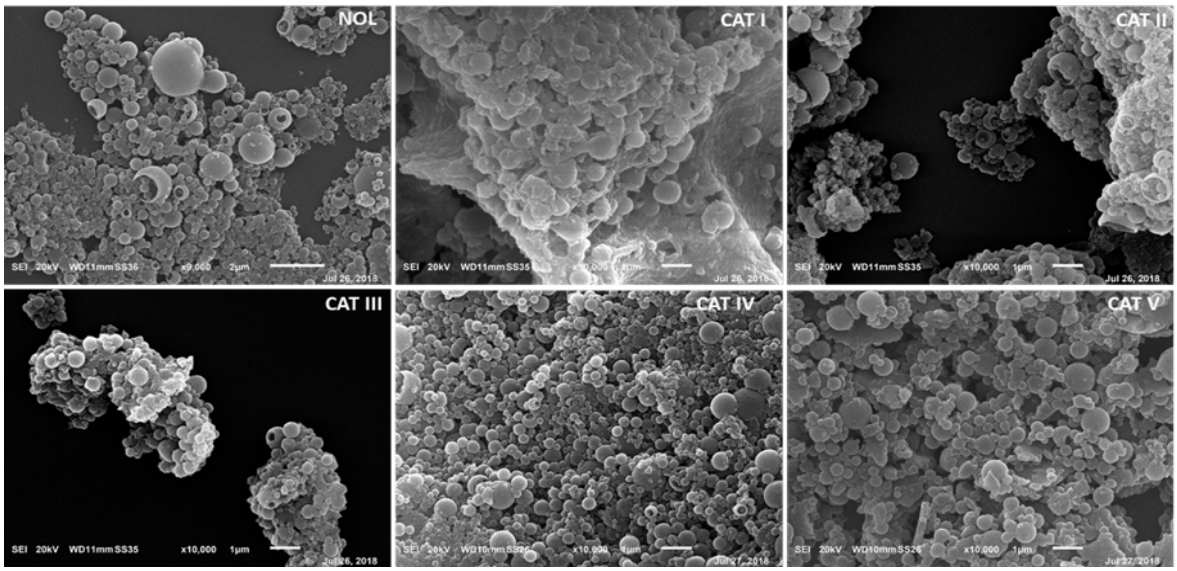

Figure 2.30 SEM images of standard nanosphere and catalysts

*Activity parameters of catalysts **I-V***

The Laccase (Lac) activity was determined by the ABTS assay[211], which accumulates following the oxidation of ABTS at 436 nm (the enzyme unit is defined as the increase in absorbance of 10^{-3} unit/min at 25 °C in 0.1M Na-acetate buffer, pH 5.0).

The immobilization and activity yields were evaluated as reported in equations 1 and 2, respectively:

$$\text{Activity (units/mg)} = Ux/Wsupport \quad (1)$$

$$\text{Activity yield (\%)} = [Ux/(Ua - Ur)] \times 100 \quad (2)$$

$$\text{Immobilization yield (\%)} = [(Ua - Ur)/Ua] \times 100 \quad (3)$$

Where Ua is the total activity (units) of the enzyme added to the solution and Ur is the residual activity (units) evaluated by the ABTS assay method in the washing solutions.

As reported in Table 12, catalysts **III-IV-V** showed a value of the immobilization yield higher than that of catalysts **I-II**, suggesting a better performance of the LbL procedure in the immobilization of laccase with respect to encapsulation and direct adsorption

procedures (entries 3-4 versus entries 1-2). The activity yield followed a similar trend. Note that catalyst **IV** was characterized by the highest value of the activity yield confirming the beneficial role of BSA and GA in the retention of the tyrosinase catalytic performance after the immobilization process. The activity of catalyst **II**-**IV** was comparable to that previously reported laccase[188] and tyrosinase based nanocatalysts[124].

Table 12. Loading factor and activity parameters of each catalyst**.**

Catalyst	Enzyme loading (%)[a]	Activity Yield (%)[b]	Activity (U/mg)	Immobilization yield (%)[c]
I	51,1	5,6	0,12	6,9
II	31,6	20,6	0,31	25,8
III	69,4	65,4	0,59	64,1
IV	72,1	65,7	0,71	66,6
V	60,6	54,1	0,56	55,2
Free LAC	-	-	1,066	-

Kinetic study of alcohol oxidation

Catalysts **I–IV** were characterized for their kinetic properties using ABTS (in the range 0.33–0.5 mM) as substrate and plotting data to a double reciprocal Lineweaver–Burk plot (Table 13). Data for native laccase are also reported as a reference (table 9, entry 6). Irrespective from the procedures used for the immobilization, V_{max} decreased and K_m increased for supported laccase, which led to an expected partial reduction in the catalytic efficiency with respect to free enzyme. Similar trends in K_m and V_{max} values have been reported for laccase immobilized on other carriers, they being attributed to mass transfer limitation processes[213].

Table 13. Kinetic parameters of each catalyst**.**

Run	Catalyst	K_m (mM)	V_{max} (x 10^{-3})[d]	V_{max}/K_m (x10^{-3})[e]	K_{cat} (s^{-1})
1	**Cat I**	**0,9 ± 0,001**	**99 ± 2**	**0,100**	**4 ± 8,2**
2	Cat II	0,21 ± 0,002	501 ± 12	2,385	41 ± 1,1

3	Cat III	0,17 ± 0,002	1245± 19	7,323	70 ± 2,0
4	Cat IV	0,16 ± 0,001	1525 ± 21	9,531	89 ± 1,9
5	Cat V	0,17 ± 0,003	1141 ± 18	6,711	64 ± 1,4
6	Free Lac	0,13 ± 0,002	1980 ± 29	15,230	98 ± 1,7

Catalysts **IV** followed by **III-V** showed the highest rate and catalytic efficiency with respect to catalysts **I-II** (Table 13, entries 3-4-5 versus entries 1-2), further confirming the beneficial role of the LbL procedure.

*Synthetic applications of catalysts **I-V***

The synthetic versatility of catalysts **I-V** was then evaluated in the oxidation of a panel of selected alcohols: benzyl alcohol **1**, 4-methoxybenzylalcohol **II**, cinnamyl alcohol **III,** geraniol **4** and 4-cholorobenzyl alcohol **5** to obtain the corresponding aldehyde derivatives **6-10** (Figure 2.30).

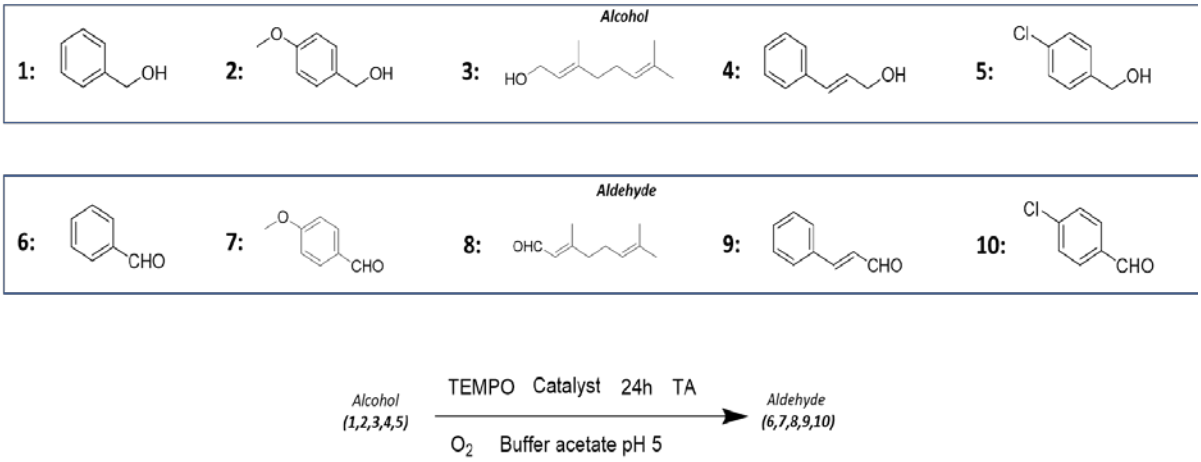

Figure 2.31 Substrates (alcohols) and products (aldehydes) and condition used for catalysis oxidation

The oxidative synthesis of aldehydes usually requires organometallic species with low selectivity and high environmental impact[214]. Briefly, compounds **1**–**5** (20 mM) and TEMPO (6 mM) were treated with catalysts **I**–**V** (0.65 U) in 0.1 M Na-acetate buffer pH 5 (1.0 ml) at 25◦C for 24 h (Figure 2.31). In the absence of the redox mediator, the oxidation was not observed, probably because none of the substrates are natural targets for Lac[215]. It is known that the active form of TEMPO is the oxoammonium ion. This intermediate oxidizes the alcohol to aldehyde producing the corresponding hydroxylamine that can be regenerated by reaction with the oxoammonium cations[216].

As expected, lignin nanosphere alone showed any catalytic activity. Catalysts **IV** and **V** showed a reactivity higher than catalyst **II** and **III** (see table 14). The presence of the LbL coating resulted in any appreciable kinetic barrier for the diffusion of the substrate. Catalyst **I** instead showed very low activity, probably for impossibility of the substrate to cross lignin shell towards inner. This behaviour of catalyst **I** was further confirmed by electrochemical studies. Generally, note that catalysts **II**–**V** performed better than Lac on Eupergit C250L, producing highest yield of aldehydes with a smaller amount of enzyme (i.e., 0.65 U for catalysts II–V compared to 10 U in the case of Eupergit C 250 L and respect to laccase immobilized on MWCNT[124].

Table 14. Yield of alcohol oxidation for each catalyst

Entry	Catalyst	Substrate	Product(s)	% Yield
1	I	**1**	**6**	0,1
2	II	**1**	**6**	3,5
3	III	**1**	**6**	45
4	IV	**1**	**6**	20,1
5	V	**1**	**6**	11,9
6	I	**2**	**7**	0,1
7	II	**2**	**7**	22,1
8	III	**2**	**7**	35,9
9	IV	**2**	**7**	99
10	V	**2**	**7**	98
11	I	**3**	**8**	**0,1**
12	II	**3**	**8**	35,4
13	III	**3**	**8**	50,6
14	IV	**3**	**8**	99
15	V	**3**	**8**	95
16	I	**4**	**9**	**0,1**
17	II	**4**	**9**	49,8
18	III	**4**	**9**	84,1
19	IV	**4**	**9**	99
20	V	**4**	**9**	99
21	I	**5**	**10**	**4**
22	II	**5**	**10**	6,3
23	III	**5**	**10**	36,5
24	IV	**5**	**10**	99
25	V	**5**	**10**	98

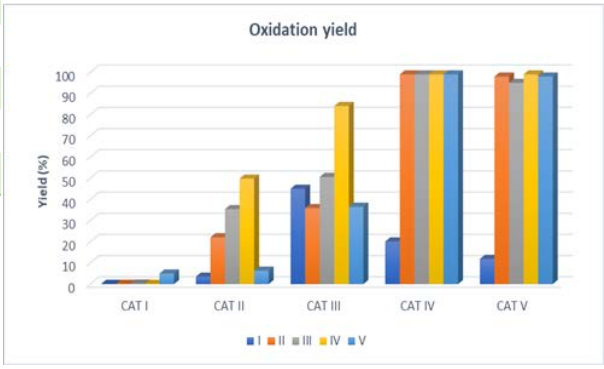

Data on variation of yield in function of time for the oxidation of compounds **2** with catalyst **V** are reported in figure 2.32, as selected representative examples. In accordance with reactivity of benzyl alcohol derivatives using catalyst Lac/TEMPO under similar experimental conditions, the rate of variation of yield increased by increasing the number of electron donor groups on the aromatic ring[217].

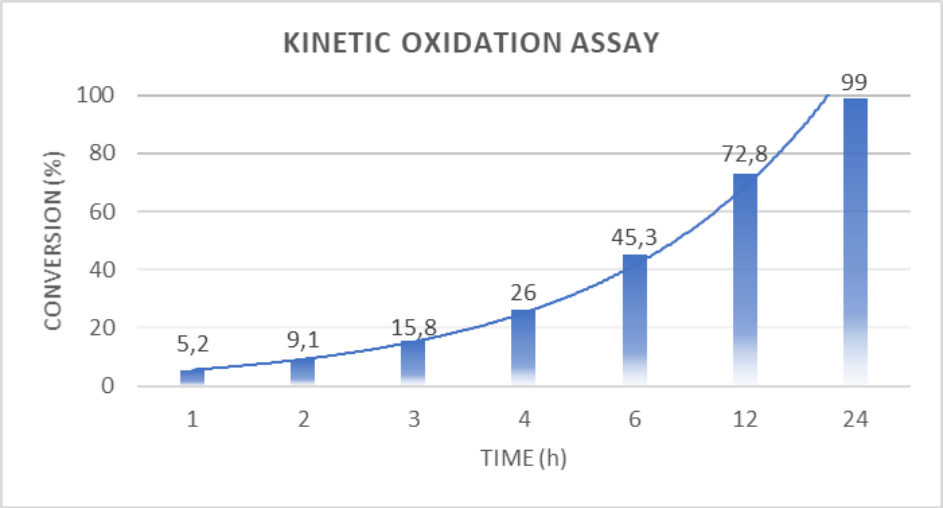

Figure 2.32 Kinetic study oxidation of catalyst **V**

The reusability of catalysts **III**–**IV** were evaluated by oxidation of 4-methoxybenzyl alcohol **2**, as a selected representative example. As a general trend, catalysts **IV** retained a reactivity higher than **III**, showing c.a. 50% con-version of substrate after 6 runs (Figure 2.33). These results further confirm the capability of the LbL procedure to create a specific microenvironment to protect the enzyme from denaturing agents[218].

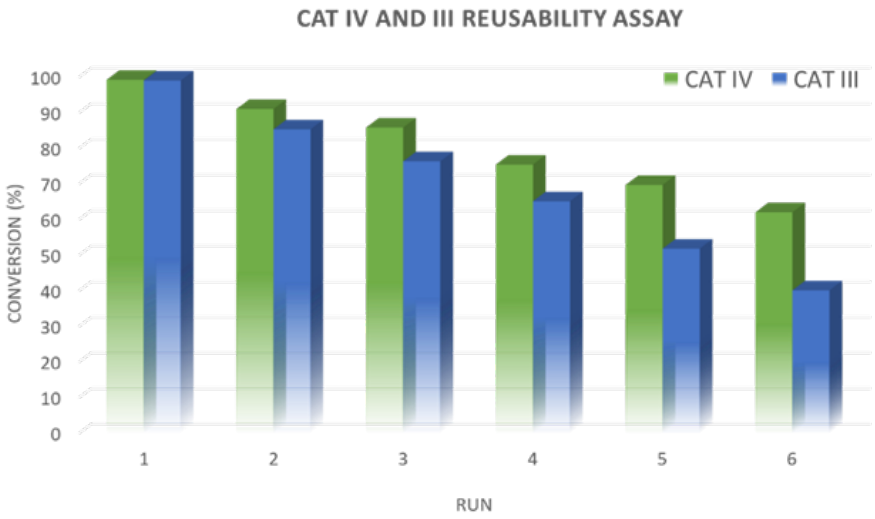

Figure 2.33. Catalysts recycle. Compounds 2 (20 mM) and TEMPO (6 mM) was treated with catalysts III–IV (0.65 U) in 0.1 M Na-acetate buffer pH 5 (1.0 ml) at 25◦C for 16 h. Results are the mean of three different experiments. Standard deviations were less than 3%.

Electrochemistry study

- *Pseudo-Direct electron transfer*

In order to demonstrate the influence of different immobilization methods of laccase (TvL) in/onto lignin nanocapsule (NOL) and the electrocatalytic behaviour of the so prepared catalysts, cyclic voltammogramms (CVs) were carried out in 120 mM Britton-Robinson (B-R) buffer pH 5.5. added with100 mM $KClO_4$ (pseudo-DET) and in ABTS solution prepared in 120 mM Britton-Robinson (B-R) buffer pH 5.5 added with 100 mM $KClO_4$ (MET). The pseudo-DET mechanism occurs at the electrode according to the following scheme (figure 2.34):

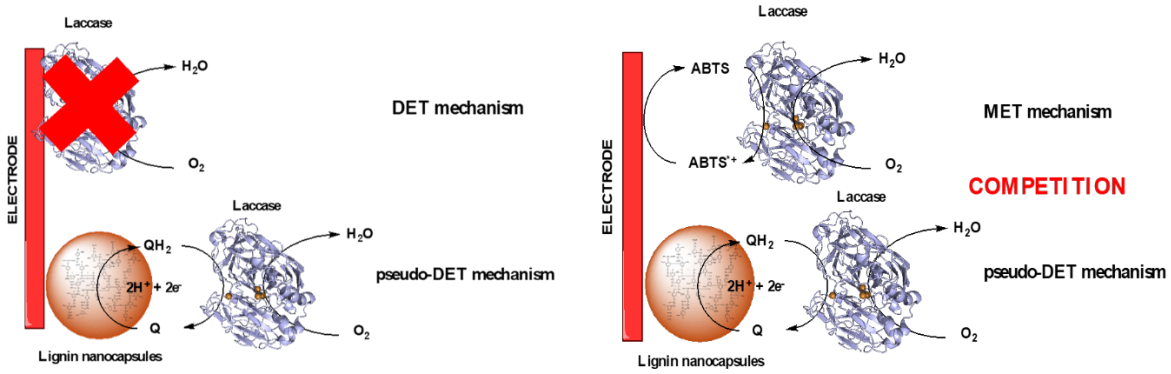

Figure 2.34. Electrocatalytic mechanism in absence and in presence of ABTS as freely diffusing mediator.

Figure 2.35 shows the CVs in absence of TvL (black line) and in presence of TvL encapsulated in the lignin nanocapsules (red line), where it is not possible to observe any catalytic effect. This result could be ascribed to the impossibility for laccase to be in direct contact with the electrode. On the one hand, it is impossible for the latter to donate electrons to the T1 site, hindering the internal electron transfer to T2/T3 cluster where the reduction of O_2 to H_2O occurs. On the other hand, it is possible to assume a hindering of O_2 diffusion occurring at the interface solution/nanocapsule, being low the amount of O_2 available as substrate for TvL.

Figure 2.35 B displays the CVs in absence of TvL (black line) and in presence of TvL randomly adsorbed onto NOL surface with a slight electrocatalytic wave starting at approximately EONSET= 0.398 V vs. SCE rising up to -23 µA cm-2 at 0 V vs. SCE. In this case, the result can be explained with the random orientation of enzyme onto the nanocapsules.

Afterwards, by applying a positive layer of PDDA on the layer-by-layer coating of NOL, it was possible to obtain a higher catalysis starting at approximately EONSET=

0.320 V vs. SCE rising up to -35 µA cm-2 at 0 V vs. SCE, as shown in the CV reported in Figure 2.35 C (red line). As mentioned before, the higher performance of this catalyst is ascribable to the positive electrostatic interaction between the PDDA layer, that is positively charged (δ+) at pH 5.5, and the partially negatively charged enzyme. Moreover, the hydrophobic interactions between PDDA and the hydrophobic pocket of the enzyme may positively affect the electrocatalytic properties of this catalyst.

Figure 2.35 D presents the CVs in absence of TvL (black line) and in presence of TvL cross-linked onto the PDDA layer by using BSA and GA (red line) with a slight electrocatalytic wave starting at approximately EONSET= 0.290 V vs. SCE rising up to -18 µA cm-2 at 0 V vs. SCE. In this case, the low effect can be ascribed to the packing of the enzyme associated to the cross-linking procedure which may hinder the oxygen diffusion and the electron transfer process.

Finally, Figure 2.35 E shows the CVs in absence of TvL (black line) and in presence of TvL adsorbed onto cationic lignin nanocapsules with a clear electrocatalytic wave starting at approximately EONSET= 0.315 V vs. SCE rising up to -25 µA cm-2 at 0 V vs. SCE. This result can be ascribed to the electrostatic interaction between the positively recharged nanocapsules (cationic lignin) and the negatively recharged laccase.

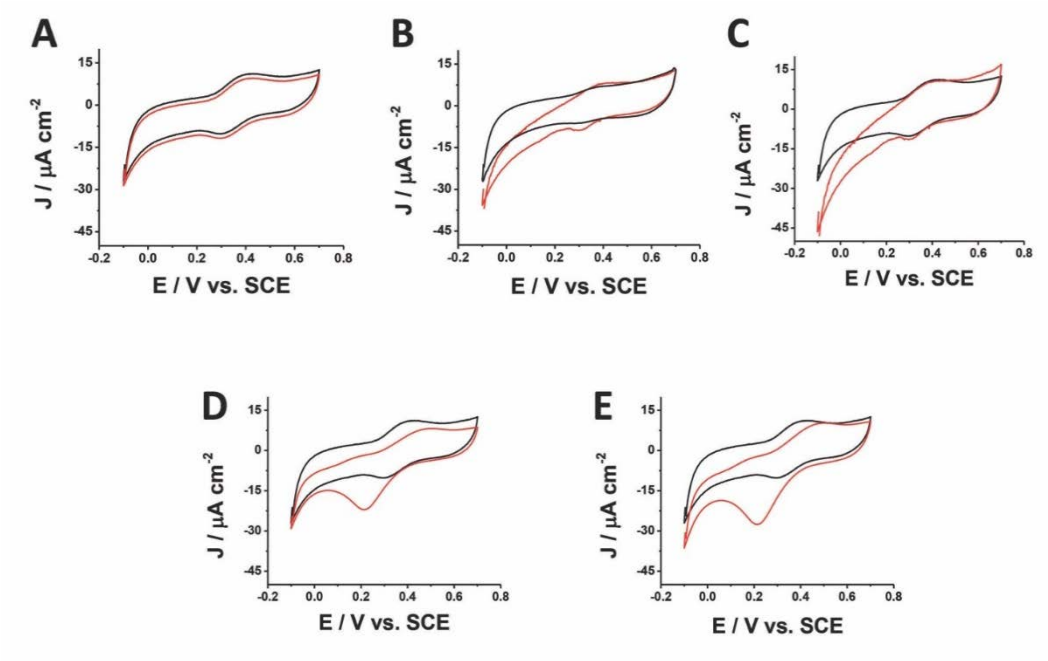

Figure 2.35 CVs of NOL (A-E, black line), Cat **I** (A, red line), Cat **II** (B, red, line), Cat **III** (C, red line), Cat **IV** (D, red line) and Cat **V** (E, red line) performed in 120 mM Britton-Robinson buffer pH 5.5 + 100 mM $KClO_4$ at a scan rate of 5 mV s^{-1}.

- *Mediated electron transfer*

In order to elucidate the mechanism governing the electron transfer of the different catalysts, we have performed also experiments in mediated electron transfer by using ABTS as mediator. Figure 2.36 A shows the CVs in absence of TvL (black line) and in presence of TvL encapsulated in the lignin nanocapsules (red line), where it is possible to observe a clear catalytic wave starting at approximately E_{ONSET}= 0.398 V vs. SCE rising up to -110 µA cm^{-2} at 0 V vs. SCE. In the black CV it is possible to observe only one couple of peaks even if there are two redox processes occurring at the electrode surface, namely ABTS/$ABTS^{\cdot+}$ redox process and QH_2/Q (for the lignin nanocapsules). This can be probably ascribed to the small difference in terms of formal potential and slow kinetics of the aforementioned redox processes. Since the electrocatalytic wave start approximately at the formal potential of ABTS and no other contributions can be observed, we can assume that the ABTS diffuses through the lignin nanocapsules donating the electrons to the T_1 site. However, the lower catalytic performance can be ascribed to the poor diffusion of O_2 through the lignin nanocapsules, as observed in the previous section for pseudo-DET experiments.

Figure 2.36 B displays the CVs in absence of TvL (black line) and in presence of TvL randomly adsorbed onto NOL surface with an evident electrocatalytic wave starting at approximately E_{ONSET}= 0.6 V vs. SCE rising up to -147 µA cm^{-2} at 0 V vs. SCE. In this case, it is possible to observe two contributions on the electrocatalytic signal, one for the mediated electron transfer operated from ABTS (catalytic wave starting at E_{ONSET}= 0.6 V vs. SCE) and the other for the pseudo-DET occurring at lignin nanocapsule surface (catalytic wave starting at E_{ONSET}= 0.32 V vs. SCE). The low electrocatalytic performance can be mainly ascribed to the random orientation of the enzyme onto the nanocapsules surface.

Afterwards, by applying a positive layer of PDDA on the layer-by-layer coating of NOL, it was possible to obtain the highest effect starting at approximately E_{ONSET}= 0.6 V vs. SCE rising up to -193 µA cm^{-2} at 0 V vs. SCE, as shown in the CV reported in Figure 2.36 C (red line). As mentioned before, there are two contributions on the electrocatalytic signal, one for the mediated electron transfer operated from ABTS (catalytic wave starting at E_{ONSET}= 0.6 V vs. SCE) and the other for the pseudo-DET occurring at lignin nanocapsule surface (catalytic wave starting at E_{ONSET}= 0.32 V vs. SCE). However, the highest performance of this catalyst is ascribable to the positive electrostatic interaction between the PDDA layer, positively charged (δ^+) at pH 5.5, and the partially negatively

charged enzyme. Moreover, also the hydrophobic interactions between PDDA and the hydrophobic pocket of the enzyme may positively affect the electrocatalytic properties of this catalyst.

Figure 2.36 D presents the CVs in absence of TvL (black line) and in presence of TvL cross-linked onto the PDDA layer by using BSA and GA (red line) with a lower electrocatalytic wave starting at approximately E_{ONSET}= 0.580 V vs. SCE rising up to -78 µA cm^{-2} at 0 V vs. SCE. In this case, it is still possible to observe both contributions (MET and pseudo-DET) but the low electrocatalytic wave can be ascribed probably to the hard packing of the enzyme through the cross-linking procedure which may hinder the oxygen diffusion and electron transfer process.

Finally, Figure 2.36 E shows the CVs in absence of TvL (black line) and in presence of TvL adsorbed onto cationic lignin nanocapsules with a clear electrocatalytic wave starting at approximately E_{ONSET}= 0.620 V vs. SCE rising up to -157 µA cm^{-2} at 0 V vs. SCE. In this case, it is still possible to observe both contributions (MET and pseudo-DET) while the clear electrocatalytic wave can be ascribed probably to the electrostatic interaction between the positively recharged nanocapsules (cationic lignin) and the negatively recharged laccase.

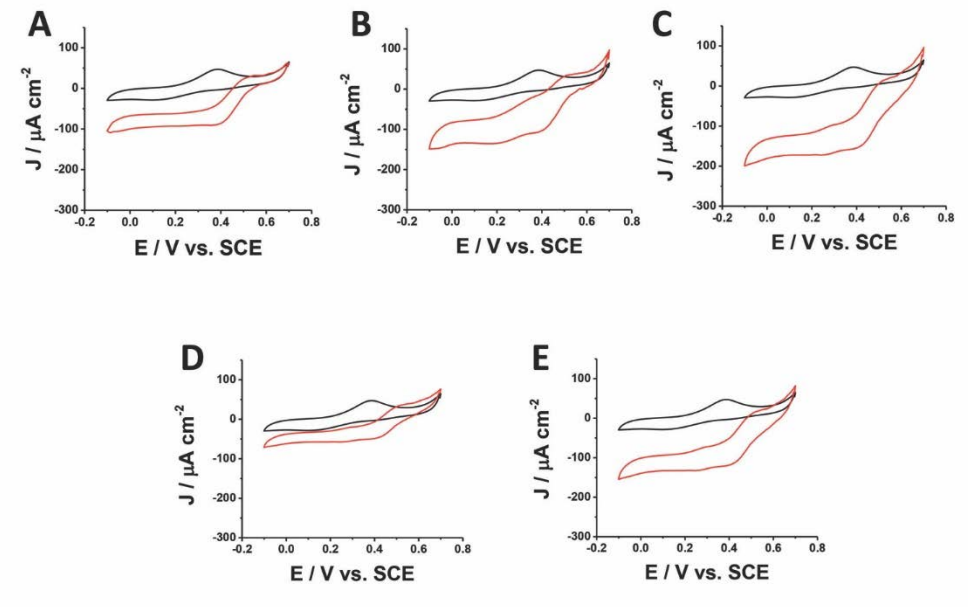

Figure 2.36 CVs of NOL (A-E, black line), Cat I (A, red line), Cat II (B, red, line), Cat III (C, red line), Cat IV (D, red line) and Cat V (E, red line) performed in 500 µM ABTS solution (120 mM Britton-Robinson buffer pH 5.5 + 100 mM $KClO_4$) at a scan rate of 5 mV s^{-1}.

- *Kinetic parameters determination*

To be able to investigate the influence of nanocapsules and different immobilization methods, several amperograms were recorded by applying a fixed potential of -0.050 V vs. SCE and injecting 25 µM ABTS every 40 s. The kinetic parameters (J_{max}, K_M^{app}) are listed in Table 15. The results are in good agreement with the results obtained by using CV. Figure 2.36 A presents the amperograms recorded for the different catalyst, while Fig. 3B displays the fitting obtained by using the Michaelis-Menten kinetic model.

Table 15. kinetic parameters (J_{max}, K_M^{app}) for the proposed catalysts.

Catalysts	J_{max} (µA cm^{-2})	K_M^{app} (mM)
I	171.5 ± 3.9	0.67 ± 0.05
II	247.7 ± 5.7	0.44 ± 0.02
III	381.0 ± 8.7	0.46 ± 0.03
IV	152.4 ± 3.5	0.38 ± 0.03
V	209.6 ± 4.8	0.32 ± 0.04

For the J_{max} values it is possible to establish a trend as follows: Cat IV < Cat I < Cat V < Cat II < Cat III, while the K_M^{app} seems to be quite similar except for the Cat I were the K_M^{app} is higher probably due to the diffusion of O_2 and ABTS through the nanocapsules.

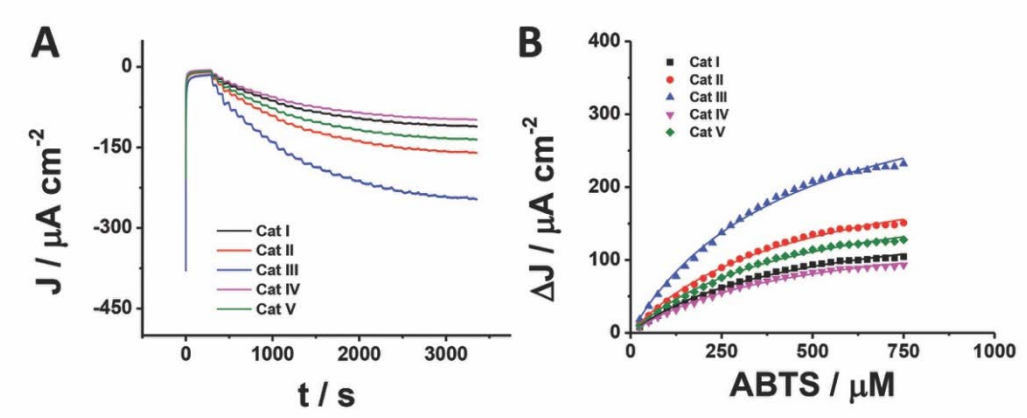

Figure 2.37. Chronoamperogram of Cat I (black), Cat II (red), Cat III (blue), Cat IV (purple) and Cat V (green) recorded by applying a fixed potential E_{app} = -0.050 V vs. SCE under constant stirring: 400 rpm. ABTS adding: 25 µM.

Chapter 3
Biomimetic systems

3.1 Tyrosinase mediated oxidative functionalization in the synthesis of DOPA-derived peptidomimetics with anti-Parkinson activity

3.1.1 Aim of work

Peptidomimetics are modified peptides[219] with optimal bioavailability and biological activity[220]. The modifications usually involve N-alkylation, Cα-substitution, Cα and N-replacement, heterocyclic generation, and backbone or side-chain transformations[221]. Among peptidomimetics, DOPA derivatives are of interest in the therapy of the Parkinson disease (PD)[222]. PD is one of the most important neurodegenerative disorder, characterized by dopamine (DA) neuron loss in the substantia nigra pars compacta (SNpc) and depletion of DA content in the dorsal striatum, which causes tremor at rest, muscle rigidity, akinesia (or bradykinesia) and postural instability[223].

DOPA peptides penetrate the blood brain barrier (BBB) by the aid of specific peptide-mediated carrier transport systems (PMCTS)[224], restoring adequate DA concentration in the surviving dopaminergic (DAergic) neurons[225]. They also preserve DOPA from the occurrence of fast metabolic decarboxylation, avoiding the peripheral DA-related side effects (cardiac arrhythmias, vomiting and hypotension)[226]. DOPA peptides showed bioavailability and anti-PD activity higher than DOPA[227].

The main synthetic pathway for the preparation of DOPA peptides is the solid-state procedure[228]. This synthesis often requires tedious and long-time protecting/de-protecting steps, with intrinsic low selectivity[229]. As an alternative, procedures based on the oxidative side chain modification of amino acids have been applied[230]. The synthesis of DOPA peptides by selective oxidation of tyrosine residues with tyrosinase from *Agaricus bisporus* was reported[231]. Tyrosinase (monophenol, o-diphenol: oxidoreductase, E.C. 1.14.18.1) is a metalloprotein able to activate di-oxygen for the conversion of tyrosine to DOPA (creolase or monophenolase activity) and to DOPA quinone (catecholase or diphenolase activity, respectively). The replacement of the natural amide bond in peptides with unusual covalent linkages is a general strategy to improve the stability and activity of the molecule[232]. We recently reported the synthesis of DOPA peptidomimetics with stable O-C and N-C covalent bonds by oxidative functionalization of tyrosine with 2-iodoxybenzoic acid (IBX)[233], that is a biomimetic system of tyrosinase. The reaction proceeded

through a Michael-like 1,4-addition of oxygen and nitrogen centred α–amino acids to reactive DOPA ortho-quinone intermediate[234]. DOPA peptidomimetics containing glycine residues showed the highest antioxidant effect in the 2,2-diphenyl picrylhydrazyl (DPPH) test, while valine derivatives were the most active compounds in the comet assay in L5178Y (TK+/-) mouse lymphoma cells.

The role of the oxidative stress in PD has been debated and reviewed[235]. Data suggested that the oxidative damage by active radical species might contribute to the cascade of events leading to degeneration of DAergic neurons[236].

In this project was studied the directly application of tyrosinase for the nucleophilic oxidative functionalization of tyrosine residues to yield DOPA peptidomimetics bearing stable O-C and N-C bonds and characterized by antioxidant and anti-Parkinson activities. The reaction was effective under heterogeneous conditions after immobilization of tyrosinase on multi walled carbon nanotubes (MWCNTs). The main advantages of heterogeneous catalysis derive from the easy product isolation, high enzyme loading and recyclability, thus minimizing the cost of the processes[237]. The anti-Parkinson activity of novel DOPA peptidomimetics was evaluated by electrophysiological recordings on individual dopaminergic neurons in rat ex vivo midbrain slices, based on the ability of novel DOPA peptidomimetics to reproduce the effects of DA and DOPA observed on the DAergic neurons in physiological conditions. Indeed, the low content of DA in the basal ganglia nuclei occurring in PD is currently mainly treated with DOPA which is converted to DA by the aromatic amino acid decarboxylase enzyme. Therefore, the efficacy of potential anti-PD drugs should be expressed through their ability to mimic DA/DOPA effects.

3.1.2 Experimental

Materials

Mushroom tyrosinase from Agaricus bisporus (Tyr), multi-walled carbon nanotubes (MWCNTs), L-tyrosine, bovine serum albumin (BSA), glutaraldehyde (GA), polydiallyldimethylammonium chloride (PDDA), sodium sulfate anhydrous (Na_2SO_4), Boc-Tyrosine-OMe, amino acids differently protected and organic solvents were purchased from Sigma–Aldrich. All spectrophotometric measurements were made with a Varian Cary50 UV–Vis spectrophotometer equipped with a Peltier thermostatted single cell holder. 1H and 13C NMR spectra were recorded on a Bruker (400 MHz) spectrometer. Mass spectra were recorded on a VG

70/250S spectrometer with an electron beam of 70 eV. All experiments were done in triplicate using native and immobilized tyrosinase in EtOH/buffer system and in H_2O medium. Sodium phosphate [(PBS) 0.1 M, pH 7.0] was used as the buffer solution.

Preparation of catalyst MWCNT/Tyr.

MWCNT/Tyr was prepared as previously reported[238]. Briefly, PDDA coated MWCNTs in PBS were treated with a mixture of Tyr (0.2 mg) and BSA (0.6 mg) for 30 minutes. Glutaraldehyde (GA, 2.5%) was added to reach a final volume of 800 μL and the mixture was shaken at 25°C for 30 min and at 4°C overnight. The excess enzyme and GA were removed by centrifugation (6000 rpm x 20 min) and the surnatant was used for the calculation of activity parameters. The catalyst was finally treated with 1.5 mL TRIS-HCl 0.1M pH 7.2 by shaking for 1h at 4°C and centrifuged. MWCNT/Tyr was washed several times with PBS in order to ensure the complete removal of unbounded Tyr (as evaluated by the Bradford method).

Activity data.

The activity of native and immobilized Tyr was determined by measuring the oxidation of L-tyrosine. The reaction was started by adding L-tyrosine to the solution of Tyr or MWCNT/Tyr in PBS under magnetic stirring. The initial rates were measured as linear increase in optical density at 475 nm, due to dopachrome formation. One unit of enzyme activity was defined as the increase in absorbance of 0.001 per minute at pH 7, 25°C in a 3.0 mL reaction cuvette containing 0.83 mM of L-tyrosine and 67 mM of PBS pH 7.0. The activity was expressed as activity unit per milligram of support:

$$\text{Activity (U/mg)} = Ux/W_{support}$$

where Ux is the activity of the immobilized enzyme assayed by dopachrome method. The activity yield represents the % of the ratio of activity of the immobilized enzyme to the total units of native enzyme used:

$$\text{Activity Yield (\%)} = [Ux/(Ua - Ur)] \cdot 100$$

where Ua is the total activity of enzyme (unit) added in the solution and Ur is the activity of the residual Tyr (unit) evaluated by dopachrome method in the washing solutions. The immobilization yield is defined as:

$$\text{Immobilization Yield (\%)} = [(Ua - Ur)/Ua] \cdot 100$$

General procedure for preparation of Dopa peptidomimetics

BTO **1** (0.068 mmol) was dissolved in 12 mL of EtOH/ PBS v/v, then amino acid (0.68 mmol) and tyrosinase from *Agaricus bisporus* or Tyr/MWCNT (600 UA) were added. The reaction mixture was stirred at 25°C for 24h. The reaction was monitored by thin layer chromatography (TLC, n-hexane/EtOAc = 2.0:1.0). After the disappearance of substrate, the reaction mixture was treated with 2 mL of H_2O and 2.0 eq. of Na_2S2O_4 stirring for 15 min. Then was added 2 mL of saturated solution of $NaHCO_3$ and stirring for 30 min. The mixture was extracted several time with AcOEt and separated from H_2O. The organic layers were collected dried with Na_2S2O_4 and concentrated under reduced pressure. The crude product was purified by flash-chromatography. Compounds Gly-N-C-Dopa **6**, Val-N-C-Dopa **7**, Gly-O-C-DOPA **8**, and Val-O-C-DOPA **9** were obtained from compounds **2**,**3**,**4** and **5** respectively using an aqueous solution of HCl 6N for 2h at reflux. The crude was then concentrated under reduced pressure and washed with hexane to yield the desired products.

Spectroscopic data

OMe-Gly-N-Boc-DOPA-OMe (2) Oil 1H NMR (400 MHz, CDCl3): δH (ppm) = 1.44 (9H, s, 3×CH3), 2.90-3.10 (2H, m, CH2), 3.74 (3H, s, OCH3), 3.93 (2H, s, CH2), 4.11 (3H, s, OCH3), 4.62-5.14 (1H, m, CH) , 7.24 (1H, s, CH), 7.42 (1H, s, CH) 13C NMR (100 MHz, CDCl3): δH (ppm) = 28.04 (3×CH3), 32.21 (CH2), 42.89 (CH2) 52.47 (OCH3), 52.59 (OCH3), 56.59 (CH), 80.48 (-C□), 113.58 (Car), 117.31 (Car), 119.31 (Car), 141.44 (Car), 144.76 (Car), 146.56 (Car), 158.32 (C=O), 171.90 (C=O), 172.64 (C=O). MS (EI): m/z 399; Elemental Analysis calcd: C, 54.26; H, 6.58; N, 7.03; O, 32.13 Elemental Analysis found: C, 54.25; H, 6.59; N, 7.08; O, 32.13.

N-Boc-Gly-N-Boc-Dopa-OMe (3) Oil 1H NMR (400 MHz, CDCl3): δH (ppm) = 1.28(9H, s, 3×CH3), 1.44 (9H, s, 3×CH3), 2.97-3-00 (2H, m, CH2), 3.74 (3H, s, OCH3), 3.94 (2H, s, CH2) 4.62-5.14 (1H, m, CH) , 7.24 (1H, s,CH), 7.42 (1H, s, CH). 13C NMR (100 MHz, CDCl3): δH (ppm) = 28.08 (3×CH3), 28.70 (3×CH3), 32.47 (CH2), 42.89 (CH2) 52.47 (OCH3), 55.79 (CH), 79.53 (-C□), 80.48 (-C□), 113.58 (Car), 117.31 (Car), 119.31 (Car), 141.44 (Car), 144.76 (Car), 146.56 (Car), 155.80 (C=O), 158.32 (C=O), 171.90 (C=O), 172.64 (C=O). MS (EI): m/z 485; Elemental Analysis calcd: C, 54.54; H, 6.66; N, 5.78; O, 33.02 Elemental Analysis found: C, 54.51; H, 6.62; N, 5.73; O, 33.01.

OMe-Val-N-Boc-Dopa-OMe (4) Oil 1H NMR (400 MHz, CDCl3): δH (ppm) = 0.89 (6H, d, 2×CH3) J=4, 1.32 (9H, s, 3×CH3), 2.90-3.10 (3H, m,CH,CH2), 3.74 (3H, s, OCH3), 3.76-3.83 (1H, m, CH), 3.81(3H,s,OCH3), 4.49-5.10 (1H, m, CH), 7.49 (2H, s, 2xCH) 13C NMR (100 MHz, CDCl3): δH (ppm) = 19.25 (2xCH3), 28.04 (3×CH3), 30.63 (CH), 32.21 (CH2), 52.47 (OCH3), 52.59 (OCH3), 55.81 (CH), 74.30 (CH), 80.48 (-C□), 113.58 (Car), 117.31 (Car), 119.31 (Car), 142.34 (Car), 144.76 (Car), 146.56 (Car), 158.32 (C=O), 171.90 (C=O), 172.64 (C=O). MS (EI): m/z 441; Elemental Analysis calcd: C, 57.26; H, 7.32; N, 6.36; O, 29.06 Elemental Analysis found: C, 57.23; H, 7.31; N, 6.36; O, 29.05.

N-Boc-Val-N-Boc-DOPA-OMe (5) Oil 1H NMR (400 MHz, CDCl3): δH (ppm) = 0.89-0.98 (6H, d,2×CH3) J=4, 1.07(9H, s, 3xCH3), 1.30 (9H, s, 3xCH3), 2.96-3.03 (3H, m,CH,CH2), 3.74 (3H, s, OCH3), 3.74-3.85 (1H, m, CH), 4.52-5.14 (1H, m, CH) 7.49 (2H, s, 2xCH) 13C NMR (100 MHz, CDCl3): δH (ppm) = 18.90 (2xCH3) 28.08 (3×CH3), 28.70 (3×CH3), 30.41(CH), 32.47 (CH2), 52.47 (OCH3), 55.79 (CH), 62.71 (CH), 79.53 (-C□), 80.48 (-C□), 113.58 (Car), 117.31 (Car), 119.31 (Car), 141.44 (Car), 144.76 (Car), 146.56 (Car), 155.80 (C=O), 158.32 (C=O), 171.90 (C=O), 172.64 (C=O). MS (EI): m/z 527; Elemental Analysis calcd: C, 57.02; H, 7.27; N, 5.32; O, 30.38 Elemental Analysis found: C, 57.00; H, 7.23; N, 5.29; O, 30.35

Gly-N-C-Dopa (6) White solid 1H NMR (400 MHz, D2O): δH (ppm) =2.90-3.08 (2H, m, CH2), 3.92(2H, s, CH2), 4.59-5.15 (1H, m, CH) J=4, 7.24 (1H, s, CH), 7.42 (1H, s, CH). 13C NMR (100 MHz, D2O): δH (ppm) = 34.70 (CH2), 46.29 (CH2), 56.69 (CH), 99.58 (Car), 115.21 (Car), 117.54 (Car), 134.44 (Car), 139.16 (Car), 145.65 (Car), 176.70 (COOH), 182.24 (COOH). MS (EI): m/z 271.09; Elemental Analysis calcd: C, 48.89; H, 5.22; N, 10.37; O, 35.52 Elemental Analysis found: C, 48.86; H, 5.19; N, 10.36; O, 35.53.

Val-N-C-Dopa (7) White solid 1H NMR (400 MHz, D2O): δH (ppm) = 0.89 (6H, d, 2×CH3) J=4, 2.34 (1H, m,CH), 2.89-3.10 (2H, m, CH2), 4.25-4.37(1H, m, CH), 4.50-5.10 (1H, m, CH), 7.30 (1H, s, CH) 7.50 (1H, s, CH) 13C NMR (100 MHz, D2O): δH (ppm) = 19.25 (2xCH3), 30.33 (CH), 34.71 (CH2), 56.74 (CH), 76.86 (CH), 99.54 (Car), 115.81 (Car), 116.35 (Car), 134.34 (Car), 139.76 (Car), 146.56 (Car), 179.84 (COOH), 180.25 (COOH). MS (EI): m/z 313.14; Elemental Analysis calcd: C, 53.84; H, 6.45; N, 8.97; O, 30.74 Elemental Analysis found C, 53.80; H, 6.50; N, 8.93; O, 30.77.

Gly-O-C-Dopa (8) White solid 1H NMR (400 MHz, D2O): δH (ppm) = 2.90-3.10 (2H, m, CH2), 3.93 (2H, s, CH2) 4.62-5.14 (1H, m, CH), 7.21 (1H, s,CH), 7.40 (1H, s, CH). 13C NMR (100 MHz, D2O): δH (ppm)= 33.57 (CH2), 39.89 (CH2), 56.77 (CH), 107.23 (Car), 110.66 (Car), 119.31 (Car), 127.46 (Car), 145.61 (Car), 146.30 (Car), 168.20 (COOR), 174.24 (COOH). MS (EI): m/z 271.09; Elemental Analysis calcd: C, 48.89; H, 5.22; N, 10.37; O, 35.52 Elemental Analysis found: C, 48.80; H, 5.18; N, 10.42; O, 35.59.

Val-O-C-Dopa (9) White solid 1H NMR (400 MHz, D2O): δH (ppm) = 0.80-0.95(6H, d,2×CH3) J=4, 2.50-2.60 (1H, m, CH), 2.90-3-10 (2H, m, CH2),4.11-4.20 (1H, m, CH) 4.50-5.02 (1H, m, CH) 7.45 (2H, s, 2xCH) 13C NMR (100 MHz, D2O): δH (ppm) = 18.90 (2xCH3), 30.43(CH), 33.57 (CH2), 57.75 (CH), 59.21 (CH), 111.26 (Car), 117.61 (Car), 120.36 (Car), 143.56 (Car), 146.73 (Car), 146.91(Car), 168.95 (COOH), 174.14 (COOH). MS (EI): m/z 313.14; Elemental Analysis calcd: C, 53.84; H, 6.45; N, 8.97; O, 30.74 Elemental Analysis found: C, 53.78; H, 6.52; N, 8.94; O, 30.79.

Electrophysiological recordings

- *Slice preparation for electrophysiology*

Preparation of midbrain slices was performed as described previously[239] from Wistar rats (P18–P23, either sex). Horizontal slices (thickness 250 or 300 µm) containing the substantia nigra pars compacta (SNpc) and the ventral tegmental area (VTA), were cut with in ice-cold modified artificial CSF (ACSF). This solution contained (in mM): 126 NaCl, 2.5 KCl, 1.2 MgCl2, 1.2 NaH_2PO_4, 2.4 $CaCl_2$, 10 glucose, and 24 $NaHCO_3$, 290 mOs/L, and was gassed with 95% O_2–5% CO_2, pH 7.4. Slices were kept in a holding chamber containing ACSF at 32°C, gassed with 95% O2–5% CO_2 for at least 40 min after slicing procedures. After recovery period, one single slice was transferred to the recording chamber.

- *Multi-electrode assay recordings*

Extracellular signals were acquired on a planar multi-electrode array (MEA) device using the MED64 System (Alpha MED Sciences, Osaka, Japan). Horizontal midbrain slices (300 µm) were placed over an 8×8 array of planar microelectrodes, each 20×20 µm in size, with an interpolar distance of 100 µm (MED-P2105, Alpha MED Sciences, Osaka, Japan) as previously described[240]. Signals were low-cut filtered at 100 Hz and digitized at 100 kHz using Mobius software (Alpha MED Sciences, Osaka, Japan). The fast transients corresponding to spontaneous action potentials were captured off-line and sorted using Spike2 6.0 software (Cambridge Electronic Design Ltd,

Cambridge, UK). The basal firing frequency was measured over a period of 3 min, before challenging the slices with a 30 sec perfusion of DA 30 µM. The relative change in firing frequency was calculated by the mean frequency during the last few seconds of DA perfusion with respect to the control period. Only cells that were inhibited by DA, with inhibition exceeding 15% of control firing, were considered in the present study.

- *Whole cell patch clamp recordings in SNpc DAergic neurons.*

Recordings were performed accordingly to Guatteo et al.[239]. SNpc DAergic neurons, localized in a region of tightly packed neurons adjacent to the medial terminal nucleus of the accessory optic tract, were identified based on a slow and regular spontaneous firing (1–5 Hz), hyperpolarizing/outward response to dopamine (DA, 30 µM), prominent Ih in response to hyperpolarizing voltage steps (-60 to -120 mV, 20 mV increment, holding potential, Vh, -60 mV)[241] and, in current-clamp mode, a depolarizing sag upon application of negative currents[242]. Patch pipettes (2–5 MΩ) were filled with a solution containing (in mM): K-gluconate (135), CaCl2 (0.1), $MgCl_2$ (2), KCl (10), EGTA (0.75), HEPES (10), Mg_2-ATP (4), and Na_3-GTP (0.3), phosphocreatine-Na_2 (10), pH 7.3, osmolarity 280 mOs/L.

3.1.3 Results and discussion

Synthesis of DOPA peptidomimetics under homogeneous conditions.

The tyrosine derivative Boc-Tyr-OMe (BTO) **1** protected at both the amino moiety (as tert-butoxycarbonyl; Boc, green) and carboxylic group (as methyl ester; cyano) was used as starting material. Reactions were designed according to the general procedure previously applied with IBX and are generalized in Figure 3.1.

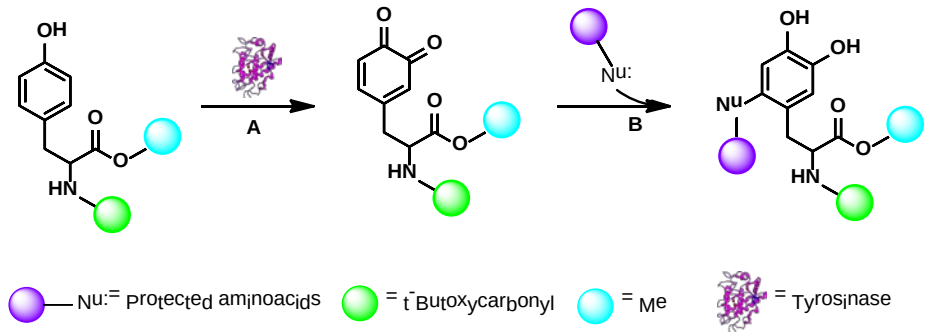

Figure 3.1 General reactivity scheme of Boc-Tyr-OMe (BTO) **1** with α-amino acids in the presence of tyrosinase from Agaricus bisporus. Step A: oxidation of tyrosine to DOPA-quinone. Step B: Michael-like 1-4-addition of α-amino acids on the DOPA-quinone intermediate, followed by the reduction step with $Na_2S_2O_4$.

Briefly, the oxidation of BTO **1** (20 mg, 0.068 mmol) with tyrosinase from *Agaricus bisporus* (600 UA) was performed in the presence of the appropriate α-amino acid derivative (0.68 mmol) in phosphate buffer solution (PBS; pH 7) and EtOH (from 9:1 v/v to 1:9 v/v PBS/EtOH ratio, respectively) at 25 °C, followed by the reduction step with $Na_2S_2O_4$. EtOH showed a complete miscibility and high compatibility with PBS in various enzymatic reactions[243]. Initially, glycine methyl ester (NH_2-Gly-OMe) was used as nitrogen centred nucleophile for the addition on the reactive DOPA ortho-quinone intermediate. The DOPA peptidomimetic OMe-Gly-N-Boc-DOPA-OMe 2 was obtained in the highest yield (87%) in the presence of PBS/EtOH 3:7 v/v after 24h, besides to unreacted BTO (Figure 3.2; Figure 3.3, pathway A; Table 12).

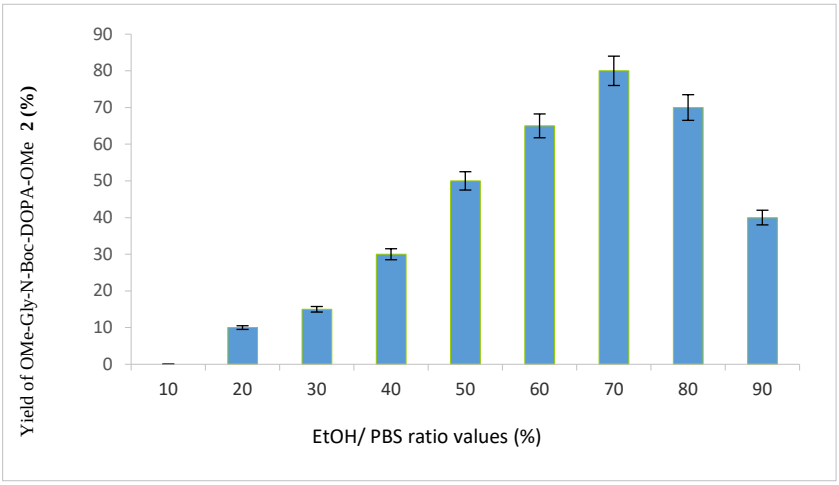

Figure 3.2. Yield (%) of OMe-Gly-N-Boc-DOPA-OMe **2** during the oxidation of BTO **1** with tyrosinase *from Agaricus bisporus* in the presence of NH_2-Gly-OMe at different EtOH/ PBS ratio values.

The oxidative functionalization of BTO **1** was then repeated using N-Boc-glycine (Boc-Gly-COOH) as oxygen centred nucleophile under optimal conditions, to yield N-Boc-Gly-N-Boc-DOPA-OMe **3** in 80% yield (Table 12, entry 3), besides to residual BTO (Figure 3.3, pathway B). To evaluate the generality of the transformation, we used the more hindered amino acids NH_2-Val-OMe and N-Boc-Val-COOH as nucleophiles.

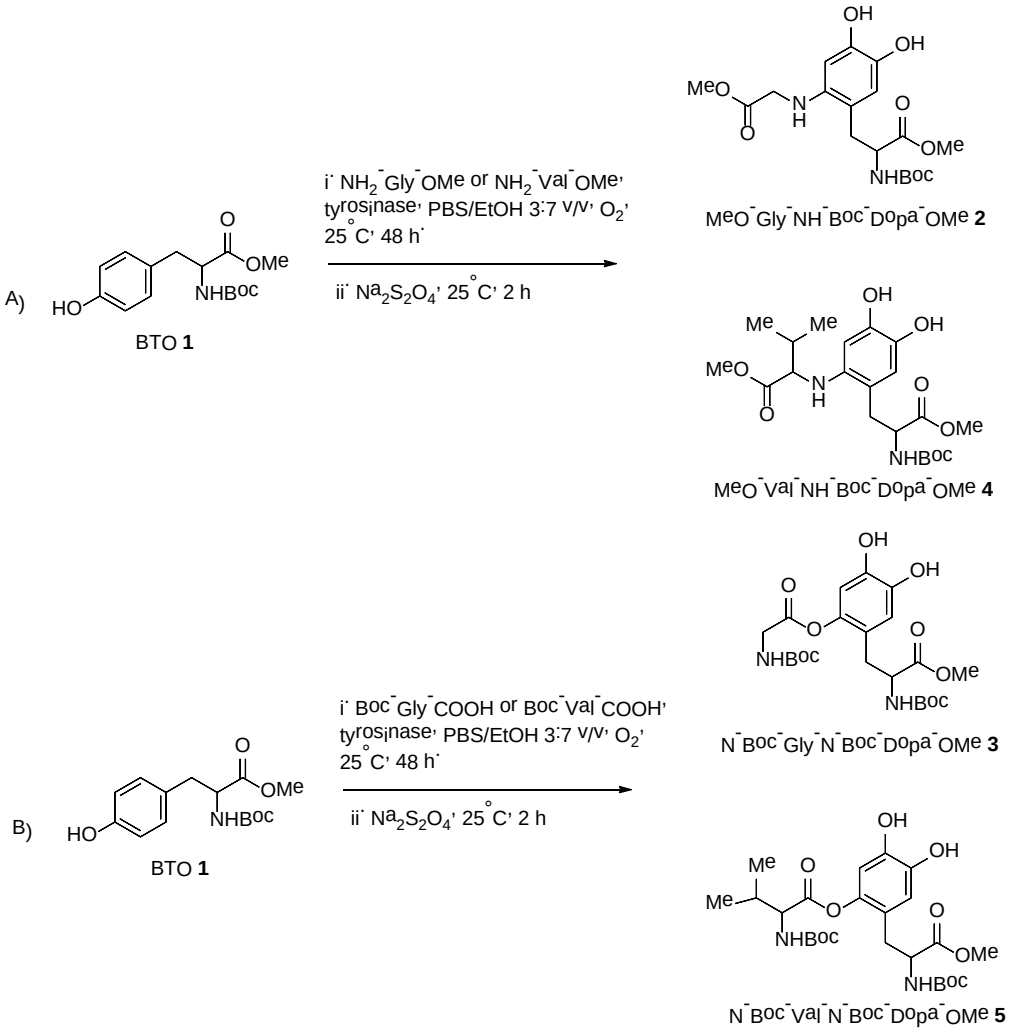

Figure 3.3. Synthesis of DOPA peptidomimetics **2-5** by oxidative functionalization of BTO **1** with tyrosinase from *Agaricus bisporus* in the presence of glycine and valine nucleophiles.

The corresponding DOPA peptidomimetics OMe-Val-N-Boc-DOPA-OMe **4** and N-Boc-Val-N-Boc-DOPA-OMe **5** were obtained in 77% and 74% yield, respectively (Table 12, entries 2 and 4), besides to residual BTO (Figure 3.3, pathways A and B). As a general trend, N-centred nucleophiles were slightly more efficient than the O-centred counterpart. Moreover, glycine nucleophiles were more reactive than valine nucleophiles, probably due to side-chain steric hindrance effects.

Table 16: Synthesis of O-C and N-C bonded DOPA peptidomimetics under homogeneous and heterogeneous conditions.

Entry	Nucleophile	Catalyst	product	Yield (%)
1	NH_2-Gly-OMe	tyrisonase[a]	OMe-Gly-N-Boc-DOPA-OMe **2**	87
2	N-Boc-Gly-COOH	tyrosinase	N-Boc-Gly-N-Boc-Dopa-OMe **3**	80
3	NH_2-Val-OMe	tyrosinase[a]	OMe-Val-N-Boc-Dopa-OMe **4**	77
4	N-Boc-Val-COOH	tyrosinase	N-Boc-Val-N-Boc-Dopa-OMe **5**	74
5	NH_2-Gly-OMe	Tyr/MWCNT[b]	OMe-Gly-N-Boc-DOPA-OMe **2**	85
6	N-Boc-Gly-COOH	Tyr/MWCNT	N-Boc-Gly-N-Boc-Dopa-OMe **3**	79
7	NH_2-Val-OMe	Tyr/MWCNT[b]	OMe-Val-N-Boc-Dopa-OMe **4**	75
8	N-Boc-Val-COOH	Tyr/MWCNT	N-Boc-Val-N-Boc-Dopa-OMe **5**	70
9	NH_2-Gly-OMe	Tyr/MWCNT[c]	OMe-Gly-N-Boc-DOPA-OMe **2**	88
10	NH_2-Gly-OMe	Tyr/MWCNT	OMe-Gly-N-Boc-DOPA-OMe **2**	85
11	NH_2-Gly-OMe	Tyr/MWCNT	OMe-Gly-N-Boc-DOPA-OMe **2**	85
12	NH_2-Gly-OMe	Tyr/MWCNT	OMe-Gly-N-Boc-DOPA-OMe **2**	83
13	NH_2-Gly-OMe	Tyr/MWCNT	OMe-Gly-N-Boc-DOPA-OMe **2**	81

[a] BTO **1** (20 mg, 0.068 mmol) was treated with tyrosinase from *Agaricus bisporus* (600 UA) and different α-amino acid residues (0.68 mmol) in PBS/EtOH (3:7 v/v; mL) at 25 °C for 24 h, followed by the reduction step with $Na_2S_2O_4$. [b] BTO **1** (20 mg, 0.068 mmol) was treated with Tyro/MWCNT (600 UA) and different α-amino acid residues in PBS/EtOH (3:7 v/v; 12mL) at 25 °C for 24 h, followed by the reduction step with $Na_2S_2O_4$. [c] Reusability is expressed as the yield in % of DOPA peptidomimetic **2** obtained by oxidation of BTO **1** with MWCTN/Tyr under optimal conditions.

Synthesis of DOPA peptidomimetics in heterogeneous conditions.

The oxidative functionalization of BTO **1** was then performed using tyrosinase supported on multi-walled carbon nanotubes (MWCNTs) applying the Layer by Layer (LbL) procedure previously developed[238]. Briefly, oxidized MWCNTs[116] were treated with a positively charged poly- (diallyldimethylammonium) chloride (PDDA) to facilitate the loading of tyrosinase, that is negatively charged at the operative pH 7. Bovine Serum Albumin (BSA) was used to reduce undesired conformational changes[243]. Glutaraldehyde (GA) increased the reticulation grade and the stability of the system (Figure 2)[244]. The structural characterization and the activity parameters of catalyst MWCNT/Tyrosinase/BSA (Tyr/MWCNTs), as well as its application in the synthesis of bioactive catechol derivatives are in reference[238]. The oxidation of BTO **1** (20 mg, 0.068 mmol) with Tyro/MWCNT (600 UA) in PBS/EtOH (7:3 v/v, 12 mL) at 25 °C for 24 h in the presence of NH_2-Gly-OMe or N-Boc-Gly-COOH (0.68 mmol) afforded compounds **2** and **3** in 85% and 79% yield, respectively (Table 12, entries 5 and 6). In a similar way, the oxidative functionalization of

BTO **1** (20 mg, 0.068 mmol) with NH_2-Val-OMe and Boc-Val-COOH (0.68 mmol) afforded compounds **4** and **5** in 75% and 70% yield, respectively (Table 12, entries 7 and 8).

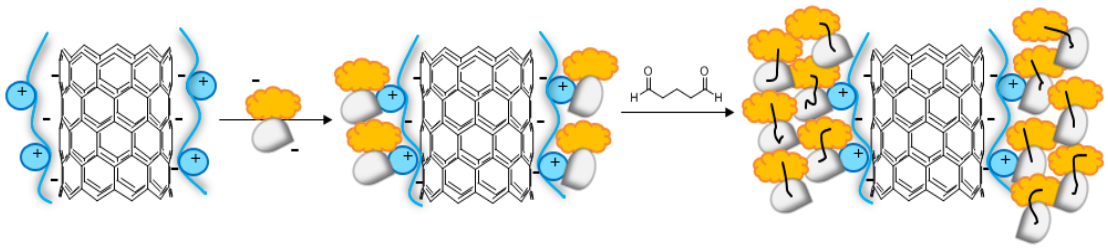

Figure 3.4. Loading of Tyrosinase (white) on oxidized MWCNTs coated with positively charged poly (diallyldimethylammonium) chloride PDDA (blue). Bovine Serum Albumin (BSA; orange) was used to reduce undesired tyrosinase conformational changes and glutaraldehyde (GA black lines) to increase the reticulation grade and the stability of the overall system.

Recycling experiments proceeded with success in the oxidation of compound BTO **1** with NH_2-Gly-OMe as selected nucleophile. As shown in Table 12 (entries 9-13), MWCNT/Tyr was used for at least five catalytic cycles with only a slight decrease of efficiency to give **2**.

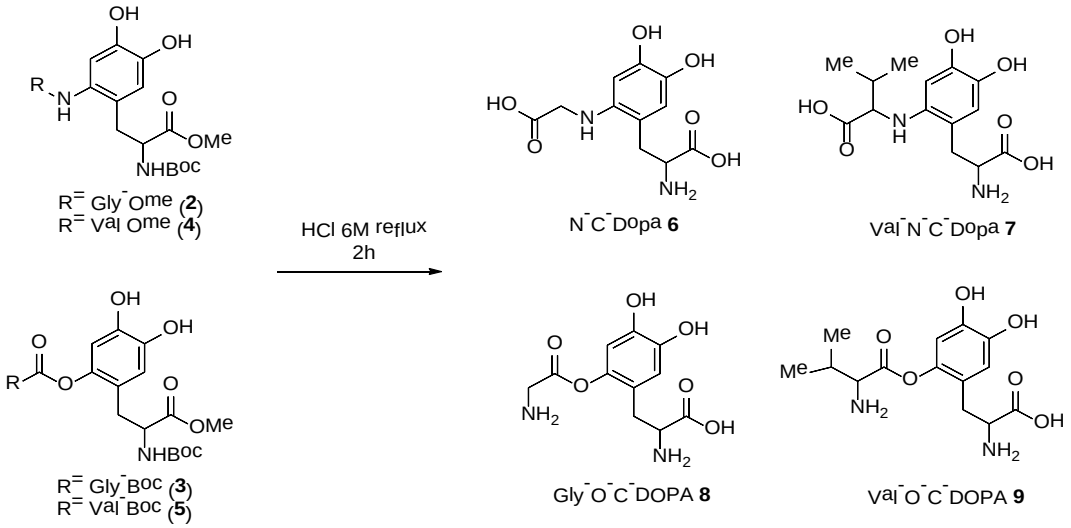

Figure 3.5 Deprotection of peptidomimetics **2-5** to afford Gly-N-C-Dopa **6**, Val-N-C-Dopa **7**, Gly-O-C-DOPA **8**, and Val-O-C-DOPA **9**.

Finally, DOPA peptidomimetics **2-5** were deprotected under standard conditions[245] using 6M hydrochloric acid heating at reflux for 2h. Gly-N-C-Dopa **6** and Val-N-C-Dopa **7** were obtained in quantitative yield, while Gly-O-C-DOPA **8** and Val-O-C-DOPA **9** were isolated in 73 % and 68 % yield respectively, probably due to the competitive hydrolysis of the novel C-O bond (Figure 3.5).

Evaluation of anti-Parkinson activity

Preliminary studies showed that DOPA peptidomimetics **2-5** were characterized by an antioxidant activity higher than that of the corresponding DOPA peptides[233]. On the basis of these data, we decided to evaluate the anti-PD effect of peptidomimetics **2-9** (protected and deprotected forms) on DAergic neurons. Since PD is characterized by low content of DA in the basal ganglia nuclei, potential anti-PD drugs should mimic the effects of DA and/or DOPA. Thus, the activity of DOPA peptidomimetics **2-9** was evaluated by measuring the effects on single neuron firing/membrane currents in comparison to those evoked by exogenous DA/DOPA applied to DAergic neurons of the rat substantia nigra pars compacta (SNpc)[245]. Simultaneous neuronal firing of a large population of neurons located in the SNpc was recorded by multi electrode array (MEA). Spontaneously active neurons were firstly challenged with DA (30 μM, 2 min, Figure 3.6) and only neurons that were inhibited by DA (>15% spontaneous firing inhibition); were considered in the present study. Similarly, the effect of the DOPA peptidomimetics 2-9 was evaluated in those DA sensitive neurons, which responded to drug perfusion with at least a 15% change in firing rate.

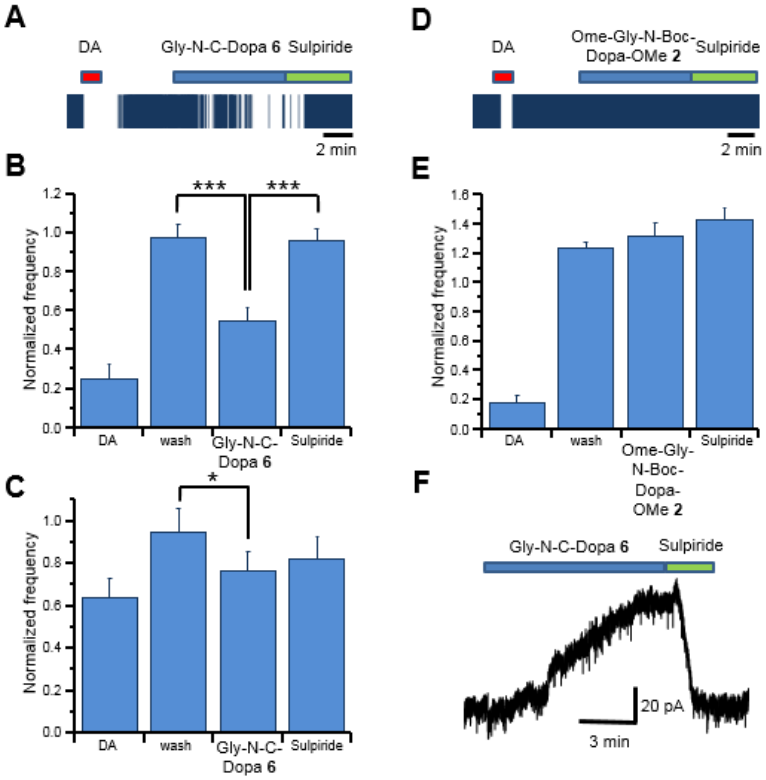

Figure 3.6 Acute effects of Gly-N-C-Dopa 6 on SNpc DA neurons. (A) Raster plot of the spontaneous firing recorded with MEA form a single SNpc DA neuron. DA (30 μM) robustly inhibited firing and, after complete washout of the DA effect, Gly-N-C-Dopa 6 (300 μM) caused a similar slow-onset inhibition of firing. Application of Sulpiride (10 μM) completely reversed Gly-N-C-Dopa 6 -mediated firing inhibition to control value. (B) Group data showing mean firing frequencies, normalized to control value, in 17 SNpc DA neurons during application of DA, washout, Gly-N-C-Dopa 6 and Sulpiride. Note that firing frequency returned to control values both after DA washout and in the presence of Sulpiride. (C) Group data showing mean firing frequencies, normalized to control value, during application of DA,

washout, Gly-N-C-Dopa 6 and Sulpiride, in 16 SNpc DA neurons poorly sensitive to DA. Similarly, to DA, also Gly-N-C-Dopa 6 exerted only a limited inhibition of firing. Sulpiride effect was minimal. (D) Raster plot of the spontaneous firing recorded with MEA form a single SNpc DA neuron. DA (30 μM) robustly inhibited firing and, after complete washout of the DA effect, the protected form OMe-Gly-N-Boc-DOPA-OMe 2 (300 μM) did not affect neuronal firing. No effect was also evident in Sulpiride (10 μM). (E) Group data showing mean firing frequencies, normalized to control value, in 40 SNpc DA neurons during application of DA, washout, OMe-Gly-N-Boc-DOPA-OMe 2 and Sulpiride. Note that no significant change of firing frequency was observed from DA washout. (F) Voltage clamp recording (Vh= -60 mV) from a single SNpc DA neuron showing Gly-N-C-Dopa 6 activated an outward current that was completely blocked by Sulpiride.

We recorded 39 neurons inhibited by DA, and in 24[246] of them the application of Gly-N-C-Dopa **6**, (300 μM) caused a slow onset firing inhibition that was completely reversed by the D2 receptor antagonist Sulpiride (10 μM; Figure 3.5, panels A and B). The extent of firing inhibition by Gly-N-C-Dopa 6 paralleled that of DA. Indeed, the effect of Gly-N-C-Dopa 6 was more pronounced (P = 0.00014; Figure 3.5, panel B) in those DA-sensitive neurons that were strongly inhibited by DA (74.66 ± 7.07%, N=17), compared to those (P = 0.041; Figure 3.5, panel C) inhibited by DA by a lesser extent (35.96 ± 9.03%, N=16). In 6 out of the 39 SNpc DA neurons, Gly-N-C-Dopa 6 (300 μM) did not cause firing inhibition (< 15%), although they responded to DA with 26.73 ± 10.88% firing inhibition (data not shown). To further investigate the neuronal response to Gly-N-C-Dopa **6** we performed voltage clamp experiments from single DA neurons. We found that application of Gly-N-C-Dopa **6** activated a slowly developing outward current of about 60 pA in 1 out of 3 DAergic neurons tested (Figure 3.5, panel F). This current was completely blocked by the D2 receptor antagonist Sulpiride. In the remaining 2 neurons Gly-N-C-Dopa 6 was ineffective. By contrast, the protected form OMe-Gly-N-Boc-DOPA-OMe **2** (300 μM) did not cause significant modifications of firing activity of DAergic neurons (N = 40, P = 0.36744; Figure 3.5 D, E). These data suggested that the deprotection of **2** was a key step for the appearance of DA-like effects in the subpopulation of DAergic neurons. Since Gly-N-C-Dopa 6 cannot release DA due to the stable N-C linkage between the amino acid residues, the observed activity could be explained by the direct interaction with D2 receptors in the extracellular environment.

Has been tested the DA/DOPA-like effects of OMe-Val-N-Boc-Dopa-OMe **4** and Val-N-C-Dopa **7**, respectively. We recorded 15 SNpc neurons inhibited by DA, and in 12 of these neurons the application of Val-N-C-Dopa **7** (300 μM) caused a pronounced (P = 0.000001) firing inhibition. This inhibition was completely reversed by the D2 receptor antagonist Sulpiride (10 μM; Figure 3.7, panels A and B). In these experiments, 3 out of 15 DAergic neurons were insensitive to Val-N-C-Dopa **7**, (300 μM; < 15%) despite they displayed an inhibition by DA of 84.34 ± 0.79% (data not shown). In a large set of population (53 out of 62) of SNpc neurons inhibited by DA OMe-Val-N-Boc-Dopa-OMe **4** (300 μM) caused marked firing inhibition (Figure 3.7, panels C and D),

however, differently from Val-N-C-Dopa **7**, the cellular inhibition seemed to be unspecific, as it was not reversed by Sulpiride.

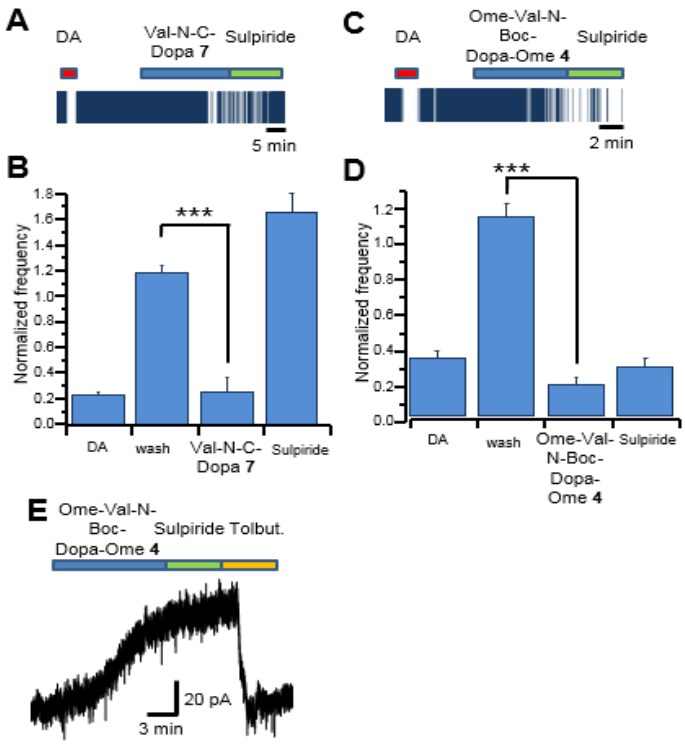

Figure 3.7. Acute effect of Val-N-C-Dopa **7** and OMe-Val-N-Boc-Dopa-OMe **4** on rat SNpc DAergic neurons. (A) Raster plot of the spontaneous firing recorded with MEA. DA (30 μM) strongly inhibited firing and, after complete washout, the deprotected form of Val-N-C-Dopa **7** (300 μM) caused a slow-onset inhibition of firing, which was reversed by Sulpiride (10 μM). (B) Group data showing mean firing frequencies in the presence of DA, washout, deprotected Val-N-C-Dopa **7** and Sulpiride, in 12 SNpc DA neurons. (C) Raster plot of the spontaneous firing recorded with MEA. DA (30 μM) strongly inhibited firing and, after complete washout, OMe-Val-N-Boc-Dopa-OMe **4** (300 μM) caused a slow-onset inhibition of firing. However, application of Sulpiride (10 μM) did not reverse OMe-Val-N-Boc-Dopa-OMe **4** effect. (D) Group data showing mean firing frequencies in the presence of DA, washout, L-DOPA Val Ome and Sulpiride, in 53 SNpc DA neurons. (E) Patch clamp recording of membrane current (Vh=- 60 mV) of a single SNpc DA neuron. Application of OMe-Val-N-Boc-Dopa-OMe **4** (300 μM) activated an outward current that was insensitive to Sulpiride and fully blocked by Tolbutamide (100 μM).

These results were further confirmed by patch-clamp recordings. In the example trace of Figure 3.7 (panel E), OMe-Val-N-Boc-Dopa-OMe 4 caused an outward current that was insensitive to Sulpiride. By contrast, the outward current was completely blocked by the KATP channel blocker Tolbutamide (100 μM). These data suggested that OMe-Val-N-Boc-Dopa-OMe **4** caused firing inhibition through a mechanism other than D2 receptor stimulation, possibly involving a drop in intracellular ATP content, which causes KATP channel opening. In alternative, the direct action on KATP channels in SNpc DAergic neurons cannot be completely ruled out.

In 9 out of the 62 SNpc DAergic neurons OMe-Val-N-Boc-Dopa-OMe 4 (300 μM) did not cause firing inhibition (< 15%), although they responded to DA with 85.78 ± 6.49% firing inhibition

(data not shown). Note that O-C peptidomimetics **3**, **5**, **8** and **9**, were not active under the same experimental conditions, suggesting a structure activity relationship between the inhibition of neuronal firing and evoked outward currents of DAergic neurons and the type of covalent bond. Future experiments will address the possible mechanisms underlying Gly-N-C-Dopa **6** and Val-N-C-Dopa **7** mediated activation of D2 receptors, and their ability to enter DAergic neurons.

3.2 Preparation of wrapped carbon nanotubes poly(4-vinylpyridine)/MTO based heterogeneous catalysts for the oxidative desulfurization (ODS) of model and synthetic diesel fuel

3.2.1 Aim of work

The removal of sulfur compounds in fuel is an important tool for the environmental protection[247] since the combustion process produces SO_x derivatives that affect the stability of the atmospheric ozone layer, increasing the formation of acid rains[248] Therefore, the sulfur content in diesel fuel is limited by U.S. Environmental Protection Agency (EPA) and Euro V standard protocols[249]. Hydrodesulfurization (HDS) is the conventional procedure for the removal of sulfur derivatives in fuel[250] by hydrogenolysis at both high temperature (300 to 400 °C) and pressure (10-130 atm)[251]. However, HDS achieves limited performances in the removal of recalcitrant aromatic compounds, such as benzothiophene (BT), dibenzothiophene (DBT) and their derivatives, which can irreversibly inactivate the catalyst, influencing the kinetic and the performance of the reactors[252]. The oxidative desulfurization (ODS) is a promising alternative to HDS[253]. In the ODS process, BT and DBT derivatives are oxidized to corresponding sulfones and sulfoxides under low temperature and pressure conditions, followed by extraction or adsorption processes with polar phases[254] The oxidation of BT and DBT derivatives in the ODS process is usually performed by stoichiometric oxidants, such as sodium bromate ($NaBrO_3$)[255], potassium permanganate ($KMnO_4$)[256], carboxylic and sulfonic peracids[257]nitric acid (HNO_3), *tert*-butyl-hydroperoxide (TBHP)[258] superoxides[259] and ozone[260]. Among the stoichiometric reagents, hydrogen peroxide (H_2O_2) is frequently applied due to its environmental benign properties[261]. In a previous study, we described the activation of H_2O_2 in the oxidation of BT and DBT derivatives with poly(4-vinylpyridine)/methyltrioxorhenium (CH_3ReO_3, MTO) adducts as heterogeneous catalysts[262]. In these reactions, MTO forms mono-peroxorhenium [$MeRe(O)_2(O_2)$] and bis-peroxorhenium [$MeRe(O)(O_2)_2$] complexes[263], which can transfer the oxygen atom to sulfur substrates[264]. The heterogeneous catalysis is of relevance in ODS processes, since it reduces the leaching of active species and favors the recovery and reuse of the catalyst for successive transformations[265]. In the last years, multiwalled carbon nanotubes (CNTs) have been used to design novel and

efficient nanostructured heterogeneous catalysts[266]. CNTs are quasi one-dimensional materials (lengths range from less than 100 nm to several centimetres, and diameters of typically 0.8 to 2 nm and 5 to 20 nm), and show unique electronic, mechanical and structural properties[119]. They are chemically stable with high surface to volume ratio, and undergo chemical functionalization for the preparation of catalysts with specific and carefully tuned properties. The combination of CNTs with titanium species[267] polyhetero acids (Cs 2.5 H0.5 $PW_{12}O_{40}$)[268] manganese oxides and palladium derivatives, has been reported in ODS model processes, with different degree of success depending on the specific experimental conditions. Recently, we described the use of CNTs as anchoring supports for different oxidative enzymes[188]. Here, we describe the preparation of a novel family of MTO heterogeneous catalysts based on either, the immobilization of preformed poly(vinyl-4-pyridine)/MTO [PVP/MTO] or poly(vinyl-4-pyridine-*N*-oxide)/MTO [PVPN/MTO] adducts on pristine CNTs, or the direct loading of MTO on previously wrapped CNTs with PVP and PVPN resins. The novel catalysts were successfully used for the activation of H_2O_2 in the oxidation of BT and DBT derivatives, and in the treatment of model fuel oil (MF) and synthetic diesel fuel (SDF) as representative systems for the ODS process.

3.2.2 Experimental part

Materials

Methyltrioxorhenium (MTO), H_2O_2 (35% w/w, aqueous solution), poly(4-vinyl pyridine) PVP-2% cross-linked with divinylbenzene, 3-methyl-thiophene (3-MeT), 2-methyl-benzothiophene (2MeBT), 3-methyl-benzothiophene (3MeBT), dibenzothiophene (DBT), 4,6-dimethyl-dibenzothiophene (DMDBT), and CNTs (D = 110-170 nm; L = 5-9 μm) were obtained from a commercial source (Aldrich). All commercial products and solvents (CH_2Cl_2, *n*-octane, CH_3CN) were of the highest grade available. The diesel fuel sample was obtained from an italian commercial source, having a density of 0.713 g/mL, 0.34% w/w of total sulfur, 73 ppm of total nitrogen (N), and 18% w/w of total aromatic fractions. The reaction mixtures were analyzed by a Hewlett Packard 6890 series gas chromatograph equipped with a FID, using a 30 m x 0.32 mm x 0.25 mm film thickness (cross-linked 5% phenylmethylsiloxane) column, and helium as carrier gas. The identification of the peaks by gas-chromatography mass-spectrometry (GC–MS) has been performed by means of a Varian 2000 GC–MS instrument. Yields

and conversions have been quantified using *n*-hexadecane as internal standard or, when necessary, after flash-chromatographic purification (silica gel, 230–400 mesh). Product yields were calculated on the basis of the substrate conversion. ^{1}H and ^{13}C NMR spectra were recorded on a Bruker AC 400 MHz spectrometer. Inductively coupled plasma mass spectrometry (ICP-MS) analyses were performed on Agilent 7500a model ICP mass spectrometer.

*Preparation of catalyst CNT/MTO **I***

CNTs (10 mg) were suspended in EtOAc (10 mL) and treated in ultrasonicator apparatus for 30 min. MTO was added to the suspension of CNTs in EtOAc (1:1, 1:2 and 1:5 CNTs/MTO w/w ratio) at 25°C for different times (30, 60, and 2 h) under magnetic stirring. At the end, the catalyst CNT/MTO **I** was recovered by centrifugation (12.000 rpm), washed with a low amount of EtOAc (2.0 mL) and dried. The washing solvent was stored in order to evaluate the loading factor (LF). The highest LF was obtained for CNT/MTO 1:2 w/w ratio, after 2h.

*Preparation of catalysts CNT/[PVP·MTO] **II** and CNT/[PVPN·MTO] **III***

The PVP/MTO and PVPN/MTO adducts were prepared as previously reported[262]. Briefly, the appropriate resin (80 mg) was suspended in EtOH (2 mL), and treated with freshly prepared MTO (20 mg, 0.08 mmol) under magnetic stirring for 1 h at 25°C. At the end, the mixture was filtered and washed with EtOH (2.0 mL) to yield the desired adducts. The wrapping of preformed PVP/MTO and PVPN/MTO adducts on CNT was performed by grinding the mixture in agate mortar (CNT/adduct 1:3 w/w) for 20 min at 25 °C. At the end, the material was suspended in EtOAc (5.0 mL) and catalysts CNT/[PVP·MTO] **II** and CNT/[PVPN·MTO] **III** were recovered by centrifugation (12.000 rpm), washed with a low amount of EtOAc (2.0 mL) and dried. The washing solvent was stored in order to evaluate the LF.

*Preparation of catalysts CNTw/MTO **IV** and CNTw'/MTO **V***

The wrapping by grinding of CNTs with poly(4-vinyl pyridine) (CNTw) or poly(4-vinyl pyridine *N*-oxide) (CNTw') 2% cross-linked with divinylbenzene resins was performed by a slightly modification of previously reported procedures [27a]. Briefly, CNT were grinded in agate mortar with the appropriate resin (1:3 w/w CNT/resin) for 20 min at 25 °C. At the end, the material was suspended in EtOAc (5.0 mL) and the support

was recovered by centrifugation (12.000 rpm). Next, the grinded supports (5 mg) were suspended in EtOAc (5.0 mL) and treated with MTO (1:2 w/w) under magnetic stirring at 25°C for 2 h. The novel catalysts *CNTw/MTO* **IV** and *CNTw'/MTO* **V** were recovered by centrifugation (12.000 rpm), washed with a low amount of EtOAc (2.0 mL) and dried. The washing solvent was stored in order to evaluate the LF.

Determination of the loading factor

The loading factor (LF; defined as mmol of MTO immobilized per gram of support) was measured by ^{1}H NMR titration, and by inductively coupled plasma mass spectrometry (ICP-MS) analysis. In the ^{1}H NMR analysis, the LF was calculated on the basis of the residual amount of MTO in washing solutions. Briefly, after evaporation, the crude was dissolved in $CDCl_3$ (0.7 mL) in the presence of *n*-octane (0.5 mmol) as internal standard. The amount of MTO was evaluated by quantitative integration of the characteristic Re-Me peak at 2.6 ppm. In the case of ICP-MS analysis, the concentrations of Re were measured by constructing the calibration curve at 5-point in the range 0-50 ppb, and were reported in % by weight with respect to the original sample (see 2.3.4 paragraph).

Scan electron microscopy (SEM) and Transmission electron microscopy (TEM) analyses

The morphology of catalysts **I-V** was studied by SEM and TEM analyses. For the SEM, the samples were dispersed in milliQ water, sonicated for 5 min at room temperature, and a drop of each solution was taken and deposited onto silicon substrates (Si). At the end, the samples were subjected to annealing at 50 °C to quickly evaporate the solvent (water). Samples were analyzed by Zeiss, LEO 1530 apparatus, equipped with a field emission electron gun. In TEM analysis, droplets of sample suspensions (10 µl) were placed on formvar-carbon coated grids and allowed to adsorb for 60 sec. Excess liquid was removed gently touching the filter paper. The adsorbed specimen was then processed for negative-staining, by washing the specimen grid on a drop of negative stain (2% uranyl acetate in distilled water), blotting and repeating this step once more, this time leaving the specimen grid for 60 sec on a new drop of negative stain solution. Samples were observed at a JEOL 1200 EX II electron microscope. Micrographs were acquired by the Olympus SIS VELETA CCD camera equipped with the iTEM software.

X-ray photoelectron spectroscopy (XPS)

The chemical state of the different elements of catalysts **II-V** was analysed using a X-ray photoelectron spectroscopy (XPS) system (PHI 1257), equipped with a hemispherical analyser. The X-ray was generated by a non-monochromatized Mg source (hν = 1253.6 eV), and the measurement was performed at ultrahigh vacuum (about 2×10^{-9} Torr). All the reported binding energy (BE) data have been calibrated using the carbon sp^2 bond of the CNTs, positioned at BE of 284.8 eV. Moreover, XPS can also provide information of the chemical environment of the surface elements according to peak-fitting of X-ray photoelectron spectral envelopes, based on the fact that the BE of the photoelectron is not only determined by the element itself but also influenced by the chemical environment. Therefore, the analysis of XPS data was performed using the XPS Peak Fitting Programme version 4.1. The C 1s, N 1s, O 1s, and Re 4f photoemission peaks were detected and analysed (not shown here).

*ICP-MS analyses of catalyst **I**-**V***

About 4 mg of samples were mineralized in opened fluorinated ethylene propylene (FEP) vials on a heating block at 148 °C. Samples were treated with 0.5 mL of 70% HNO_3 at 148 °C to incipient dryness; 2.0 mL of deionized water (from a Milli-Q system) were then added. The obtained solution was centrifuged at 2500 rpm for 4 minutes, in order to separate it from the solid residue, collected and diluted with deionized water to have Re concentration in the ng/g range before ICP-MS measurements. A second extraction, using the same procedure, has been performed on the solid residue of each vial. A 10^{-3} g/g certified standard rhenium solution (AccuStandard Lot Number B4065078) was used to calibrate the instrumentation. The relative uncertainties in rhenium concentration, given with one standard deviation, are in the order of 5%. The Re extraction efficiency [%] of the adopted procedure was calculated based on the measurement of the two solutions obtained for each sample.

*Oxidation of thiophene derivatives **1**-**5**. General procedure.*

Dibenzothiophene (DBT) **1**, 4,6-dimethyl-dibenzothiophene (DMDBT) **2**, 2-methyl-benzothiophene (2-MeBT) **3**, 3-methyl-benzothiophene (3-MeBT) **4**, and 3-methyl thiophene **5** (3-MeT), were oxidized as representative aromatic sulfur compounds in fuel oil. Initially, DBT **1** was treated with catalysts **I-V** and H_2O_2 in CH_2Cl_2 or *n*-octane.

Briefly, the appropriate catalyst (3% w/w of MTO with respect to substrate) was added to **1** (0.1 mmol) in CH_2Cl_2 or *n*-octane (2.0 mL), followed by treatment with H_2O_2 (4.0 equivalents, 35% water solution), under magnetic stirring at 60°C for 24 h. The progress of the oxidation was monitored by GC–MS analysis of periodically withdrawn samples (2.0 μL of sample were taken out the reaction solution). The catalyst was recovered by filtration and MnO_2 (1.0 mg) was added under stirring at 25°C to eliminate the excess of H_2O_2 (the reaction mixture was found to be unchanged after the MnO_2 treatment). The organic solvent was dried on Na_2SO_4, filtered and evaporated under reduced pressure. Next, the oxidation of compounds **1**-**5** with catalysts **I**-**V** was repeated under similar experimental conditions using *n*-octane/CH_3CN mixture in three different ratio (1:1, 2:1 and 3:1 v/v ratio), to evaluate the optimal amount of the co-solvent. At the end of the oxidation, the catalyst was removed by centrifugation (12.000 rpm), the *n*-octane and CH_3CN phases were separated, dried and analysed by GC-MS in the presence of acetophenone as internal standard. As expected, sulfone derivatives were detected in the polar CH_3CN phase. When necessary, crude sulfone derivatives were obtained by distillation under reduced pressure of the *n*-octane and CH_3CN phases, and the recovered organic phases were used for further transformations.

Catalyst recycling and leaching experiments

Recycling experiments with catalyst **V**, as a selected representative sample, were performed for the oxidation of either DBT **1** alone or MF, in the optimal *n*-octane/CH_3CN mixture (3:1 v/v) for **1**, or MF/CH_3CN (3:1 v/v) for MF. After the first run, the catalyst was recovered by filtration, washed with *n*-hexane and dried under vacuum for 1 h. More runs were performed, working under optimized experimental conditions. To evaluate the presence of a real heterogeneous catalytic activity, the organic layer obtained after any recycle was analyzed by ^{1}H NMR analysis, as previously reported for the determination of the loading factor (LF). The absence of the characteristic ^{1}H NMR Re-Me peak at 2.6 ppm, even after the last recycling run, suggested that MTO was not released in the reaction medium, thus working as purely heterogeneous system. These data were further confirmed by the lack of catalytic activity for the recovered organic solution.

Preparation and oxidation of model fuel (MF) and synthetic diesel fuel (SDF) samples

The model fuel (MF) sample was prepared by adding equimolar amounts (in the range of 0.01–0.03 mmol) of each substrate **1**–**5** into *n*-octane (from 1.5 to 2.0 mL), in order to

obtain a total sulfur concentration of 2.8 mg/mL, which is indicative of a real sample. In a similar way, equimolar amounts (0.02 mmol) of each substrate **1**–**5** were added to an authentic sample of diesel fuel (SDF, 1.5 mL) to gain a total sulphur concentration of 3.8 mg/mL. The MF and SDF samples were oxidized with the most reactive catalyst **V**, under previously optimized experimental conditions. In particular, MF or SDF samples added with one third of acetonitrile (with respect to their original volume) were treated with catalyst **V** (3% w/w of MTO with respect to total substrate) and H_2O_2 (4.0 equiv., added in two steps to reduce thermal decomposition; 8.0 equiv. in the case of SDF), under magnetic stirring at 60 °C. The reaction progress was monitored by GC–MS analyses of periodically withdrawn samples (0.1 mL samples were taken out the reaction solution), until the substrate was entirely consumed. At the end of the oxidation, the catalyst was removed by centrifugation (12.000 rpm), the *n*-octane (or diesel fraction) and CH_3CN phases were separated, dried and analysed by GC-MS in the presence of acetophenone as internal standard. The sulfone derivatives were detected in the polar CH_3CN phase.

3.2.2 Results and discussions

*3.1 Preparation of catalysts **I-V***

Three novel types of MTO heterogeneous catalysts were prepared starting from commercially available carbon nanotubes (CNTs). CNTs are excellent supports for immobilization of active organometallic compounds, since they offer a high surface area for loading, as well as biocompatibility and mechanical resistance[271]. Initially, MTO was loaded on CNTs through physical adsorption by noncovalent interactions[272]. In particular, MTO was added to a suspension of CNTs in EtOAc (1:1, 1:2 and 1:5 CNT/MTO w/w ratio) under magnetic stirring at 25°C for 2 h. CNT/MTO **I** was recovered by centrifugation, washed and used without any further purification (Figure 3.8, pathway A). The loading factor (LF) of catalyst **I** (defined as mmol of MTO per gram of support) was measured by ^{1}H NMR titration of the residual MTO in washing solutions, and in alternative, by inductively coupled plasma mass spectrometry (ICP-MS) analysis of the final product. Irrespective to experimental conditions, low values of LF were obtained (Table 17, entry 1), suggesting the ineffectiveness of the simple physical adsorption of MTO on CNTs. CNTs and poly(4-vinylpyridine) (PVP) undergo metal-induced self-aggregation processes to form tight stable bundles in which metal ions can be trapped by coordination with the pyridinyl moiety[273]. On the basis of these data, we evaluated the

possibility to load two preformed MTO adducts, namely poly(4-vinylpyridine)/MTO [PVP·MTO] and poly(4-vinylpyridine)*N*-oxide/MTO [PVPN·MTO] on CNTs. The adducts were prepared as previously reported by us[274], and added to a suspension of CNTs in EtOAc [2:1 w/w, (resin·MTO)/CNT ratio] under magnetic stirring at 25°C for 2 h, to yield catalysts CNT/[PVP·MTO] **II** and CNT/[PVPN·MTO] **III** (Figure 3.8, pathway B). LFs and immobilization yields of catalysts **II** and **III** were in the range of 0.33-0.36, and 16.6-17.9%, respectively (Table 17, entries 2 and 3).

Table 17. Loading factors and immobilization yields of catalysts **I**-**V**.

Entry	Sample	Loading factor[a]	Immobilization yield[b] (%)
1	Cat **I**	0.01[c] (n.d.)[d]	0.4[d]
2	Cat **II**	0.33 (0.31)	16.6
3	Cat **III**	0.36 (0.32)	17.9
4	Cat **IV**	0.47 (0.42)	24
5	Cat **V**	1.43 (1.40)	71.6

[a] mmol of catalyst (MTO) per gr of support (MWCNTs). [b] Immobilization yield is defined as supported MTO with respect to total MTO. [c]Value calculated by ICP-MS analysis. [d]Value calculated by ^{1}H NMR analysis.

Finally, we applied the wrapping procedure. The wrapping procedure in solid state[275] is the simplest alternative to physical adsorption for the functionalization of CNTs. For example, the wrapping of PVP on CNTs successfully separates single walled carbon nanotubes from the ropes they formed because of intra-strand van der Walls attractive interactions. Moreover, CNTs wrapped PVP systems show highly modified solubility properties[276]. As a general procedure, PVP (or PVPN) and CNTs (2:1 w/w ratio) were grinded in an agate mortar for 1 h at 25°C to afford the desired PVP/CNT and PVPN/CNT composite supports[277] About the efficacy of the deposition, previously reported thermogravimetric analysis (TGA) of PVP/CNT showed the presence of c.a. 0.04 mmol of PVP per mg of aggregate[273]. Successively, PVP/CNT and PVPN/CNT were dispersed in EtOAc (2.0 mL) and loaded with MTO (support:MTO ratio 1:2 w/w) under magnetic stirring for 2 h at 25°C, to yield CNT_w/MTO **IV** (CNT_w=PVP/CNT) and CNT_w'/MTO **V** (CNT_w'=PVPN/CNT), respectively (Figure 3.8, pathway C). Catalyst **IV** and **V** showed values of LF and immobilization yield higher than **II** and **III** (Table 17, entries 4-5 versus entries 2-3), confirming the efficacy of the wrapping procedure for the deposition of MTO on CNTs.

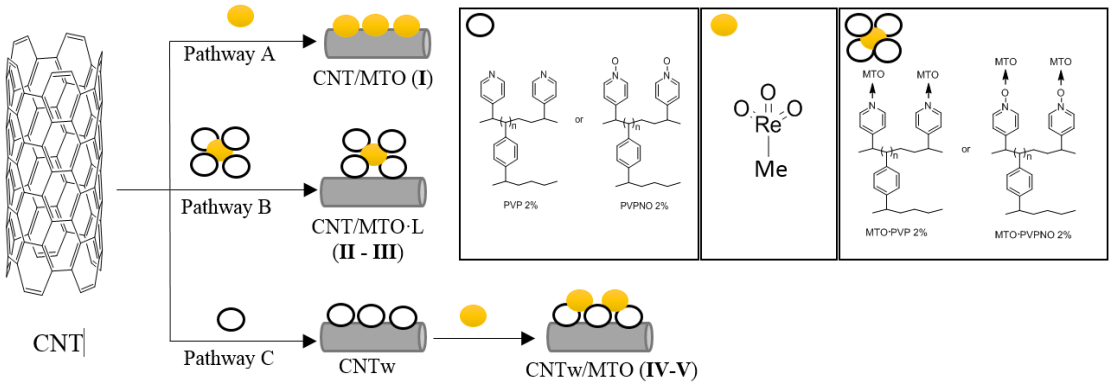

Figure 3.8. Preparation of catalysts CNT/MTO **I**, CNT/MTO·L **II-III**, and CNTw/MTO **IV-V**

*Morphological characterization of catalysts **II-V***

Figures 3.9-3.13 show a set of scanning electron microscopy (SEM) and transmission electron microscopy (TEM) photographs of catalysts **II-V**. Figure 3.9 reports the SEM image of the commercially available CNTs used in the preparation of catalysts **I-V**. CNTs are rigid rods, with a perfectly smooth surface and different diameter depending on the number of the graphitic cylinders involved[278].

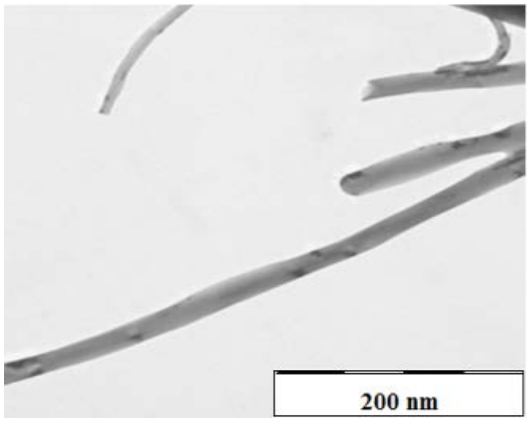

Figure 3.9. SEM image of pristine CNTs.

SEM and TEM photographs of catalyst **II** showed a quite different morphology (Figure 3.10). The organic resin clearly covers CNTs in the SEM image, yielding objects of fusiform shapes and diameter of average size of the order of 200 nm (Figure 3.10, panel A). TEM confirms the coating, the fusiform CNTs black core being homogeneously covered along its extension (Figure 3.10, Panel B). At a largest magnification (Figure 3.10, panel C), small protrusions emerging from the surface are visible.

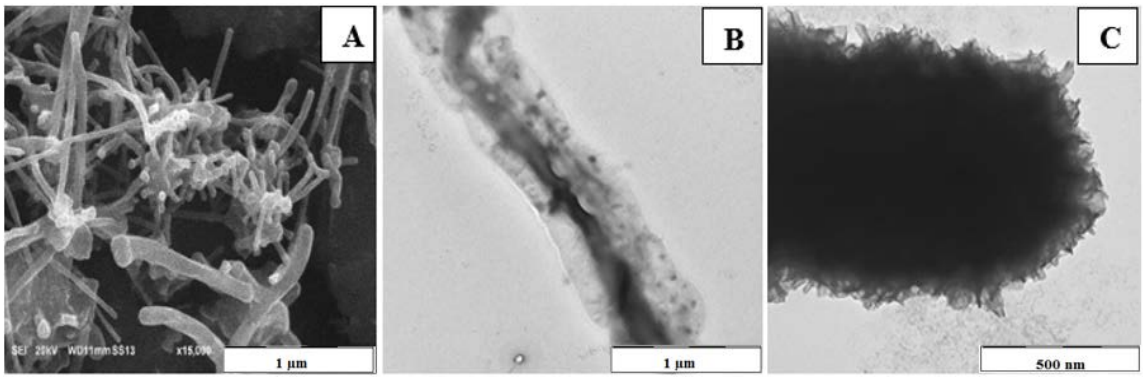

Figure 3.10. Panel A: SEM image of catalyst **II**. Panels B and C: TEM images of catalyst **II**.

The morphology of catalyst **III**, is similar to that of catalyst **II**. Again, CNTs are completely covered by the organic resin (Figure 3.11, panel A), that appears as a continuous layer in the TEM image (Figure 3.11, panel B).

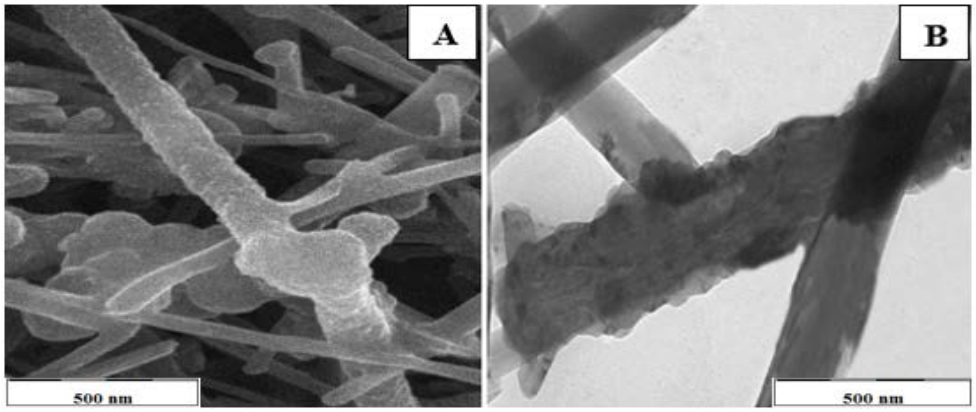

Figure 3.11 SEM image (Panel A) and TEM image (Panel B) of catalyst **III**.

The wrapping procedure afforded objects with a more organized surface structure. The SEM image of catalyst **IV** shows coated CNTs with small and well-defined protrusions of regular shape, arranged on the surface (Figure 3.12, panel A). Protrusions are clearly visible as polygonal-like small grumes in TEM (Figure 3.12, panel B). The scaffold was characterized by an average size of the order of 200-300 nm, similar to that of catalyst **II**.

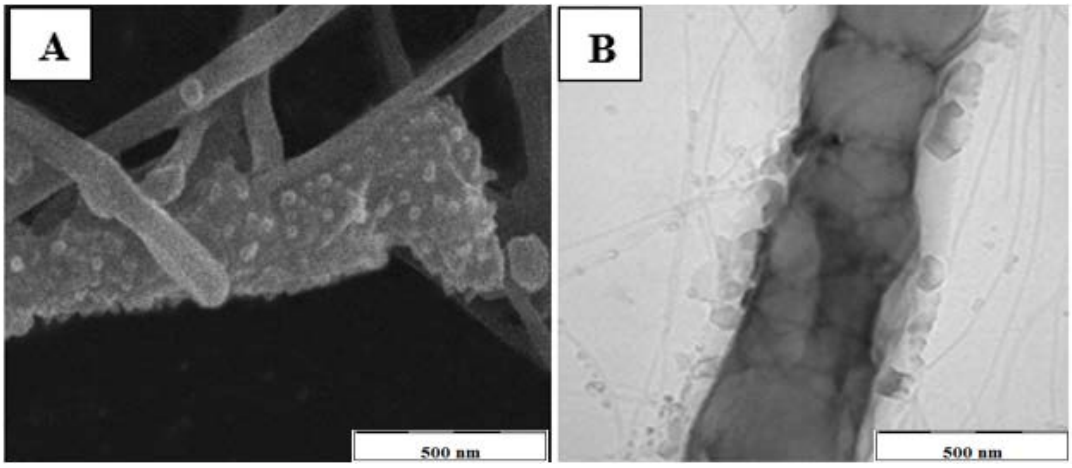

Figure 3.12 Panel A: SEM image of catalyst **IV** with an organized and regular surface structure. Panel B: TEM image of catalyst **IV** showing protrusions as polygonal-like small grumes.

Catalyst **V** showed a behavior similar to **IV**, again characterized by well-defined protrusions on the surface (Figure 3.13, panels A and B). The presence of regular aggregates after the wrapping procedure is in accordance with the known supramolecular self-assembling properties of PVP resins, which are able to generate highly organized structures by non-covalent (van der Waals, induced dipoles, etc.) and π-interactions.

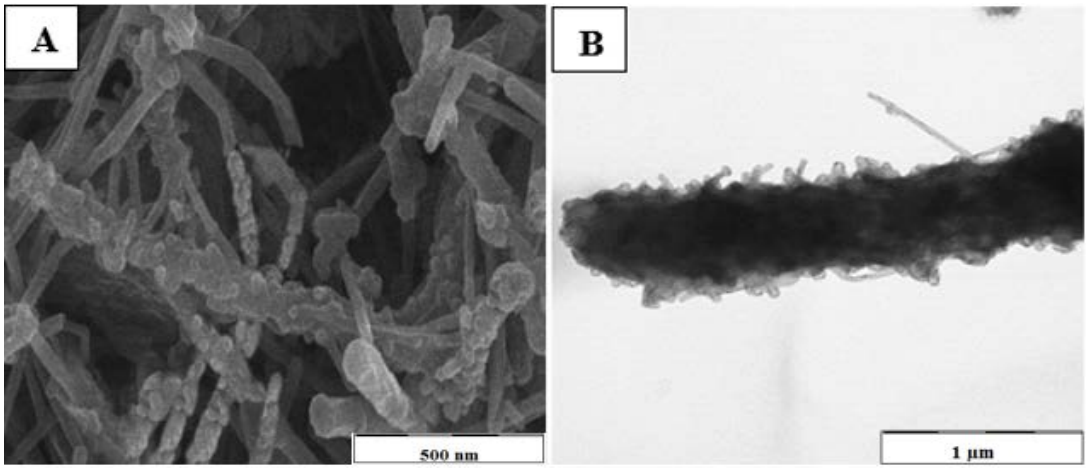

Figure 3.13 Panel A and B: SEM and TEM images of catalyst **V**, respectively.

XPS analysis

Table 18 reports the XPS binding energies (BEs) of catalysts **II-V**, obtained through the fitting procedure of the N 1s and Re 4f peaks. The Re 4f region showed two different double peaks, corresponding to $4f_{7/2}$ and $4f_{5/2}$ levels, with a spin orbit splitting of 2.4 eV. The BEs peaks at 46.4, 44.1-44.5 and 44.8-45.0 eV were assigned as Re $4f_{7/2}$ level for Re^{7+}, $Re^{5+/4+}$, and Re^{6+} species, respectively. In addition, the band of the pyridine-*N*-oxide fragment was detected at about 403 eV[280]. The presence of different oxidation state for

rhenium suggests the occurrence of redox processes during the immobilization of MTO on the resins. An analogous behavior was previously observed in the XPS analysis of polyaniline/MTO complexes[281]. In the case of catalysts **III** and **V,** the higher values of BEs peaks positions of Re 4f level (44.8 and 45.0 eV, respectively, assigned to a Re^{6+} oxidation state) with respect to **II** and **IV**, indicates that the redox process is less relevant for the PVPN resin. The N 1s peak (at around 401 eV) in catalysts **II-V**, due to a charge transfer from pyridine moiety to rhenium center, definitively confirms the coordination of rhenium, irrespective to the immobilization procedure.

Table 18. Selected Binding Energies (BEs) by XPS analysis on catalysts **II-V** and relative assignments[a]

Element	II	III	IV	V	Assignments
N *1s*	398.8	399.3	399.3	399.2	Pyridine[b]
	401.0	401.1	400.9	401.2	Re-pyr interactions
	-	403.0	-	402.8	Pyridine-*N*-oxide[b]
Re $4f_{7/2}$	44.1[c]	44.8[d]	44.5[c]	45.0[d]	$Re^{6+/5+/4+}$
	46.4	46.4	46.4	46.4	Re^{7+}

[a]BEs measured in eV units. [b]See Table 5 on reference [35d]. [c]Tentatively assigned to $Re^{5+/4+}$. [d]Tentatively assigned to Re^{6+}.

Oxidation of thiophene, BT and DBT derivatives

In ODS model processes, the oxidation is usually performed in organic solvents with a low value of dielectric constant, since they show a polarity similar to original fuel diesel. With the aim to evaluate the efficacy of catalysts **I-V**, we initially studied the oxidation of DBT **1** in CH_2Cl_2 and *n*-octane, under the experimental conditions previously applied by us with the simple PVP/MTO and PVPN/MTO adducts[262]. Briefly, the reaction was performed in the presence of the appropriate catalyst (3% w/w of MTO with respect to substrate, based on LF) by addition of a small excess of H_2O_2 (4.0 equiv) in two steps (to reduce thermal decomposition) at 25°C (CH_2Cl_2) or 60°C (*n*-octane)[282].

Figure 3.14. Catalytic Oxidation of model aromatic sulfur derivatives **1-5**.

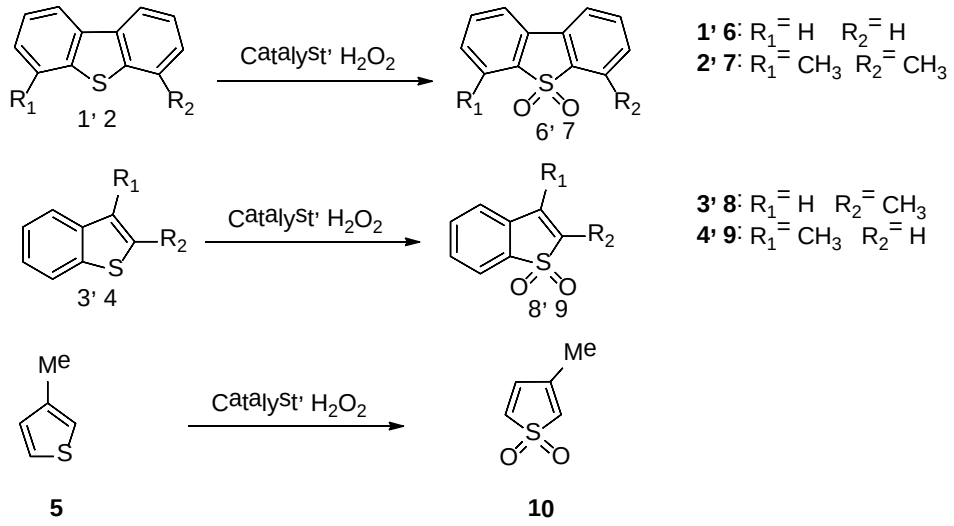

Table 19. Oxidation of DBT **1** to sulfone **6** with catalysts **I-V** in CH_2Cl_2 (25 °C) or *n*-octane (60°C).[a]
[a]The appropriate catalyst (3% w/w of MTO with respect to substrate) was added to **1** (0.1 mmol) in CH_2Cl_2 or *n*-octane (2.0 mL), followed by treatment with H_2O_2 (4.0 equivalents, 35% water solution), under magnetic stirring at 25°C and 60°C, respectively. [b]Yields correspond to substrate conversion.

Entry	Catalyst	Solvent	Time (h)	Yield (%)[b]
1	**I**	CH_2Cl_2	6	<3
2	**II**	CH_2Cl_2	6	>99
3	**III**	CH_2Cl_2	6	>99
4	**IV**	CH_2Cl_2	6	>99
5	**V**	CH_2Cl_2	6	>99
6	**I**	*n*-octane	24	n.d.
7	**PVP/MTO**	*n*-octane	24	51
8	**PVPN/MTO**	*n*-octane	24	60
9	**II**	*n*-octane	24	47
10	**III**	*n*-octane	24	59
11	**IV**	*n*-octane	24	79
12	**V**	*n*-octane	24	91

Irrespective to experimental conditions, the sulfone **6** was obtained as the only recovered product, the yield of **6** corresponding to the conversion of substrate (Figure 3.14, Table 19, entries 1-12). As expected, catalyst **I** showed a negligible activity, probably due to the low value of LF (Table 19, entries 1 and 6). As reported in Table 19, the oxidation of compound **1** with catalysts **II-V** in CH_2Cl_2 do in quantitative yield and conversion of substrate, to yield the sulfone **6** after only 6 h (Table 19, entries 2-5). A lower reactivity was observed in *n*-octane, in which case higher temperature and longer

reaction times were required (Table 19, entries 9-12). The low reactivity of MTO during the oxidation of aromatic sulfur derivatives in n-octane was previously reported[262]. Catalysts **II** and **III** showed a reactivity similar to PVP/MTO and PVPN/MTO alone, confirming that the adsorption of the MTO adducts on CNTs did not alter their catalytic performance (Table 19, entries 7-8 versus 9-10). On the other hand, catalysts **IV** and **V** were more reactive than catalysts **II** and **III**, catalyst **V** being the most active system (Table 19, entries 11 and 12).

Table 20. Oxidation of thiophene derivatives **1-5** with catalysts **II-V** in *n*-octane/CH_3CN mixture.[a]

Entry	Substrate	Catalyst	Product	Yield (%)
1	**1**	**V**[b]	**6**	83
2	**1**	**V**[c]	**6**	>90
3	**1**	**V**	**6**	>99
4	**1**	**II**	**6**	52
5	**1**	**III**	**6**	64
6	**1**	**IV**	**6**	81
7	**1**	**PVP/MTO**	**6**	56
8	**1**	**PVPN/MTO**	**6**	67
9	**2**	**II**	**7**	30
10	**2**	**III**	**7**	41
11	**2**	**IV**	**7**	70
12	**2**	**V**	**7**	80
13	**3**	**II**	**8**	18
14	**3**	**III**	**8**	21
15	**3**	**IV**	**8**	69
16	**3**	**V**	**8**	78
17	**4**	**II**	**9**	16
18	**4**	**III**	**9**	21
19	**4**	**IV**	**9**	42
20	**4**	**V**	**9**	51
21	**5**	**II**	**10**	5
22	**5**	**III**	**10**	7
23	**5**	**IV**	**10**	19
24	**5**	**V**	**10**	28

[a]The oxidations were performed with catalysts **II-V** (3% w/w of MTO with respect to substrate) in the presence of *n*-octane/CH_3CN 3:1 v/v mixture at 60°C for 3h. [b]*n*-octane/CH_3CN 1:1 v/v mixture at 60°C for 3h. [c]*n*-octane/CH_3CN 2:1 v/v mixture at 60°C for 3h.

Thus, the properties of the support (wrapped CNT_w), and the oxidation state of the resin (that is PVP versus PVPN) tuned the reactivity of the catalyst, in accordance with the results previously reported for the MTO adducts[274]. This effect may be in part ascribed to the different structure of the active site[269]. Co-solvents with high value of dielectric constant (acetonitrile, DMF and DMSO) have been applied in ODS processes to optimize the sulfur removal, since they can extract the sulfoxide and sulfone derivatives produced during the oxidation[283]. The advantage of the extraction-oxidation process is the high sulfur removal under lower H_2O_2/sulfur ratio, with concomitant improvement of catalyst stability[284]. For this reason, the oxidation of compounds **1** in *n*-octane was repeated with the most active catalyst **V** in the presence of acetonitrile (CH_3CN) in three different ratio values (*n*-octane/CH_3CN, 1:1, 2:1 and 3:1 v/v, respectively) at 60°C (Table 20, entries 1-3; Scheme 2). CH_3CN really increased the efficiency of the oxidation, leading to formation of sulfone **6** in high yield after 3 h (Table 20, entry 3), the 3:1 *n*-octane/CH_3CN v/v being the optimal mixture (Table 20, entry 1). These experimental conditions were successively applied for the oxidation of compound **1** with catalysts **II**-**IV** (in this set of experiments catalyst **I** was not analysed, due to its low reactivity). In accordance with data previously reported, catalysts **IV** and **V** were more reactive than **II**-**III** (Table 20, entries 3 and 6 versus entries 4 and 5), these latter showing a reactivity similar to PVP/MTO and PVPN/MTO adducts (Table 20, entries 4-5 versus 7-8). To evaluate the generality of the transformation, the attention was next focused on the oxidation of 4,6-DMDBT **2**, 2-MeBT **3**, 3-MeBT **4**, and 3-MeT **5** (Figure 3.13). Irrespective to experimental conditions, sulfones **7**-**10** were detected as the only recovered products (Table 20, entries 9-24). Again, catalysts **IV** and **V** were the most efficient systems (see for example, Table 20, entries 11-12 versus 9-10, and entries 15-16 versus 13-14). As a general trend, sulfones from dibenzothiophene and monobenzothiophene derivatives (products **6**-**9)** were obtained in an average yield higher than that from 3-methylthiophene (product **10)**, with the following order of reactivity: DBT>4,6-DMDBT>2-MeBT≈3-MeBT>3-MeT. This order of reactivity is in accordance with previously reported data for the oxidation of thiophene derivatives with nanosized catalysts[285], representing the effect of aromatic moieties and electron donating substituents on the electron density of sulfur atom[286]. Next, catalyst **V** was applied to a model fuel oil (MF) prepared by addition of equimolar amounts of **1**–**5** in *n*-octane, to gain an overall sulfur content of 2.8 mg/mL typical of a real fuel sample[287]. Treatment of the sample mixture MF/CH_3CN (3:1 v/v) with catalyst **V** (3% w/w of MTO with respect to total substrate) and H_2O_2 (4.0 equiv.),

at 60 °C yielded the quantitative conversions of **1**–**5** in 2 hours (Table 21, entry 3). The oxidation of compounds **1**–**5** in MF was more efficient and faster than that of any isolated substrates, suggesting the presence of synergic effects or autocatalysis phenomena (Table 21, entry 3 versus entry 2). Noteworthy, the highly recalcitrant substrate **5** was oxidized in a quantitative manner. In this latter case, the disproportionation reaction between two sulfoxide (or sulfoxide and sulfoxide-like) intermediates might be responsible for the increased yield of sulfones from the most recalcitrant substrates[288]. Previously, we observed a similar behaviour in the oxidation of MF with PVP/MTO and PVPN/MTO[265]. We can emphasize that catalyst **V** was more reactive than the corresponding PVPN/MTO system in the oxidation of MF, affording the quantitative conversion of substrates **1**–**5** with a lower LF value (Table 21, entry 3 versus entry 1). Finally, catalyst **V** efficiently oxidized compounds **1-5** when embedded in a real sample such as the synthetic diesel fuel (SDF) sample (3.8 mg/mL of total sulfur content) (Table 21, entry 4).

Table 21. Oxidation of model fuel oil (MF) and synthetic diesel fuel (SDF) samples by either catalyst **V** or PVPN/MTO.

Entry	Substrates	Solvent	Catalyst	Time (h)	Product (yield%)
1[a]	**1-4** in MF	n-octane	PVPNO•MTO	2	**6-9** (>99)
2[b]	**1-5**	n-octane/CH_3CN	**V**	3	**6** (>99); **7** (80); **8** (78); **9** (51), **10** (28)
3[c]	**1-5** in MF	MF/CH_3CN	**V**	2	**6** (>99); **7** (>99); **8** (>99); **9** (>99), **10** (>99)
4[c]	**1-5** in SDF	SDF/CH_3CN	**V**	2	**6** (>99); **7** (>99); **8** (>99); **9** (>99), **10** (47)

[a]Experimental conditions as reported in ref. 16: PVPN/MTO (5% w/w of MTO, LF=5.0), 4.0 equiv. of H_2O_2, 1.5 mL of MF having a total S concentration of 2.8 mg/mL, 70 °C.
[b]The oxidations of isolated compounds **1-5** were performed with catalysts **V** (3% w/w of MTO with respect to substrate), 4.0 equiv. of H_2O_2 in n-octane/CH_3CN (3:1 v/v) mixture, at 60 °C.
[c]Catalyst **V** (3% w/w of MTO with respect to substrate), 4.0 equiv. of H_2O_2 in MF/CH_3CN (or 8.0 equiv. of H_2O_2 for SDF/ CH_3CN) (3:1 v/v) mixture (2.0 mL), at 60 °C.

Note that catalyst **V** showed a similar performance when applied in the optimal conditions to SDF samples larger than 1000 ml, suggesting the feasibility of this process for a large scale.

Catalyst **V** was a stable system in the oxidation of substrate **1** in n-octane/CH_3CN (3:1 v/v ratio) mixture, as selected representative sample. In particular, it was recovered and recycled ten times, with only a slight decrease of the reactivity after the sixth run, after which it was stabilized at around 60% of the initial value (Table 22).

Table 22. Stability of catalyst **V** in the oxidation of DBT **1** and MF.[a]

Substrate		**Conversion (%)**									
		Run n. 1	Run n. 2	Run n. 3	Run n. 4	Run n. 5	Run n. 6	Run n. 7	Run n. 8	Run n. 9	Run n. 10
DBT (**1**)		>99	95	89	87	81	56	64	61	58	65
MF	DBT (**1**)	>99	>99	>99	90	84	68	71	65	61	64
	DMDBT (**2**)	>99	>99	>99	97	93	73	70	61	72	66
	2-MeBT (**3**)	>99	>99	>99	96	90	64	66	61	59	65
	3-MeBT (**4**)	>99	>99	95	87	89	78	72	69	68	67
	3-MeT (**5**)	>99	88	78	67	57	39	43	40	38	45

[a]After the first reaction, catalyst **V** was recovered by filtration; following runs were performed working under the same experimental conditions. [b]Yields of corresponding sulfones match with substrates conversion values.

Interestingly, catalysts **V** showed to be a stable system also in the oxidation of a MF sample (Table 22). Irrespective to the type of substrate, the conversion was high until the fifth run, after which it was stabilized at around 65% of the initial value (only in the case of **5** we observed a slightly lower value stabilized around 40%). These results are in accordance with the previously reported trend of stability in ODS processes of heterogeneous catalysts based on other active species. For example, TiO_2 nanoparticles retained the catalytic activity in the oxidation of DBT in MF at least for five runs[288], poly-oxometalates (POMs) nanoparticles for ten runs[289], and titanium Ti-modified SBA-15 (Ti-SBA15) for four runs[290].

Leaching experiments were performed to evaluate the absence of MTO in the homogeneous phase. In particular, the organic layer from any recycle of catalyst **V** was analyzed by ^{1}H NMR. The absence of the Re-Me peak (2.6 ppm), even after the sixth recycling run, highlighted that MTO was not released during the reaction. These results were further confirmed by the lack of catalytic activity in the washing solutions[291]. Moreover, the value of the total amount of immobilized rhenium was constant during the recycling runs (ICP-MS analysis). Based on these data, the slight decrease of the reactivity after the sixth run may be probably due to the formation of low reactive rhenium species, as confirmed by XPS analysis.

References

1 Anastas P.T., Warner J.C. Green Chemistry: Theory and Practice. New York: Oxford Univ. Press **1998**

2 Clark, J. From waste to wealth using green chemistry: The way to long term stability. *Curr. Opin. Green Chem.* **2017**, *8*, 10–13.

3 Sherwood, J.; Clark, J.H.; Farmer, T.J.; Herrero-Davilla, L.; Moity, L. Recirculation: A new concept to drive innovation in sustainable product design for bio-based products. Molecules **2017**, *22*, 48.

4 Anastas, P.T.; Zimmerman, J.B. Peer reviewed: Design through the 12 principles of green engineering. Environ. Sci. Technol. **2003**, *37*, 94–101.

5 Anastas, P.T.; Ferris, C.A. Benign by Design: Alternative Synthetic Design for Pollution Prevention; American Chemical Society: Washington, DC, USA, **1994** 577.

6 Ricciardi, M.; Cespi, D.; Celentano, M.; Genga, A.; Malitesta, C.; Proto, A.; Capacchione, C.; Cucciniello, R. Bio-propylene glycol as value-added product from Epicerol process. Sustain. Chem. Pharm. **2017**, *6*, 10–13.

7 Clark J.H. Green chemistry: today (and tomorrow). *Green Chem.* **2006**, 8, 17–21.

8 Knight D.J. **2006**. EU Regulation of Chemicals: REACH. *Rapra Rev. Rep.* 181, Rapra Technol. Ltd., Shawbury, UK; Harrison R.E, Hester R.E. Chemicals in the Environment: Assessing and Managing Risk. Cambridge, UK: RSC Publ **2006.**

9 Bozell J., Patel M.K., eds. Feedstocks for the Future: Renewables for the Production of Chemicals and Materials. Washington, DC: *Am. Chem. Soc.* **2006**.

10 Ragouskas A.J, Williams C.K., Davison B.H., Britovsek G., Cairney J., et al. The path forward for biofuels and biomaterials. *Science* **2006,** *311*, 484–89.

11 Climent M. J., Corma A. and Iborra S., *Green Chem.*, **2014**, *16*, 516–547.

12 Caspeta L., Buijs N. A. A. and Nielsen J., *Energy Environ. Sci.*, **2013**, *6*, 1077–1082.

13 Bruijnincx P.C.A. and Weckhuysen B. M., *Angew. Chem.*, **2013**, *52*, 11980–11987.

14 Dale B.E., Ong R.G., Energy, wealth, and human development: Why and how biomass pretreatment research must improve. *Biotechnol. Prog.* **2012**, *28*, 893–898;

15 Sannigrahi P., Ragauskas A. J., Characterization of fermentation residues from the production of bio-ethanol from lignocellulosic feedstocks. *J. Biobased Mat. Bioeng* **2011**, *5*, 514–519; Boerjan W., Ralph J., Baucher M., Lignin biosynthesis. *Annu. Rev. Plant Biol.* **2003**, *54*, 519–546.

16 M. Kleinert, T. Barth, Towards a lignocellulosic biorefinery: Direct one-step conversion of lignin to hydrogen-enriched biofuel *Energy Fuels*, **2008**, *22*, 1371–1379

17 Tuck C. O., Pérez E., Horváth I. T., Sheldon R. A., Poliakoff M., Valorization of biomass: Deriving more value from waste. *Science* **2012**, *337*, 695–699

18 Langholtz M. et al., Lignin-derived carbon fiber as a co-product of refining cellulosic biomass. SAE Int. *J. Mater. Manf* **2014**, 7, 115–121

19 Stewart D., Lignin as a base material for materials applications: Chemistry, application and economics. *Ind. Crops Prod.* **2008**, 27, 202–207

20 Chabannes, M.; et al. "In situ analysis of lignins in transgenic tobacco reveals a differential impact of individual transformations on the spatial patterns of lignin deposition at the cellular and subcellular levels". *Plant J.* 28 **2001** (*3*) 271–282.

21 Sarkanen K.V. & Ludwig C.H. (eds). Lignins: Occurrence, Formation, Structure, and Reactions. New York: *Wiley Intersci.* **1971**

22 Caño-Delgado A., Penfield S., Smith C., Catley M., Bevan M. Reduced cellulose synthesis invokes lignification and defense responses in Arabidopsis thaliana. *Plant J* **2003**, *34*, 351–362; Tronchet M., Balagué C., Kroj T., Jouanin L., Roby D. Cinnamyl alcohol dehydrogenases C and D, key enzymes in lignin biosynthesis, play an essential role in disease resistance in Arabidopsis. *Mol Plant Pathol* **2010**, *11*, 83–92

23 Boerjan W., Ralph J., Baucher M. () Lignin biosynthesis. *Annu Rev Plant Biol* **2003**, *54*, 519–546; Ralph J., Lundquist K., Brunow G., Lu F., Kim H., Schatz P.F., Marita J.M., Hatfield R.D., Ralph S.A., Christensen J.H., et al. Lignins: natural polymers from oxidative coupling of 4-hydroxyphenylpropanoids. *Phytochem Rev* **2004**, *3*, 29–60.

24 Humphreys J. M., Chapple C., Rewriting the lignin roadmap. *Curr. Opin. Plant Biol.* **2002**, *5*, 224–229.

25 Vanholme R. et al., Caffeoyl shikimate esterase (CSE) is an enzyme in the lignin biosynthetic pathway in Arabidopsis. *Science* **2013**, *341*, 1103–1106

26 Rippert P., Puyaubert J., Grisollet D., Derrier L., Matringe M. Tyrosine and phenylalanine are synthesized within the plastids in Arabidopsis. *Plant Physiol* **2009** *149*, 1251–1260).

27 Chapple C. Molecular-genetic analysis of plant cytochrome P450-dependent monooxygenases. *Annu Rev Plant Physiol Plant Mol Biol* **1998**, *49*, 311–343.

28 Achnine L, Blancaflor EB, Rasmussen S, Dixon RA. () Colocalization of l-phenylalanine ammonia-lyase and cinnamate 4-hydroxylase for metabolic channeling in phenylpropanoid biosynthesis. *Plant Cell* **2004,** *16*, 3098–3109

29 Novo Uzal E., Gómez Ros L.V., Pomar F., Bernal M.A., Paradela A., Albar J.P., Ros Barceló A. The presence of sinapyl lignin in Ginkgo biloba cell cultures changes our views of the evolution of lignin biosynthesis. *Physiol Plant* **2009** *135*, 196–213

30 Ralph J., Lundquist K., Brunow G., Lu F., Kim H., Schatz P.F., Marita J.M., Hatfield R.D., Ralph S.A., Christensen J.H., et al. Lignins: natural polymers from oxidative coupling of 4-hydroxyphenylpropanoids. *Phytochem Rev* **2004** *3*, 29–60

31 Lu F., Ralph J., Novel tetrahydrofuran structures derived from β-β-coupling reactions involving sinapyl acetate in Kenaf lignins. *Org Biomol Chem* **2008**, *6*, 3681–3694

32 Nakashima J., Chen F., Jackson L., Shadle G., Dixon R.A. Multi-site genetic modification of monolignol biosynthesis in alfalfa (Medicago sativa): effects on lignin composition in specific cell types. *New Phytol* **2008** *179* 738–750).

33 Lapierre C. et al., Structural alterations of lignins in transgenic poplars with depressed cinnamyl alcohol dehydrogenase or caffeic acid O-methyltransferase activity have an opposite impact on the efficiency of industrial kraft pulping. *Plant Physiol.* **1999**, *119*, 153–164

34 Zhao Q. et al., Loss of function of cinnamyl alcohol dehydrogenase 1 leads to unconventional lignin and a temperature-sensitive growth defect in Medicago truncatula. *Proc. Natl. Acad. Sci.* U.S.A. **2013**, *110*, 13660–13665

35 Vanholme R. et al., Metabolic engineering of novel lignin in biomass crops. *New Phytol.* **2012**, *196*, 978–1000

36 Wilkerson C. G. et al., Monolignol ferulate transferase introduces chemically labile linkages into the lignin backbone. *Science* **2014,** *344*, 90–93

37 Poursorkhabi V., Misra M., Mohanty A. K., Extraction of lignin from a co-product of the cellulosic ethanol industry and its thermal characterization. *BioResources* **2013**, *8*, 5083–5101

38 Laskar D.D., Zeng J., Yan L., Chen S., Yang B., Characterization of lignin derived from water-only flowthrough pretreatment of Miscanthus. *Ind. Crops Prod.* **2013**, *50*, 391–399.

39 Brandt A., Grasvik J., Hallett J. P. and Welton T., *Green Chem*., **2013**, *15*, 550–583 and references therein.

40 Kumar A.K., Parikh B.S., Pravakar M. Natural deep eutectic solvent mediated pre-treatment of rice straw: bioanalytical characterization of lignin extract and enzymatic hydrolysis of pre-treated biomass residue. *Environ Sci Pollut Res Int.* **2016**, *10*, 9265-75.

41 Wyman C. E., Potential synergies and challenges in refining cellulosic biomass to fuels, chemicals, and power. *Biotechnol. Progr.* **2003**, *19*, 254–262

42 National Research Council, National Academies Press, Washington, DC, **2011**

43 Chung H., Washburn N.R., Chemistry of lignin-based materials. *Green Mat.* **2013**, *1*, 137–160.

44 Lora J., "Industrial commercial lignins: sources, properties and applications," in Monomers, Polymers and Composites from Renewable Resources, M. N. Belgacem, A. Gandini, Eds. Elsevier, Oxford, **2008**, 225–241

45 Hirai N., Kubo S., Magara K., Combined cyclic voltammetry and in situ electrochemical atomic force microscopy on lead electrode in sulfuric acid solution with or without lignosulfonate. *J. Power Sources* **2009**, *191*, 97–102.

46 DeAngelis F., Reale S., Review – The lignin concept. Chim'Ind-Mila **2006**, *88*, 58–65

47 Li Y., Ragauskas A.J., Kraft lignin-based rigid polyurethane foam. J. Wood Chem. Technol. **2012**, *32*, 210–224.

48 Ciemniecki S.L., Glasser W.G., Multiphase materials with lignin: 1. Blends of hydroxypropyl lignin with poly(methyl methacrylate). *Polymer* **1988**, *29*, 1021–1029

49 Liang C., Li Z. and Dai S., *Angew. Chem.,* Int. Ed., **2008**, *47*, 3696–3717

50 Zhai Y., Dou Y., Zhao D., Fulvio P.F., Mayes R. T. and Dai S., *Adv. Mater.*, **2011**, *23*, 4828–4850.

51 Krishnan A.V., Stathis P., Permuth S.F., Tokes L. and Feldman D., Endocrinology, **1993**, *132*, 2279–2286.

52 Fache M., Darroman E., Besse V., Auvergne R., Caillol S. and Boutevin B., *Green Chem.*, **2014**, *16*, 1987–1998.

53 Meredith H.J., Jenkins C.L. and Wilker J.J., *Adv. Funct. Mater.*, **2014**, *24*, 3259–3267.

54 Lee H., Scherer N.F. and Messersmith P.B., *Proc. Natl. Acad. Sci.* U. S. A., **2006**, *103*, 12999–13003.

55 Jin S., Xiao Z., Li C., Chen X., Wang L., Xing J., Li W. and Liang C., Catal. Today, **2014**, *234*, 125–132.

56 Aouf C., Nouailhas H., Fache M., Caillol S., Boutevin B. and Fulcrand H., *Eur. Polym. J.*, **2013**, *49*, 1185–1195.

57 Pandey M.P., Kim C.S., Lignin depolymerization and conversion: A review of thermochemical methods. *Chem. Eng. Technol.* **2011**, *34*, 29–41.

58 Zakzeski J., Bruijnincx P.C.A., Jongerius A.L., Weckhuysen B.M., The catalytic valorization of lignin for the production of renewable chemicals. *Chem. Rev.* **2010** 110, 3552–3599.

59 Wang H.M., Male J., Wang Y., Recent advances in hydrotreating of pyrolysis bio-oil and its oxygen-containing model compounds. *ACS Catal.* **2013**, *3*, 1047–1070

60 Salvachúa D. et al., Fungal pretreatment: An alternative in second-generation ethanol from wheat straw. *Bioresour. Technol.* **2011**, *102*, 7500–7506

61 Á.T. Martínez et al., Biodegradation of lignocellulosics: Microbial, chemical, and enzymatic aspects of the fungal attack of lignin. *Int. Microbiol.* **2005**, *8*, 195–204; Bugg T.D.H., Ahmad M., Hardiman E. M., Singh R., The emerging role for bacteria in lignin degradation and bio-product formation. *Curr. Opin. Biotechnol.* **2011**, *22*, 394–400

62 Xu, T.; Zhang, N.; Nichols, H.L.; Shi, D.; Wen, X. Modification of nanostructured materials for biomedical applications. *Mater. Sci. Eng. C* **2007**, *27*, 579–594.

63 Hussain, F. Review article: Polymer-matrix nanocomposites, processing, manufacturing, and application: An overview. *J. Compos. Mater.* **2006**, *40*, 1511–1575

64 Frangville, C.; Rutkevičius, M.; Richter, A.P.; Velev, O.D.; Stoyanov, S.D.; Paunov, V.N. Fabrication of environmentally biodegradable lignin nanoparticles. *ChemPhysChem* **2012**, *13*, 4235–4243.

65 Qian, Y.; Deng, Y.; Qiu, X.; Li, H.; Yang, D. Formation of uniform colloidal spheres from lignin, a renewable resource recovered from pulping spent liquor. *Green Chem.* **2014**, *16*, 2156

66 Tortora, M.; Cavalieri, F.; Mosesso, P.; Ciaffardini, F.; Melone, F.; Crestini, C. Ultrasound driven assembly of lignin into microcapsules for storage and delivery of hydrophobic molecules. *Biomacromolecules* **2014**, *15*, 1634–1643.

67 F. Hennrich, C. Chan, V. Moore, M. Rolandi, and M. O'Connell, Carbon Nanotubes Properties and Applications, Taylor & Francis Group, **2006**

68 Kroto H.W., Heath J.R., O'Brien S.C., Curl R.F., and Smalley R.E., C60: Buckminster fullerene, *Nature*, **1985**, *318*, 6042, 162–163

69 Iijima S., Helical microtubules of graphitic carbon, *Nature*, **1991**, *354*, 6348, 56–58,

70 Iijima S. and Ichihashi T., "Single-shell carbon nanotubes of 1-nm diameter, *Nature*, **1993** *363*, 603–605.

71 Meyyappan M., Delzeit L., Cassell A., and Hash D., Carbon nanotube growth by PECVD: a review, *Plasma Sources Science and Technology*, **2003** *12*, 205–216,

72 Lin T., Bajpai V., Ji T., and Dai L., "Chemistry of carbon nanotubes," *Australian Journal of Chemistry*, **2003**, *56*, 635–651.

73 Yu M.F., Files B.S., Arepalli S., and Ruoff R.S., "Tensile loading of ropes of single wall carbon nanotubes and their mechanical properties," *Physical Review Letters*, **2000**, *84*, 5552–5555.

74 P.M. Ajayan, T.W. Ebbesen "Large-scale synthesis of carbon nanotubes," *Nature*, **1992**, *358*, 6383, 220–222.

75 Thess A., Lee R., Nikolaev P. et al., "Crystalline ropes of metallic carbon nanotubes," *Science*, **1996**, *273*, 5274, 483–487

76 Kong J., Cassell A.M., and Dai H., "Chemical vapor deposition of methane for single-walled carbon nanotubes," *Chemical Physics Letters*, **1998**, *292*, 4–6, 567–574, S. Fan, M. G. Chapline, N. R. Franklin, T. W. Tombler, A. M. Cassell, and H. Dai, "Self-oriented regular arrays of carbon nanotubes and their field emission properties," *Science*, **1999**C, *283*, 5401, 512–514.

77 Gao B., *Chem. Phys. Lett.* **2000**, *327*, 69

78 Ma R.Z., et al., Science in China Series E-*Technological Sciences* **2000**, *43*, 178

79 Lievonen, M.; Valle-Delgado, J.J.; Mattinen, M.-L.; Hult, E.-L.; Lintinen, K.; Kostiainen, M.A.; Paananen, A.; Szilvay, G.R.; Setälä, H.; Österberg, M. A simple process for lignin nanoparticle preparation. *Green Chem.* **2016**, *18*, 1416–1422.

80 Qian, Y.; Zhong, X.; Li, Y.; Qiu, X. Fabrication of uniform lignin colloidal spheres for developing natural broad-spectrum sunscreens with high sun protection factor. *Ind. Crops Prod.* **2017**, *101*, 54–60.]

81 Yearla, S.R.; Padmasree, K. Preparation and characterisation of lignin nanoparticles: Evaluation of their potential as antioxidants and UV protectants. *J. Exp. Nanosci.* **2016**, *11*, 289–302.

82 Fukushima, R.S.; Hatfield, R.D. Extraction and isolation of lignin for utilization as a standard to determine lignin concentration using the acetyl bromide spectrophotometric method. *J. Agric. Food Chem.* **2001**, *49*, 3133–3139.

83 Li, H.; Deng, Y.; Wu, H.; Ren, Y.; Qiu, X.; Zheng, D.; Li, C. Self-assembly of kraft lignin into nanospheres in dioxane-water mixtures. *Holzforschung* **2016**, *70*, 725–731.

84 Li, H.; Deng, Y.; Liu, B.; Ren, Y.; Liang, J.; Qian, Y.; Qiu, X.; Li, C.; Zheng, D. Preparation of nanocapsules via the self-assembly of kraft lignin: A totally green process with renewable resources. *ACS Sustain. Chem. Eng.* **2016**, *4*, 1946–1953.

85 Leskinen T., Smyth M., Xiao Y., Lintinen K., Mattinen M.L., Kostiainen M.A., Oinas P., Österberg M., Scaling Up Production of Colloidal Lignin Particles SPECIAL ISSUE LIGNIN *Nordic Pulp & Paper Research Journal* **2017**, *32*, 4.

86 Chen L. et al. Green synthesis of lignin nanoparticle in aqueous hydrotropic solution toward broadening the window for its processing and application *Chemical Engineering* Journal **2018**, *346*, 217-225

87 Deng, Y.; Feng, X.; Zhou, M.; Qian, Y.; Yu, H.; Qiu, X., Investigation of Aggregation and Assembly of Alkali Lignin Using Iodine as a Probe. *Biomacromolecules* **2011**, *12*, 1116-1125.

88 Deng Y., Feng X., Yang D., Yang D., Xueqing Q., Xueqing Q. π-π Stacking of the aromatic groups in lignosulfonates *Bioresources* **2012**, *7*

89 Tian D., Hu J., Bao J., Chandra R.P., Saddler J.N., Lu C. Lignin valorization: lignin nanoparticles as high-value bio-additive for multifunctional nanocomposites. *Biotechnol Biofuels.* **2017**, *10*,192

90 Del Saz-Orozco, B.; Oliet, M.; Alonso, M.V.; Rojo, E.; Rodríguez, F. Formulation optimization of unreinforced and lignin nanoparticle-reinforced phenolic foams using an analysis of variance approach. *Compos. Sci. Technol.* **2012**, *72*, 667–674.

91 Henrikki Sipponen M., Smyth M., Leskinen T., Johanssona L.S. and Österberg M. All-lignin approach to prepare cationic colloidal lignin particles: stabilization of durable Pickering emulsions *Green Chem*, **2017**,*19*, 5831-5840.

92 Venkatesan, P.; Manavalan, R.; Valliappan, K. Microencapsulateation: A Vital Technique in Novel Drug Delivery System. *J. Pharm. Sci. Res.* **2009**, *1*, 26–35.; Singh, M.N.; Hemant, K.S.Y.; Ram, M.; Shivakumar, H.G. Microencapsulation: A promising technique for controlled drug delivery. *Res. Pharm. Sci.* **2010**, *5*, 65–77.

93 Tsuji, K. Microencapsulation of pesticides and their improved handling safety. *J. Microencapsul.* **2001**, *18*, 137–147.

94 Green, D.W.; Mann, S.; Oreffo, R.O.C. Mineralized polysaccharide capsules as biomimetic microenvironments for cell, gene and growth factor delivery in tissue engineering. *Soft Matter* **2006**, *2*, 732–737; Kurosaki, T.; Kitahara, T.; Fumoto, S.; Nishida, K.; Yamamoto, K.; Nakagawa, H. Chondroitin Sulfate Capsule System for Efficient and Secure Gene Delivery. *J. Pharm. Pharm. Sci.* **2010**, *13*, 351–361.

95 Desai, K.G.H.; Jin Park, H. Recent Developments in Microencapsulation of Food Ingredients. *Dry. Technol.* **2005**, *23*, 1361–1394.

96 Herzfeldt, C.D.; Kümmel, R. Dissociation constants, solubilities and dissolution rates of some selected nonsteroidal antiinflammatories. *Drug Dev. Ind. Pharm.* **1983**, *9*, 767–793. Vayssières, L.; Chanéac, C.; Tronc, E.; Jolivet, J.P. Size Tailoring of Magnetite Particles Formed by Aqueous Precipitation: An Example of Thermodynamic Stability of Nanometric Oxide Particles. *J. Colloid Interface Sci.* **1998**, *205*, 205–212.

97 Yiamsawas, D.; Baier, G.; Thines, E.; Landfester, K.; Wurm, F.R. Biodegradable lignin nanocontainers. *RSC Adv.* **2014**, *4*, 11661–11663.

98 Dai, L.; Liu, R.; Hu, L.Q.; Zou, Z.F.; Si, C.L. Lignin Nanoparticle as a Novel Green Carrier for the Efficient Delivery of Resveratrol. *ACS Sustain. Chem. Eng.* **2017**, *5*, 8241–8249.

99 Qian Y., Qiu X., and Zhu S. Sunscreen Performance of Lignin from Different Technical Resources and Their General Synergistic Effect with Synthetic Sunscreens *ACS Sustainable Chem. Eng.* **2016**, *4*, 4029-4035

100 Gutiérrez-Hernández J.M., Escalante A., Murillo-Vázquez R.N., Delgado E., González F.J., Use of Agave tequilana-lignin and zinc oxide nanoparticles for skin photoprotection Toríz G3 *J Photochem Photobiol B.* **2016**, *63*,156-61

101 Popa, V.I.; Capraru, A.M.; Grama, S.; Malu¸tan, T. Nanoparticles based on modified lignins with biocide properties. *Cellul. Chem. Technol.* **2011**, *45*, 221–226.

102 Nada, A.M.A.; El-Diwany, A.I.; Elshafei, A.M. Infrared and antimicrobial studies on different lignins. *Acta Biotechnol.* **1989** (*9*) 295–298. Zemek, J.; Košíková, B.; Augustín, J.; Joniak, D. Antibiotic properties of lignin components. *FoliaMicrobiol.* (Praha) **1979**, *24*, 483–486.

103 Yang, W.; Owczarek, J.S.S.; Fortunati, E.; Kozanecki, M.; Mazzaglia, A.; Balestra, G.M.M.; Kenny, J.M.M.; Torre, L.; Puglia, D. Antioxidant and antibacterial lignin nanoparticles in polyvinyl alcohol/chitosan films for active packaging. *Ind. Crops Prod.* **2016**, *94*, 800–811

104 Wang, S.X.; Yang, L.; Stubbs, L.P.; Li, X.; He, C. Lignin-derived fused electrospun carbon fibrous mats as high-performance anode materials for lithium ion batteries. *ACS Appl. Mater. Interfaces* **2013**, *5*, 12275–12282.

105 Kim J.B., J. Grate W., and Wang P., "Nanostructures for enzyme stabilization," Chemical Engineering Science, **2006**, *61*, 3, 1017–1026

106 Laurent N., Haddoub R., and. Flitsch S. L, "Enzyme catalysis on solid surfaces," *Trends in Biotechnology*, **2008**, *26*, 328–337.

107 Jia H., Zhu G., and Wang P., "Catalytic behaviors of enzymes attached to nanoparticles: the effect of particle mobility," *Biotechnology and Bioengineering* **2003**, *84*, 406–414

108 Shim, Kam N.W.S., Chen R J., Li Y., and Dai H., Functionalization of carbon nanotubes for biocompatibility and biomolecular recognition, *Nano Letters*, **2002**, 2, *4*, 285–288; Zhang D.B. and Henthorn P., Synthesis of PEGylated single wall carbon nanotubes by a photoinitiated graft from polymerization, *AIChE Journal*, **2010**, *6*, 1610–1615.

109 Palonen, H.; Tjerneld. F.; Zacchi, G.; Tenkanen, M. J. *Biotechnol.* **2004**, 107, 65-72.

110 - Salas, C.; Rojas, O. J.; Lucia, L. A.; Hubbe, M. A.; Genzer, J. *ACS Appl. Mater. Interfaces* **2012**, *5*, 199-206.

111 Rahikainen, J. Cellulase-lignin interactions in the enzymatic hydrolysis of lignocellulose. VTT Technical Research Centre of Finland, Espoo, Finland, **2013.**

112 Yamaguchi, A.; Isozaki, K.; Nakamura, M.; Takaya, H.; Watanabe, *T. Sci. Rep.* **2016**, *6*, 21833.

113 Matsuura K., Saito T., Okazaki T., Ohshima S., Yumura M., and Iijima S., "Selectivity of water-soluble proteins in single-walled carbon nanotube dispersions," *Chemical Physics Letters* **2006**, *429*, 497–502.

114 Spahn, C., & Minteer, S. D. Enzyme immobilization in biotechnology. Recent Patents on Engineering **2008**, *2*, 195-200.

115 Felipe Díaz J. et al. Enzyme immobilization in MCM-41 molecular sieve Kenneth J.Balkus Jr) **1996**, *2*, 15-126.

116 Asuri P., Karajanagi S.S., Yang H., Yim T.J., Kane R.S., and Dordick J.S., "Increasing protein stability through control of the nanoscale environment," *Langmuir*, **2006**, *22*, 5833–5836.

117 Vogler, E. A. *Biomaterials* **2012**, 33, 1201-1237

118 Penna, M. J.; Mijajlovic, M.; Biggs, M. J. J. *Am. Chem. Soc.* **2014**, 136, 5323-5331

119 Tasis D., Tagmatarchis N., Bianco A., and Prato M., "Chemistry of carbon nanotubes" *Chemical Reviews*, **2006,** *106*, 1105–1136

120 Pantarotto D., Partidos C.D., Graff R. et al., "Synthesis, structural characterization, and immunological properties of carbon nanotubes functionalized with peptides," *Journal of the American Chemical Society*, **2003**, *125*, 6160–6164

121 Kim B. J., Kang B. K., Bahk Y. Y., Yoo K. H., and Lim K. J., "Gated phase-modulation feedback approach to fiber-optic gyroscopes," *Current Applied Physics*, **2009**, *9*, 263–265

122 Besteman K., Lee J. O., Wiertz F. G. M., Heering H. A., and Dekker C., "Enzyme-coated carbon nanotubes as single-molecule biosensors," *Nano Letters* **2003**, *3*, 727–730

123 Singh B. D. Biotechnology: Expanding horizons. **2015**.

124 Capecchi E., Piccinino D.2, Delfino I., Bollella P., Antiochia R., Saladino R., Functionalized Tyrosinase-Lignin Nanoparticles as Sustainable Catalysts for the Oxidation of Phenols. *Nanomaterials* **2018**, 8, 438

125 Mallan L., Suiting Up for Space: the Evolution of the Space Suit, John Day Co., NewYork, **1971**, 154.

126 Love C., Estroff L.A., Kriebel J.K., Nuzzo R.G., Whitesides G.M., Self- assembled monolayers of thiolates on metals as a form of nanotechnology, *Chem. Rev.* **2005**, *105*, 1103–1169

127 Tao F., Bernasek S.L., Understanding odd-even effects in organic self-assembled monolayers, *Chem. Rev.* **2007**, *107*, 1408–1453

128 Vericat C., Vela M.E., Benitez G., Carro P., Salvarezza R.C., Self-assembled monolayers of thiols and dithiols on gold: new challenges for a well-known system, *Chem. Soc. Rev.* **2010**, *39*, 1805–1834

129 Häkkinen H. The gold–sulfur interface at the nanoscale, *Nature Chemistry* **2012**, 4, 443–455

130 Bain C.D., Troughton E.B., Tao Y.T., Evall J., Whitesides G.M., and Nuzzo R.G. *J. Am. Chem. Soc.* **1989**, *111*, 321

131 Ulman A., Eilers J.E., and Tillman N. *Langrnuir* **1987**, *5*, 1147

132 Bruening, M. L.; Zhou, Y.; Aguilar, G.; Agee, R.; Bergbreiter,D. E.; Crooks, R. M. *Langmuir* **1997**, *13*, 770-778

133 Bain C.D., Troughton E.B., Tao Y.T., Evall J., Whitesides G.M., Huzzo R.G. Formation of monolayer films by the spontaneous assembly of organic thiols from solution onto gold *J. Am. Chem. Soc.*, **1989**, *111*, 321-335

134 Lee H., Dellatore S.M., Miller W.M., Messersmith P.B. Mussel-inspired surface chemistry for multifunctional coatings *Science*, **2007**(*318*), 426-430; Y. Liu, K. Ai, L. Lu Polydopamine and its derivative materials: synthesis and promising applications in energy, environmental, and biomedical fields *Chem. Rev.*, **2014**, *114*, 5057-5115

135 T.S. Sileika, D.G. Barrett, R. Zhang, K.H.A. Lau, P.B. Messersmith Colorless multifunctional coatings inspired by polyphenols found in tea chocolate, and wine *Angew. Chem. Int. Ed.*, **2013**, 52, 10766-10770

136 V. Ball Permeability of silver cations through (PAH–PSS)m multilayer films to deposit silver in underlying (PAH–TA)n film without external reducing agent at pH 5.0 *Colloids Surf. A: Physicochem. Eng. Asp.,* **2015**, *484*, 70-74.

137 Ghosh, S.K. In Functional Coatings: By Polymer Microencapsulation; Ed. Wiley-VCH **2006**, 1−28.

138 McShane, M.J.; Lvov, Y.M. In Dekker Encyclopedia of Nanoscience and Nanotechnology, Marcel, **2004**, 1–16.

139 Laugel, N.; Betscha, C.; Winterhalter, M.; Voegel J.C.; Schaaf, P.; Ball, V. Relationship between the growth regime of polyelectrolyte multilayers and the polyanion/polycation complexation enthalpy. *J. Phys. Chem.* B **2006**, *110*, 19443–19449.

140 Shutava, T.; Prouty, M.; Kommireddy, D.; Lvov, Y. pH Responsive Decomposable Layerby-Layer Nanofilms and Capsules on the Basis of Tannic Acid, *Macromolecules*, **2005**, *38*, 2850–2858

141 Tian, D.; Hu, J.; Bao, J.; Chandra, R.P.; Saddler, J.N. and Lu C. Lignin valorization: lignin nanoparticles as high-value bio-additive for multifunctional nanocomposites. *Biotechnol Biofuels.* **2017**, *10*, 192-203.

142 Qian, Y.; Qiu, X.; Zhu, S. Lignin: a nature-inspired sun blocker for broad-spectrum sunscreens. *Green Chem.* **2015**, *17*, 320-324.

143 Zhu, H.; Stein, E.W.; Lu, Z.; Lvov, Y.M.; McShane, M.J. Synthesis of Size-Controlled Monodisperse Manganese Carbonate Microparticles as Templates for Uniform Polyelectrolyte. *Microcapsule Formation Chem. Mater.* **2005**, *17*, 2323-2328

144 Safdar, M.N.; Kausar, T.; Jabbar, S.; Mumtaz, A.; Ahad, K.; Saddozai, A.A. Extraction and quantification of polyphenols from kinnow (Citrus reticulate L.) peel using ultrasound and maceration techniques. *J Food Drug Anal* **2017**, *25*, 488-500

145 Granata A. and Argyropoulos D.S. 2-Chloro-4,4,5,5-tetramethyl-1,3,2-dioxaphospholane, a Reagent for the Accurate Determination of the Uncondensed and Condensed Phenolic Moieties in Lignins. *J. Agric. Food Chem*. **1995**, *43*, 1538-1544

146 a. Melone, F.; Saladino, R.; Lange, H.; Crestini, C. Tannin Structural Elucidation and Quantitative 31P NMR Analysis. 2. Hydrolyzable Tannins and Proanthocyanidins. *J. Agric. Food Chem.* **2013**, *61*, 9307–9315 b. Pu, Y.; Caob, S.; Ragauskas, A.J. Application of quantitative 31P NMR in biomass lignin and biofuel precursors characterization *Energy Environ. Sci.*, **2011**, *4*, 3154-3166

147 Siatka, T.; Kašparová, M. Seasonal Variation in Total Phenolic and Flavonoid Contents and DPPH Scavenging Activity of Bellis perennis L. *Flowers Molecules* **2010**, *15*, 9450-9461.

148 Antipov, A.A.; Shchukin, D.; Fedutik, Y.; Petrov A.I.; Sukhorukov G.B; Moehwald, H. Carbonate microparticles for hollow polyelectrolyte capsules fabrication. *Colloids and Surfaces A: Physicochem. Eng. Aspects* **2003**, *224*, 175-183.

149 Xiong, F.; Han, Y.; Wang, S.; Li, G.; Qin, T.; Chen, Y.; Chu, F. Preparation and Formation Mechanism of Renewable Lignin Hollow Nanospheres with a Single Hole by Self-Assembly. *ACS Sustain. Chem. Eng.*, **2017**, *5*, 2273–2281.

150 Yi, H.; Wu, L.Q.; Bentley, W.E.; Ghodssi, R.; Rubloff, G.W.; Culver, J.N.; Payne, G.F.; Biofabrication with chitosan. Biomacromolecules **2005**, 6, 2881–2894.

151 Shutava, T.; Lvov, Y.M.; Microcapsules of Tannic Acid and Chitosan for Protein Encapsulation. J. Nano-engineered *Nanosci. Nanotechnol.* **2006**, *6*, 1655–1661.

152 Ito, K.; Miki, H.; Ohba, Y. Interaction between acyclic phenol--formaldehyde oligomers and quaternary ammonium ions *J. Pharm. Soc. Jpn*, **2002**, *122*, 413-417.

153 Sionkowska, A.; Kaczmarek, B.; Lewandowska, K. Modification of collagen and chitosan mixtures by the addition of tannic acid. *J Mol. Liquids* **2014**, *199*, 318-323.

154 Fan, H.; Wang, J.; Zhang, Q.; Jin, Z. Tannic Acid-Based Multifunctional Hydrogels with Facile Adjustable Adhesion and Cohesion Contributed by Polyphenol Supramolecular Chemistry. Omega, 2017, *2*, 6668–6676.

155 Brand-Williams, W.; Cuvelier M.E.; Berset, C. Use of a free radical method to evaluate antioxidant activity. *Food Sci. Technol.* **1995**, *28*, 25-30.

156 Rao, S.; Padmasree, Y.; K. Padmasree. Preparation and characterization of lignin nanoparticles: evaluation of their potential as antioxidants and UV protectants. *J. Exp. Nanosci.* **2016**, *11*, 289-302.

157 Sarkanen, S.; Teller, D.C.; Abramowski, E.; McCarthy, J.L., Lignin. 19. Kraft Lignin Component Conformation and Associated Complex Configuration in Aqueous Alkaline Solution. *Macromolecules* **1982**, *15*, 1098-1104

158 Sarkanen, S.; Teller, D. C.; Stevens, C. R.; McCarthy, J. L., Lignin. 20. Associative Interactions Between Kraft Lignin Components. *Macromolecules* **1984**, *17*, 2588-2597.

159 Qian, Y.; Qiu, X.; Zhu, S. Sunscreen Performance of Lignin from Different Technical Resources and Their General Synergistic Effect with Synthetic Sunscreens. *ACS Sustain. Chem. Eng.* **2016**, *4*, 4029–4035.

160 Bourbonnais, R.; Paice, M. Voltammetric Measurement of Lignin in Pulp and Paper Samples An Electron Transfer Catalytic Approach with Mediators. *J. Electrochem. Soc.* **2004**, *151*, 246-249.

161 Gülçin, İ.; Huyut, Z.; Elmastaş, M.; Aboul-Enein, H. Y. Radical scavenging and antioxidant activity of tannic acid. *Arab. J. Chem.* **2010**, *3*, 43-53.

162 Walczak, M. M.; Dryer, D.A.; Jacobson, D.D.; Foss, M.G.; Flynn N.T. pH Dependent Redox Couple: An Illustration of the Nernst Equation. *J. Chem. Educ.* **1997**, *74*, 1195.

163 Leskinen, T.; Witos, J.; Valle Delgato, J.J.; Lintinen, K.S.; Kostiainen, M.A.; Wiedmer, S.K.; Osterberg, M.; Mattinen, M.L. Adsorption of proteins on colloidal lignin particles for advanced biomaterials. *Biomacromolecules* **2017**, *18*, 2767–2776.

164 Strobel, K.L.; Pfeiffer, K.A.; Blanch, H.W.; Clark, D.S. Structural Insights into the Affinity of Cel7A Carbohydrate-binding Module for Lignin. *J. Biol. Chem.* **2015**, *290*, 22818–22826.

165 Westereng, B.; Cannella, D.; Agger, J.W.; Jørgensen, H.; Andersen, M.L.; Eijsink, V.G.H.; Felby, C. Enzymatic cellulose oxidation is linked to lignin by long-range electron transfer. *Sci. Rep.* **2015**, *5*, 18561.

166 Frommhagen, M.; Mutte, S.K.; Westphal, A.H.; Koetsier, M.J.; Hinz, S.W.A.; Visser, J.; Vincken, J.-P.; Weijers, D.; van Berkel, W.J.H.; Gruppen, H.; et al. Boosting LPMO-driven lignocellulose degradation by polyphenol oxidase-activated lignin building blocks. *Biotechnol. Biofuels* **2017**, *10*, 121.

167 Frommhagen, M.; Koetsier, M.J.; Westphal, A.H.; Visser, J.; Hinz, S.W.A.; Vincken, J.-P. Lytic Polysaccharide monooxygenase from Myceliophthora thermophila C1 differ in substrate preference and reducing agent specificity. *Biotechnol. Biofuels* **2016**, *9*, 186.

168 Fiorentino, D.; Gallone, A.; Fiocco, D.; Palazzo, G.; Mallardi, A. Mushroom tyrosinase in polyelectrolyte multilayers as an optical biosensor for o-diphenols. *Biosens. Bioelectron.* **2010,** *25*, 2033–2037.

169 Dinçer, A.; Becerik, S.; Aydemir, T. Immobilization of tyrosinase on chitosan–clay composite beads. *Int. J.Biol. Macromol.* **2012**, *50*, 815–820.

170 Guazzaroni, M.; Crestini, C.; Saladino, R. Layer-by-Layer coated tyrosinase: An efficient and selective synthesis of catechols. *Bioorg. Med. Chem.* **2012**, *20*, 157–166.

171 Subrizi, F.; Crucianelli, M.; Grossi, V.; Passacantando, M.; Pesci, L.; Saladino, R. Carbon Nanotubes as Activating Tyrosinase Supports for the Selective Synthesis of Catechols. *ACS Catal.* **2014**, *4*, 810–822.

172 Botta, G.; Delfino, M.; Guazzaroni, M.; Crestini, C.; Onofri, S.; Saladino, R. Selective Synthesis of DOPA and DOPA Peptides by Native and Immobilized Tyrosinase in Organic Solvent. *ChemPlusChem* **2013**, *78*, 325–330.

173 Bozzini, T.; Botta, G.; Delfino, M.; Onofri, S.; Saladino, R.; Amatore, D.; Sgarbanti, R.; Nencioni, L.; Palamara, A.T. Tyrosinase and Layer-by-Layer supported tyrosinases in the synthesis of lipophilic catechols with antiinfluenza activity. *Bioorg. Med. Chem.* **2013**, *21*, 7699–7708.

174 Botta, L.; Bizzarri, B.M.; Crucianelli, M.; Saladino, R. Advances in biotechnological synthetic applications of carbon nanostructured systems. *J. Mater. Chem. B* 2017, *5*, 6490–6510.

175 Ismaya, W.T.; Rozeboom, H.J.; Schurink, M.; Boeriu, C.G.; Wichers, H.; Dijkstra, B.W. Crystallization and preliminary X-ray crystallographic analysis of tyrosinase from the mushroom Agaricus bisporus. *Acta Crystallogr.* **2011**, *67*, 575–578.

176 El Hage, R.; Brosse, N.; Chrusciel, L.; Sanchez, C.; Sannigrahi, P.; Rag, A. Characterization of milled wood lignin and ethanol organosolv lignin from Miscanthus. *Polym. Degrad. Stab.* **2009**, *94*, 1632–1638.

177Hu, J.; Shen, D.;Wu, S.; Zhang, H.; Xiao, R. Composition Analysis of Organosolv Lignin and Its Catalytic Solvolysis in Supercritical Alcohol. *Energy Fuels* **2014**, *28*, 4260–4266.

178 Lu, F.; Ralph, J. The DFRC method for lignin analysis. 2. Monomers from isolated lignins. *J. Agric. Food Chem.* **1998**, *46*, 547–552.

179 Jiang, C.; He, H.; Jiang, H.; Ma, L.; Jia, D.M. Nano-lignin filled natural rubber composites: Preparation and characterization. *Express Polym. Lett.* **2013**, *7*, 480–493

180 Leboukh, S.; Gouzi, H.; Coradin, T.; Yahia, H. An optical catechol biosensor based on a desert truffle tyrosinase extract immobilized into a sol–gel silica layered matrix. *J. Sol-Gel Sci. Technol.* **2018**, *86*, 675–681.
181 Malik, A.; Khan, M.T.H.; Khan, S.B.; Ahmad, A.; Choudhary, M.I. Tyrosinase inhibitory lignans from the methanol extract of the roots of Vitex negundo Linn and their structure-activity relationship. *Phytomedicine* **2006**, *13*, 255–260.

182 Grönqvist, S.; Viikari, L.; Niku-Paavola, M.-L.; Orlandi, M.; Canevali, C.; Buchert, J. Oxidation of milled wood lignin with laccase, tyrosinase and horseradish peroxidase. *Appl. Microbiol. Biotechnol.* **2005**, *67*, 489–494.

183 Min, K.; Yum, T.; Kim, J.; Woo, H.M.; Kim, Y.; Sang, B.-I.; Yoo, Y.J.; Kim, Y.H.; Um, Y. Perspectives for biocatalytic lignin utilization: Cleaving 4-O-5 and Ca-Cb bonds in dimeric lignin model compounds catalyzed by a promiscuous activity of tyrosinase. *Biotech. Biofuels* **2017**, *10*, 212.

184 Cie ´ nska, M.; Labus, K.; Lewa´ nczuk, M.; Ko´zlecki, T.; Liesiene, J.; Bryjak, J.; Legault, C. Effective L-Tyrosinehydroxylation of native and immobilized tyrosinase. *PLoS ONE* **2016**, *11*, 4016-4213.

185 Li, Y.; Qiu, X.; Qian, Y.; Xiong, W.; Yang, D. pH-responsive lignin-based complex micelles: Preparation, characterization and application in oral drug delivery. *Chem. Eng. J.* **2017**, *327*, 1176–1183.

186 Caluey, A.N.; Wilson, J.N. Functionalized lignin biomaterials for enhancing optical properties and cellular interactions of dyes. *Biomater. Sci.* **2017**, *5*, 2114–2121.

187 Hattori, Y.; Sakaguchi, M.; Maitani, Y. Folate-linked lipid-based nanoparticles deliver a NFB decoy into activated murine macrophage-like RAW264 7 cells. *Biol. Pharm. Bull.* **2006**, *29*, 1516–1520.

188 Piccinino, D.; Delfino, M.; Botta, G.; Crucianelli, M.; Grossi, V.; Passacantando, M.; Saladino, R. Highly efficient synthesis of aldehydes by layer-by-layer multi-walled carbon nanotubes (MWCNTs) laccase mediator systems. *Appl. Catal. A Gen.* **2015**, *499*, 77–88.

189 Pillai, K.V.; Renneckar, S. Cation p-interactions as a mechanism in technical lignin adsorption to cationic surfaces. *Biomacromolecules* **2009**, *10*, 798–804

190 Yu, C.-M.; Yen, M.-J.; Chen, L.-C. A bioanode based on MWCNT/protein-assisted co-immobilization of glucose oxidase and 2, 5-dihydroxybenzaldehyde for glucose fuel cells. Biosens. Bioelectron. **2010**, *25*, 2515–2521

191 Shah, S.; Solanki, K.; Gupta, M.N. Enhancement of lipase activity in non-aqueous media upon immobilization on multi-walled carbon nanotubes. *Chem. Cent. J.* **2007**, *1*, 1–30.

192 Arslan, A.; Kiralp, S.; Toppare, L.; Yagci, Y. Immobilization of tyrosinase in polysiloxane/polypyrrole copolymer matrices. *Int. J. Biol. Macromol.* **2005**, *35*, 163–167.

193 Tischer, W. Immobilized enzymes: Crystals or carriers? *Trends Biotechnol.* **1999**, *117*, 326–335.

194 Kim, M.A.; Lee, W.Y. Amperometric phenol biosensor based on sol–gel silicate/Nafion composite film. *Anal. Chim. Acta* **2003**, 479, 143–150.

195 Yu, J.H.; Liu, S.Q.; Ju, H.X. Mediator-free phenol sensor based on titania sol–gel encapsulation matrix for immobilization of tyrosinase by a vapor deposition method. *Biosens. Bioelectron.* **2003**, *19*, 509–514.

196 Fernández-Mar, M.I.; Mateos, R.; García-Parrilla, M.C.; Puertas, B.; Cantos-Villar, E. Bioactive compounds in wine: Resveratrol, hydroxytyrosol and melatonin: A review. *Food Chem*. **2012**, *130*, 797–813.

197 Lekse, J.; Xia, L.; Stark, J.; Morrow, J.D.; May, J.M. Plant catechols prevent lipid peroxidation in human plasma and erythrocytes. *Mol. Cell. Biochem.* **2001**, *226*, 89–95.

198 Solomon E.I., Baldwin M.J., Lowery M.D., *Chem. Rev.* **1992**, *92*, 521–542.

199 Mogharabi A., Faramarzi M.A., *Adv.Synth. Catal.* **2014**, *356*, 897–927.

200 Ca˜nas A.I., Camarero S., *Biotechnol. Adv.* **2014**, 28, 694–705.

201 Rico A., Rencoret J., Del Río J.C., Martínez A.T., Gutiérrez A., *Biotechnol. Biofuels* **2014**, *7*, 6.

202 Antuch M., Abradelo D.G., Cao New R., *J. Chem*. **2014**, *38*, 386–390.

203 Giroud F., Minteer S.D., *Electrochem. Commun.* **2013**, *34*, 157–160.

204 Santhanam N., Vivanco J.M., Decker S.R., Reardon K.F., *Trends Biotechnol.* **2011**, *29*, 480–489.

205 Pang H.L., Liu J., Hu D., Zhang X.H., Chen J.H., *Electrochim. Acta* **2010**, *55*, 6611–6616.

206 Nazaruk E., Karaskiewicz M., ˙Zelechowska K., Biernat J.F., Rogalski J., Bilewicz R., *Electrochem. Commun.* **2012**, *14*, 67–70.

207 Zhaoa H.Y., Zhoua H.M., Zhanga J.X., Zhenga W., Zheng Y.F., *Biosens. Bioelectron.* **2009**, *25*, 463–468.

208 Zheng W., Zhou H.M., Zheng Y.F., Wang N., *Appl. Phys. Lett.* **2008**, 457, 381–385.

209 Bilewicz R., Stolarczyk K., Sadowska K., Rogalski J., Biernat J.F., ECS Trans. **2009**, *19*, 27–36.

210 Babot E.D., Rico A., Rencoret J., Kalum L., Lund H., Romero J., del Rio J.C., Martinez I.T., A. Gutierrez, *Bioresour. Technol.* **2011**, *102*, 6717–6722;

211 Areskogh D., Henriksson G., *Process Biochem.* **2014**, *46*, 1071–1075.

212 Concalves A.R., Costa S.M., Esposito E. *Appl Environ Microbiol.* **1998**, *64*, 2026–2031.

213 Masamoto, Y.; Kubo, M. Inhibitory effect of Chinese crude drugs on tyrosinase. *Planta Med.* **1980**, *40*, 361–365.

214 Anderson R., Griffin K., Johnston P., Alsters P.L., *Adv. Synth. Catal.* **2003**, *345*, 517–523.

215 Eggert C., Temp U., Dean J.F.D., Eriksson K.-E.L., *FEBS Lett.* **1996**, *391*, 144–148.

216 Tromp S.A., Matijoˇsyt I., Sheldon R.A., Arend I.W.C.E., Mul G., Kreutzer M.T., Moulijn J.A., de Vries S., *ChemCatChem* **2010**, *2*, 827–833.

217 Park J.H., Xue H., Jung J.S., Ryu K., *Korean J. Chem. Eng.* **2012**, *29*, 1409–1412.

218 Sukhorukov G., Fery A., Mc H. ¸ hwald, *Prog. Polym. Sci.* **2005**, *30*, 885–897.

219 Recio M. C., Andujar J., Rios J. L., *Current Medicinal Chemistry*, **2012**, *19*, 2088.

220 Welch B.D., Van Demark A. P., Heroux A., Hill C. P., Kay M. S., *Proceedings of the National Academy of Science*, **2007**, *104*, 16828-16833.

221 Walensky L.D., Kung A. L., Escher I., *Science*, **2004**, *305*, 1466-1470.

222 Kanazawa M., Ohba H., Harada N., Kakiuchi T., Muramatsu S. and Tsukada H., *Journal of Nuclear Medicine*, **2016**, *57*, 303-308

223 Abou-Sleiman P. M., Muqit M. M., Wood N. W., *Nature Reviews Neuroscience* **2006**, *7*, 207-219.

224 Bai J. P., Amidon G. L., *Pharmaceutical Research* **1992**, *9*, 969-978

225 Fei Y.J., Kanai Y., Nussberger S., Ganapathy V., Leibach F. H., Romero M. F., Singh S. K., Boron W. F., Hediger M. A., *Nature*, **1994**, *368*, 563-6.

226 Miyamoto K., Shiraga T., Morita K., Yamamoto H., Haga H., Taketani Y., Tamai I., Sai Y., Tsuji A., Takeda E., *Biochimica and Biophysica Acta* **1996**, *1305*, 34-38.

227 Wang H.P., Lee J.-S., Tsai M.-C., Lu H.-H., Hsu W., *Bioorganic & Medicinal Chemistry Letters* **1995**, *5*, 2195-2198.

228 O'Neill J., Veitch F., Wagner-Jauregg T., *The Journal of Organic Chemistry* **1956**, *21*, 363-364

229 Bizzarri B.M., Tortolini S., Rotelli L., Botta G., Saladino R., *Current Medicinal Chemistry*, **2015**, *22*, 4138-4165.

230 Ueda J., Ozawa T., Miyazaki M., Fujiwara Y., *Journal of Inorganic Biochemistry*, **1994**, *55*, 123-130

231 Lazzaro C.F., Crucianelli M., De Angelis F., Neri V., Saladino R., *Tetrahedron Letters*, **2004**, *45*, 9237-9240.

232 Miller S.M., Simon R.J., Zucherman R.N., Kerr J.M., Moos W.H., *Drug Development Research*, **1995**, *35*, 20-32

233 Bizzarri B.M., Pieri C., Botta G., Arabuli L., Mosesso P., Cinelli S., Schinoppi A., Saladino R. *RSC Advances*, **2015**, *5*, 60354-60364

234 Jimenez M., Garcia-Carmona F., Garcia Canovas F., Iborra J. L., Lozano J. A., Martinez F., *Archives of Biochemistry and Biophysics*, **1984**, *235*, 438-448.

235 Dias V., Junn E., and Mouradian M., Journal of Parkinson's disease. **2013**, *3*, 461-491.

236 Beal M.F., *Annual Neurology*, **2005**, *58*, 495-505.

237 Brena B., González-Pombo P., Batista-Viera F., *Methods in molecular biology*. **2013**, *1051*, 15-31.

238 Botta G., Bizzarri B.M., Garozzo A., Timpanaro R., Bisignano B., Amatore D., Palamara A.T., Nencioni L., Saladino R., *Bioorganic & Medicinal Chemistry* **2015**, *23*, 5345-5351.

239 Mercuri N.B., Bonci A., Calabresi P., Stefani A., Bernardi G., *European Journal of Neuroscience*, **1995**, *7*, 462-9.

240 Berretta N., Bernardi G., Mercuri N.B. *The Journal of Physiology*, **2010**, *588*, 1719-35

241 Guatteo E., Yee A., McKearney J., Cucchiaroni M.L., Armogida M., Berretta N., Mercuri N.B., *J. Lipski, Experimental Neurology*, **2013**, *247*, 582-94

242 Guatteo E., Fusco F.R., Giacomini P., Bernardi G., Mercuri N.B.. *The Journal of Neuroscience*, **2000**, *15*, 6013-20.

243. Barbosa O., Torres R., Ortiz C., Shuster B., Fishman A., *Journal of Molecular Microbiology and Biotechnology* **2009**, *6*, 188-200

244 Satish C., Mohapatra J.T., *Biotechnology Techniques* **1994**, *8*, 13–16.

245 Mercuri N.B., Calabresi P., Bernardi G., *Life Science* **1992**, *51*, 711-8

246 Guatteo E., Federici M., Siniscalchi A., Knöpfel T., Mercuri N.B, Bernardi G., *Journal of Neurophysiology* **1998**, *79*, 1239-45

247 Oliveira A.A., Teixeira I.F., Leandro P., Ribeiro E.L., Lorencon E., Ardisson J.D., Fernandez-Outon L., Waldemar A.A., Macedo F., Moura C.C., *Appl. Catal. A* **2013**, *456*, 126-134.

248 De Souza W.F., Guimaraes I., Guerreiro M.C., Oliveira L.C.A., *Appl. Catal. A* **2009**, *360*, 205-209.

249 Eßer J., Wasserscheid P., Jess A., *Green Chem.* **2004**, *6*, 316–322.

250 Vít Z., Gulková D., Kaluža L., Kupčík J., *Appl. Catal. B* **2015**, *179*, 44-53.

251 Farhat Ali M., Al-Malki A., El-Ali B., Martinie G., Siddiqui M.N., *Fuel* **2006**, *85*, 1354–1363.

252 Wang Y., Li G., Wang X., Jin C., *Energy Fuels* **2007**, 21, 1415–1419.

253 Zhao H., Baker G.A., *Front. Chem. Sci. Eng.* **2015**, *9*, 262-279.

254 Campos-Martin J.M., Capel-Sanchez M. C., Perez-Presas P., Fierro J.L.G., *J. Chem. Technol. Biotechnol.* **2010**, *85*, 879-890.

255 Shaabani A., Behnam M., Rezayan A.H, *Catal. Commun.* **2009**, *10*, 1074-1078.

256 Gokel G.W., Gerdes H.M., Dishong D.M., *J. Org. Chem.* **1980**, *45*, 3634-3639.

257 Kubota A., Takeuchi H., *Org. Process Rev. Dev.* **2004**, *8*, 1076-1078.

258 Cedeño Caero L., Jorge F., Navarro A., Gutiérrez-Alejandre A., *Catal. Today* **2006**, *116*, 562–568.

259 Chan N.Y., Lin T.-Y., Yen T.F., Energy Fuels **2008**, *22*, 3326–3328.

260 Nonaka O.S., Takashima T., Qian W.H., Gakkaisi S., *J. Jpn. Pet. Inst.* **1999**, *42*, 315-320.

261 Campos-Martin J.M., Capel-Sanchez M.C., Fierro J.L.G., *Green Chem.* **2004**, *6*, 557–562.

262 Di Giuseppe A., Crucianelli M., De Angelis F., Crestini C., Saladino R., *Appl. Catal. B* **2009**, *89*, 239-245.

263 W.A. Herrmann, R.W. Fischer, W. Scherer, M.U. Rauch, *Angew. Chem. Int. Ed.* **1993**, *32*, 1157–1160.

264 Crucianelli M., Saladino R., De Angelis F., *ChemSusChem* **2010**, *3*, 524-540.

265 Saladino R., Botta G., Crucianelli M., in: T.A. Saleh (Ed.), Applying Nanotechnology to the Desulfurization Process in Petroleum Engineering, IGI Global (USA), **2016**, 180-215.

266 Zhai Y., Zhu Z., Dong S., *ChemCatChem* **2015**, *7*, 2806-2815

267 Chen M.L., Zhang F.J., Oh W.C., *New Carbon Mater.* **2009**, *24*,159–166.

268 Kozhevnikov I.V., in: Catalysts for Fine Chemical Synthesis, Vol. *2*, Catalysis by Polyoxometalates, John Wiley & Sons, Chichester, **2002**.

269 Meman N.M., Pourkhalil M., Rashidi A., Zarenezhad B., *J. Ind. Eng. Chem.* **2014**, *20*, 4054-4058.

270 Kwok R.W.M., XPS Peak Fitting Program for WIN95/98 XPSPEAK Version 4.1, Department of Chemistry, The Chinese University of Hong Kong.

271 Zhan G., Zeng H.C., *Chem. Mater.* **2015**, *27*, 726−734.

272 Hanefeld U., Gardossi L., Magner E., *Chem. Soc. Rev.* **2009**, *38*, 453−468.

273 Maggini L., Raquez J.-M., Marega R., Ahrens J.J., F. Pineux, Meyer F., Dubois P., Bonifazi D., *ChemSusChem* **2013**, *6*, 367-377.

274 Saladino R., Pelliccia A.R., Neri V., Caminiti R., Sadun C. *J. Org. Chem.* **2002**, 67, 1323-1332.

275 O'Connell M.J., Boul P., Ericson L.M., Huffman C., Wang Y., Haroz E., Kuper C., Tour J., Ausman K.D., Smalley R.E., *Chem. Phys. Lett.* **2001**, 342, 265-271.

276 Hua J., Wang Z., Zhao J., Xu L., Zhang J.I., Li R., Sun X., *J. Macromol. Sci. B* **2011**, *50*, 679-687.

277 Jing H., Zhongguang W., Jian Z., Jin Z., Ruying L., Hengyong N., Xueliang S., *Colloid Polym. Sci.* **2011**, *289*, 783-789.

278 Rao C.N.R., Govindaraj A., *Nanosci. Nanotechnol.* **2011**, *18*.

279 Li L., Ou X., Sims S., Li W., Wu L., *RCS Adv.* **2014**, *4*, 56998-57008.

280 Yan Y., Miao J., Yang Z., Xiao F.-X., Yang H. B., Liu B., Yang Y., *Chem. Soc. Rev.* **2015**, *44*, 3295-3346.

281 Choudary B.M., Roy M., Roy S., Kantam M.L., Sreedhar B., Vijay Kumar K., *Adv. Synth. Catal. 348*, **2006**, 1734-1742.

282 Cedeño-Caero L., Gomez-Bernal H., Fraustro-Cuevas A., Guerra-Gomez H.D., Cuevas-Garcia R., *Catal. Today*, **2008**, *133–135*, 244–254.

283 Patrut C., Bildea C.S., Kiss A.A., *Chem. Eng. Process.* **2014**, *81*, 1-12.

284 Yajie T., Yue Y., Yanhui Z., Lijun Y., Shuxiang L., *Energy Fuels* **2015**, *29*, 618-625.

285 Sharifzadeh Baei M., Rezvani M.A., *Asian J. Chem.* **2011**, *23*, 5381-5389.

286 Napanang T., Sooknoi T., *Catal. Commun.* **2009**, *11*, 1-6.

287 Lee C.M., Pearce E.M., Kwei T.K., *Polymer* **1996**, *37*, 4283–4288.

288 Fang Y., Hu H., *Catal. Commun.* **2007**, 8, 817-820.

289 Sampanthar J.T., Dou J., Joo G.G., Widjaja E., Eunice L.Q.H., *Nanotechnology* **2007**, *18*, 025601.

290 Lorenc E.¸, D.C.B. Alves, Krambrock K., Ávila E.S., Resende R.R., Ferlauto A.S., Lago R.M., *Fuel* **2014**, *132*, 53–61

291 Moulijn J.A., van Diepen A.E., Kapteijn F., *Appl. Catal. A* **2001**, *212*, 3–16.